Tunable broadband and high-field THz time-domain spectroscopy system

Wei Cui

Thesis submitted to the University of Ottawa
in partial Fulfillment of the requirements for the
Doctor of Philosophy in Physics

Department of Physics
Faculty of Science
University of Ottawa

Abstract

This thesis focuses on improving the performance of the THz time-domain spectroscopy system using second-order nonlinear crystals for THz generation and detection in terms of bandwidth, sensitivity, and THz field strength. The theories for the THz generation based on optical rectification and detection technique, electro-optical sampling, based on Pockels effect are introduced in Chapter 2. In Chapter 3, some experiments are presented to characterize the performances of the THz system based on a 180 fs Yb:KGW femtosecond laser amplifier operating at 1035 nm. The Yb-based femtosecond laser is becoming increasingly popular due to its robustness, high repetition rate, and high average power. However, the NIR bandwidth of these femtosecond lasers is limited by the gain bandwidth of the gain medium, and achieving pulse durations shorter than 180 fs is challenging. Consequently, the full bandwidth of THz time-domain spectroscopy systems is constrained by such laser systems. In order to broaden the THz bandwidth of such THz time-domain spectroscopy systems, our work in Chapter 4 combines the Yb:KGW femtosecond laser amplifier with an argon-filled hollow-core photonic crystal fiber pulse shaper to spectrally broaden the near-infrared pulses from 3.5 to 8.7 THz, increasing the measured THz bandwidth correspondingly from 2.3 THz to 4.5 THz. This is one of the first works to have broadband THz system based on Yb-based femtosecond lasers in the year of 2018. In Chapter 5, the tilted-pulse-front phase matching in the THz generation and detection scheme is demonstrated using the same surface-etched phase gratings on the front surfaces of the 2 mm-thick GaP generation and detection crystals. This scheme overcomes the THz generation and detection bandwidth limit of thick crystals imposed by the traditional collinear phase matching, while allowing the long nonlinear interaction length. This results in a THz spectral range from 0.1 to 6.5 THz with a peak at 3 THz and a peak dynamic range of 90 dB. In the range between 1.1 and 4.3 THz, the system dynamic range exceeds 80 dB. Based on this contact grating-based THz generation, the next step involves generating high-field THz above 2 THz. For high-field THz generation, the most renowned technique is the tilted-pulse-front technique, which generates high-field THz below 2 THz in a $LiNbO_3$ crystal. Most nonlinear optics experiments in the THz regime rely on such THz sources. To

generate high-field THz above 2 THz, one promising candidate is organic THz crystals. However, most organic crystals require a pump laser with a wavelength exceeding 1200 nm, necessitating a more complex laser system. Additionally, the low damage threshold of these crystals are susceptible to compromise the stability of the measurements. Other techniques, such as air plasma and metallic spintronics, can generate ultra-broadband high-field THz from 0.1 to 30 THz, but the pulse energy within certain frequency windows is relatively low, rendering these THz sources less effective for nonlinearly driving specific optical transitions. On the other hand, semiconductor crystals as THz generation crystals, have a high damage threshold and can achieve good phase matching at wavelength around 800 or 1000 nm. In Chapter 6, high-field THz generation with a peak field of 303 kV/cm and a spectral peak at 2.6 THz is achieved with a more homogenous grating on the surface of a 1 mm-thick GaP generation crystal in a configuration collimating the near-infrared generation beam with a pulse energy of 0.57 mJ onto the generation crystal. The experiments also show that the system operates significantly below the GaP damage threshold and THz generation saturation regime, indicating that the peak THz field strength can approach 1 MV/cm, with a 5 mJ near-infrared generation pulse. This is the first high-field THz source based on semiconductor crystals capable of generating high-field THz above 2 THz. With such a THz source, we can conduct nonlinear optics experiments above 2 THz, including the study of phonon-assisted nonlinearities, coherent control of Bose-Einstein condensation of excitons and polaritons in semiconductor cavities, and saturable absorption in molecular gases.

Statement of originality and collaborative contributions

To the best of his knowledge, the author affirms that the research presented in this thesis is original. The contributions from the author to each of the publications in this thesis are detailed below.

Chapter 4 contains the paper entitled “Broadband and tunable time-resolved THz system using argon-filled hollow-core photonic crystal fiber” which was published in 2018 in APL Photonics. Wei Cui and Aidan Schiff-Kearn built the THz system. Emily Zhang and Nicolas Couture built the hollow-core photonic crystal fiber system. Wei Cui collected the data, analyzed the data and made the figures for the manuscript. Francesco Tani and David Novoa performed the simulation of the propagation of the NIR pulse in the hollow-core photonic crystal fiber. Philip St.J. Russell provided the hollow-core photonic crystal fiber. Wei Cui and Jean-Michel Ménard drafted the original manuscript. Wei Cui handled the reviewing process under the supervision of Jean-Michel Ménard. All authors reviewed and contributed to the published manuscript.

Chapter 5 contains the paper entitled “Broadband and high-sensitivity time-resolved THz systems using grating assisted tilted-pulse-front phase matching” which was published in 2022 in Advanced Optical Materials. Wei Cui built the experimental system, collected, and analyzed the data, performed the simulations, made the figures and drafted the original manuscript. Kashif Masud Awan fabricated the grating on the nonlinear crystals for THz generation and detection. Wei Cui handled the reviewing process under the supervision of Jean-Michel Ménard. All authors reviewed and contributed to the published manuscript.

Chapter 6 contains the paper entitled “High-field THz source centered at 2.6 THz” which was published in 2023 in Optics Express. Wei Cui built the experimental system. Mohammad Bashirpour fabricated the grating on the nonlinear crystals. Wei Cui, Eeswar Kumar Yalavarthi and Aswin Radhan collected the data. Wei Cui analysed the data. Wei Cui and Eeswar made the figures. Wei Cui drafted the original manuscript. Wei Cui handled the reviewing process under the supervision of Jean-Michel Ménard. All authors reviewed and contributed to the published manuscript.

Acknowledgements

I would like to extend my heartfelt gratitude to numerous individuals who have been instrumental in my PhD journey. First and foremost, my supervisor, Jean-Michel Ménard. Thank you for introducing me to the THz community and for being an exceptional supervisor over the past 7 years! I deeply appreciate your high standards for quality and attention to details! You also supported me through two of the most challenging periods in my life during my PhD journey. I am hopeful that the THz systems we developed over these years will lead to more intriguing projects in the future!

I also want to thank my co-supervisor, Ravi Bhardwaj. While it was a pity that I have not had the opportunity to work more extensively with you during my PhD, your support during the initial 4 years was invaluable. I thoroughly enjoyed the spectroscopy course you taught. As I conclude my PhD, I believe the THz system I built will be instrumental in studying the fluorescence properties of the PMMA. I hope future students will continue this project.

Angela Gamouras, thanks for your support during the last 3 years of my PhD study. You helped so much revise my manuscripts, conference proceedings and so on! You also gave me a lot of useful advice on research and career direction. Wish you all the best for your professional and personal life!

I have had the privilege of collaborating with many colleagues. Aidan Schiff-Kearn, our initial 2 years in Ottawa, spent building the THz system and experimenting with various materials, were memorable. Our mutual support and culinary adventures in Ottawa, Montreal and Regensburg will always be cherished. Wish you success in completing your PhD and a fulfilling future. Lauren Gingras, I gained much from our collaboration and your postdoc tenure in our group. Your assistance extended beyond the lab to conference participation. Alexi Halpin, as the first postdoc I have worked with, especially after recovering from my sickness, I am grateful for your guidance for me back to the research life and support in my research endeavors. Nicolas Couture, we worked a lot together and I really enjoy our seamless science communication. Your dedication resulted in the success of our joint project. I wish you continued success in your future endeavors. Ahmed Jaber, we spent a lot of time measuring your samples together and I admire

your inquisitive nature. Also, thanks for helping me improve my English writing. Aswin Vishnu Radhan, we worked together in the last 2 years of my PhD, and your rigorous and careful attitude in experiments impressed me. Thank you for your contributions to our high-field paper. Eeswar Kumar Yalavarthi, you are the youngest member in our group. Your zeal for learning diverse experimental techniques is inspiring. I also appreciate your contributions to our high-field paper. I extend my best wishes to all group members who stood for me during my PhD and through the most challenging times of my life.

I also need to thank my friends Le Qiao, Zi Chao Zhou and Lijuan Gu. We had a lot of fun in Ottawa and on the trips. A special thanks to Fanqi Kong for invaluable research suggestions and good career advice. We also enjoyed playing basketball together. Chang Zhang, we collaborated at the end of my PhD but we became good friends so quickly. Thanks for your support during my hard time this year!

My dear wife Yuanming Zhao, we met each other in Waterloo, and you have been with me throughout the last 7 years in Ottawa. We went through all the challenges and enjoyed all the success together. In 2018, your unwavering love and support during my sickness have been my anchor. This year, in the hardest time, you are with me all the time and I hope our future is filled with love and serenity.

To my mother Renqing Xu, you brought me to the world and your unwavering support throughout my life has been invaluable. I wish you health and happiness in the years to come.

Lastly, to my dear father, Zhifeng Cui, I deeply regret that you couldn't witness my graduation. You were the one who guided me into the physics world. The memory of the purple pulsed laser in your lab from my childhood remains vivid. Your unwavering support, both emotionally and intellectually, especially over the last 4 years, has been my strength. I promise to forge ahead with resilience, hoping you find peace in heaven.

Table of Contents

List of Figures

Chapter 1

Introduction of THz time-domain spectroscopy

1.1 Terahertz

When we say 'Terahertz (THz)', we're talking about frequencies that are 10^{12} times a second. The Terahertz band is a part of the electromagnetic spectrum, and it is usually defined as ranging from 0.1 to 30 THz. Due to its distinct properties, such as its low photon energy (non-ionizing radiation), high penetration depth in many materials traditionally considered opaque and strong interaction with molecular vibrations, THz technology has found extensive applications in diverse areas. Typical applications encompass THz imaging [1,2], security screening [3,4], material characterization [5,6], quality control [7,8] and THz communication [9,10]. Historically, the THz band was a technical void as THz frequencies exceed the upper frequency limit of the electronic systems and fall below the lower frequency limit of the laser systems. The absence of effective THz generation and detection techniques rendered the THz range elusive for researchers. However, over the last three decades, significant advancements in the THz technology have progressively bridged this gap.

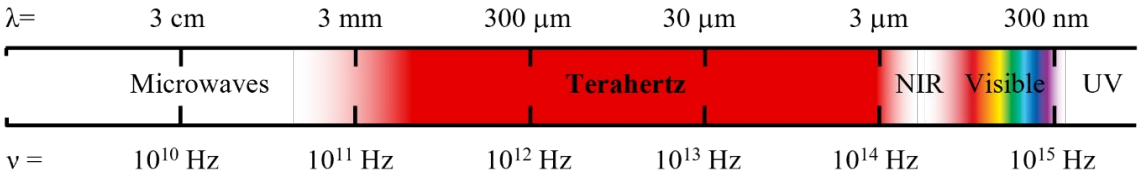

Fig. 1.1 The electromagnetic spectrum in the units of wavelength and the frequency. The THz band is between the near-infrared (NIR) and the microwaves.

Currently, available THz sources include quantum cascade lasers (QCLs) [11,12], free-electron lasers (FELs) [13], Gyrotrons [14] and those based on the femtosecond laser systems. The sources derived from femtosecond laser systems feature photo-conductive antennas [15,16], second order

nonlinear crystals [17], air plasma [18], and metallic spintronics [19,20]. Figure 1.2 illustrates the progression of the THz sources up to 2020 [21,22]. Note that the specifications of metallic spintronics are not included here; the bandwidth of metallic spintronics can range from 0.1 to 30 THz [19], and the highest THz power can reach 40 μW [20] at room temperature. Additionally, my PhD work on a high-field THz source in Chapter 6 is included in Fig. 1.2. The figure of merit in this figure is the output power, while my goal was to achieve a high THz peak field using a commercial ultrafast laser system. Furthermore, traditional commercial optical parametric amplifiers (OPAs), such as the TOPAS PRIME OPA, can generate wavelengths ranging from 0.189 to 20 μm (15 to 1587 THz). When operating around 20 THz, this OPA can produce 100 fs pulses with an average power of 0.3 mW, and the generation process becomes more efficient at higher THz frequencies. The Alpha OPA from Stuttgart Instruments can generate 350 fs pulses at 30 THz with an average power of 25 mW.

Among these THz sources, THz QCLs can generate high-power continuous-wave (CW) THz radiation with good beam quality. The system is compact but typically requires cryogenic cooling. Its spectral bandwidth tunability is limited by the design of the quantum well structures. The FELs can generate extremely high power and are capable of producing both CW and pulsed outputs. The THz frequency of FELs can be broadly tuned. However, they are large-scale equipment that requires significant operational and maintenance support. Gyrotrons primarily produce high-power CW THz beams below 1 THz. This equipment is bulky, and its frequency tunability is limited compared to other THz sources. Photoconductive antennas can generate pulsed THz radiation with a relatively broad bandwidth. The output power is relatively low compared to the aforementioned sources, and their lifetime could be limited due to high-intensity illumination. Second-order nonlinear crystals can generate both CW and pulsed THz radiation with significant frequency tunability, depending on linear properties of the crystal. However, the THz generation efficiency is relatively low, and a high-power laser is required for efficient THz generation. Among second-

order nonlinear crystals, semiconductor crystals have a higher damage threshold than organic crystals but a lower nonlinear coefficient for THz generation. Air plasma and metallic spintronics techniques are capable of generating ultra-broadband THz pulses. The air plasma technique does not require a nonlinear medium, thus avoiding material damage, but its conversion efficiency is still relatively low and necessitates a high-power laser for efficient THz generation. Metallic spintronics is compact and can be integrated with electronic devices, with its frequency not limited by phase-matching conditions. However, metallic spintronics is still in the early stages of research, and its output power and efficiency are relatively low.

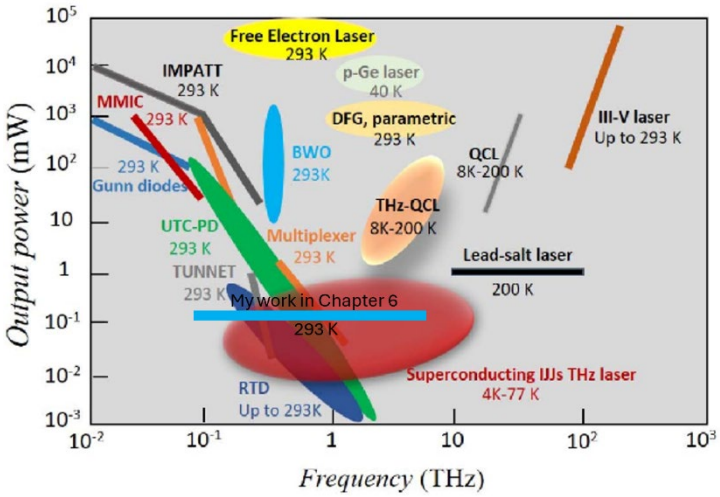

Fig. 1.2 The development of THz sources till 2020 [21,22] with my work in Chapter 6 [23]. MMIC: microwave monolithic integrated circuits; IMPATT: impact ionization avalanche transit-time diodes; BWO diodes backward wave oscillators; RTDs: resonant tunneling diodes; UTC-PD: uni-travelling carrier photodiodes; QCL: quantum cascade laser.

Numerous THz detectors are currently in use, each leveraging distinct mechanisms and offering unique advantages. Thermal effect based detectors include bolometers [24–26], which measure the resistance change of an absorptive element heated by a THz beam; Golay cells [27,28], which gauge pressure alterations in gas due to the heat from a THz beam; and pyroelectric detectors [29,30], which assess the potential difference between the two opposite faces of a pyroelectric crystal due to a temperature change induced by the absorption of a THz beam. These

thermal detectors are typically not fast (ms response time) and are not phase sensitive. Detectors utilizing THz-induced or -driven photocurrent comprise Schottky diodes [31,32] and photoconductive antennas [33–35]. Schottky diodes detect THz radiation by measuring the DC current rectified from the AC current induced by the oscillating THz field, while photoconductive antennas measure the THz-driven current between two electrodes in the antennas. The response time of such detectors is in the picosecond or even sub-picosecond range. Schottky diodes are not phase-sensitive, whereas photoconductive antennas are phase-sensitive. Additionally, nonlinear effect-based THz techniques such as electro-optical sampling (EOS) [36–38], which leverages the second-order nonlinear effect in crystals, and terahertz wave air-based-coherent-detection (ABCD) [39,40], harnessing the third-order nonlinearity of laser-induced air plasma. Notably, the photoconductive antenna, EOS and ABCD not only measure the intensity of the THz beam but also the phase of the electric field, making these techniques invaluable in THz time-domain spectroscopy (THz-TDS) for material characterization.

An optimal THz system is anticipated to possess high peak power/field, facilitating measurements of highly absorptive materials and enabling nonlinear experiments. Additionally, a system operating at high repetition rate above 1 kHz (repetition rate of traditional Ti:Sapphire fs lasers) would increase the data acquisition speed, while a tighter THz focus can improve the spatial resolution and provide higher peak field strengths. Furthermore, such a system should exhibit high sensitivity to discern subtle alterations in materials, offer a broader spectral bandwidth to acquire comprehensive material information, feature rapid measurement capabilities, and maintain a compact device size.

My PhD thesis focuses on improving the traditional techniques used for THz generation and detection based on the nonlinear effects of ultrashort optical pulses. The THz generation in nonlinear crystals occurs via optical rectification (OR), a second-order nonlinear effect. This process involves the difference-frequency mixing of high-frequency and low-frequency

components within an ultrafast NIR pulse. The THz detection is performed with the EOS technique inside a second-order nonlinear semiconductor crystal. In the detection crystal, the slowly oscillating THz electric field modulates the polarization of the NIR femtosecond gating pulse through the Pockels effect. Notably, the degree of the polarization shift is linearly related to the transient THz electric field amplitude. A more in-depth exploration of the THz generation through difference frequency mixing and detection via electro-optical sampling is provided in the subsequent section.

1.2 THz time-domain spectroscopy

THz time-domain spectroscopy (THz-TDS) is a technique to investigate the properties of the materials in the THz range. The key to the technique is the generation of the THz pulses from NIR femtosecond generation pulses and the detection of the THz pulses which time-resolves the electric field oscillation of the THz pulses, providing both the amplitude and phase information at one time.

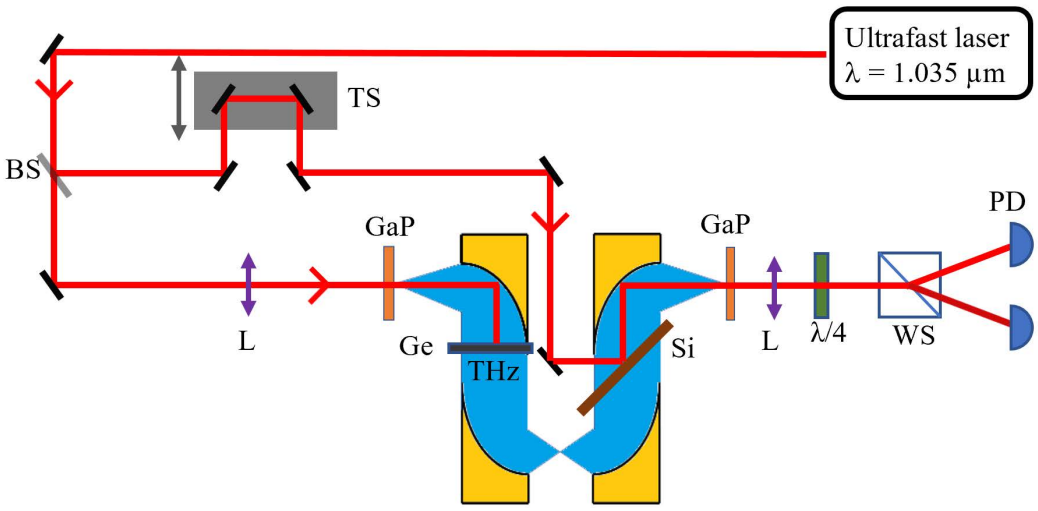

Fig. 1.3 The schematic of the standard THz time-domain spectroscopy system built in our lab. The THz generation and detection are both performed using nonlinear crystals. BS: beam splitter; TS: translational stage, GaP: 110-oriented 220 μm-thick gallium phosphide crystal; Ge: germanium wafer; Si: silicon wafer; L: lens, λ/4: quarter-wave plate; WP: Wollaston prism; PD: photodetector.

Figure 1.3 presents a standard THz time-domain spectroscopy system [41] I built in our lab. The NIR pulse coming out of the a Yb:KGW femtosecond laser amplifier splits into 2 arms. The first arm is focused on a 110-oriented nonlinear generation crystal to generate THz through optical rectification. A 2″ diameter parabolic mirror with a 5 cm focal length is put after the generation crystal to maximally collect the emitted THz beams. A Ge wafer is put after this first parabolic mirror to block the residual NIR beam while transmitting the generated THz beam. The residual NIR beam is collimated onto the Ge wafer, thereby exciting free electrons with a density of 2.75×10^{14} cm^{-3}. As a result, the free electron absorption coefficient of THz radiation is calculated to be 1.13×10^{-26} cm^{-1} at 2 THz, which can be considered negligible in this Ge wafer. A second parabolic mirror focuses the collimated THz beam to create a THz focus for the sample to be investigated in the THz-TDS system. A third parabolic mirror is then placed to recollimate the THz beam. In the following collimated THz section, a silicon wafer is put 45° into the THz beam which transmits the THz beam and reflects the NIR gating beam from the other arm. The second arm of the NIR beam goes through a linear mechanical translational stage which varies the temporal difference between the generated THz beam and the NIR beam in this gating arm with small stepping resolution. This detection beam is overlapped on the silicon wafer spatially and temporally. The detection beam is also collimated onto the Si wafer, exciting a free electron density of 1.28×10^{13} cm^{-3}. This free electron density in Si contributes to an absorption coefficient of 2.24×10^{-24} cm^{-1} at 2 THz, which can also be considered negligible. Then, the gating NIR beam and the THz beam are both focused onto the same spot on the detection crystal. The NIR beam's polarization is rotated by the THz beam through Pockels effect. The rotation angle of the NIR beam is measured through a quarter wave plate, a Wollaston prism, and a pair of balanced photodetectors.

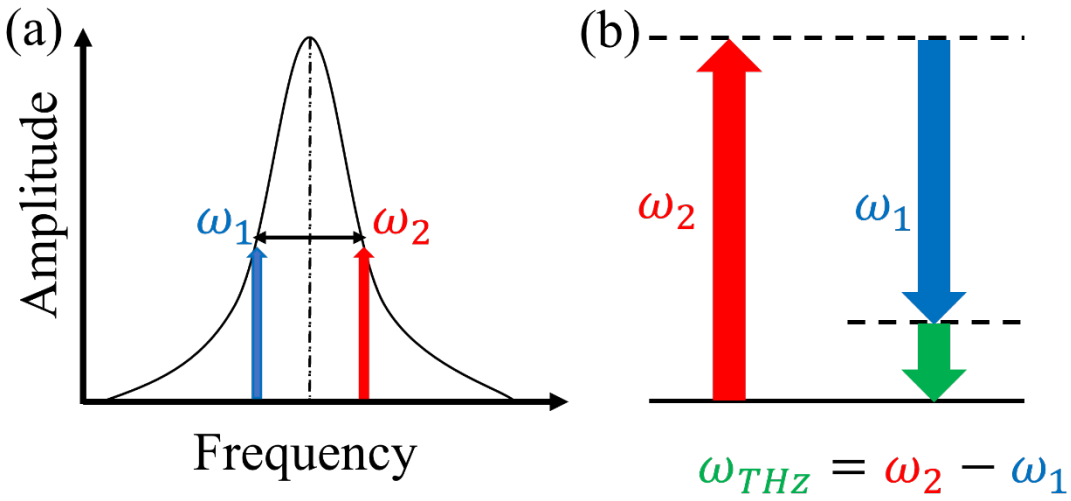

Fig. 1.4 The mechanism of THz generation via OR. (a) An optical spectrum of a NIR pulse for THz generation. (b) Photon description of the interaction between 2 NIR photons to produce a THz photon through difference frequency generation (DFG).

Fig. 1.4 illustrates the principle of the THz generation inside a second-order nonlinear crystal via optical rectification of an NIR pulse. The spectrum of an NIR femtosecond pulse encompasses numerous frequency components. During THz generation, a high-frequency photon interacts with a low-frequency photon, producing a new photon with a frequency equal to the frequency difference between the two original NIR photons; this emergent photon has a frequency in the THz range. Consequently, the spectral bandwidth of the generated THz pulse is inherently tied to the spectral range of the NIR generation pulse: a broader NIR spectrum results in a wider THz bandwidth (assuming that the NIR generation pulse is Fourier transform-limited), despite other factors affecting the THz generation bandwidth, such as the linear properties of the THz generation crystal related to phase-matching conditions. Chapter 4 of this thesis delves into an example of expanding the THz spectrum of a THz-TDS system by broadening the NIR generation pulse's spectral bandwidth using a hollow-core photonic crystal fiber pulse shaper.

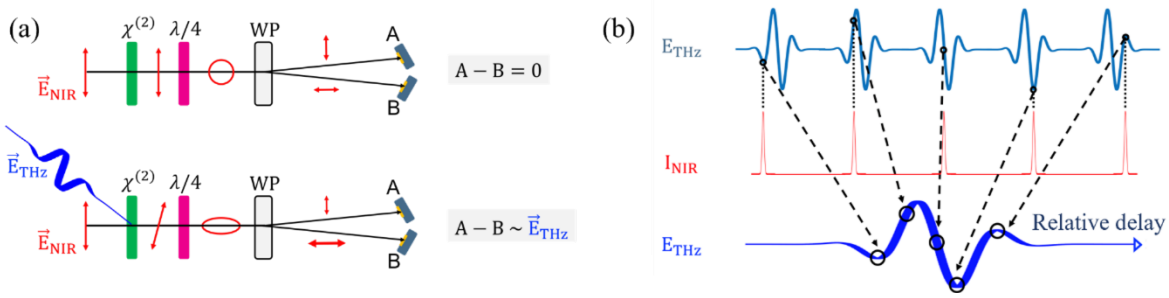

Fig. 1.5 Principle schematic of the electro-optical sampling technique (adapted from [42]). (a) Polarization changes of the NIR gating beam with and without the illumination of the THz together with the corresponding differential signal between the A and B balanced photodetectors. $\chi^{(2)}$: second order nonlinear crystals; $\lambda/4$: quarter-wave plate; WP: Wollaston prism. (b) Process of the time-resolved detection of the THz electric field.

Figure 1.5 elucidates the principle behind the electro-optical sampling (EOS) technique for THz detection. In Figure 1.5(a), without THz illumination on the gating crystal, the horizontally polarized NIR gating beam polarization remains unchanged as it traverses the second-order nonlinear crystal. Subsequently, after passing through the quarter-wave plate, this beam adopts a circular polarization. Upon encountering the Wollaston prism, NIR beams with orthogonal polarization, in equal proportions, strike the A and B photodiodes, resulting in a voltage difference 0 V between A and B photodiodes. However, when the THz pulse spatially and temporally coincides with the NIR gating pulse on the gating crystal, the THz beam alters the NIR beam's polarization within the gating crystal via the Pockels effect (for a more detailed theory, refer to Chapter 2). Figure 1.5(b) depicts the time-resolved progression of the electric field of the THz pulse. THz pulses oscillate over periods on the order of picoseconds (ps), whereas the NIR gating pulses have a pulse duration of below 200 fs. Consequently, each segment of the electric field of the THz pulse can be viewed as a transient DC electric field influencing a NIR fs pulse. By adjusting the position of the translational stage, distinct temporal segments of the THz pulse can be successively overlapped with the NIR femtosecond pulse. The varying electric field strengths across the THz pulse's duration will induce proportional rotations in the NIR gating pulse's polarization. This mechanism enables the EOS technique to time-resolve oscillation in the THz electric field.

Chapter 2

Theory of nonlinear optical process for THz generation and detection

In this chapter, the theory of the second-order nonlinear processes will be presented in detail. We start from Maxwell's equations to derive the coupled-wave equation describing the second-order nonlinear polarization which is the source of second-order nonlinear effects. The derived equations are then used to describe the second nonlinear effects in the THz generation and detection process.

2.1 Optical nonlinearity

To describe the optical nonlinearity, we first need to understand how the polarization, $\tilde{P}(t)$ (dipole moment per unit volume), of a material depends on the electric field strength, $\tilde{E}(t)$ of an applied field. The accent ~ over a quantity here means this quantity varies rapidly with time. The polarization inside a one-dimensional (1D) lossless and dispersionless material can be written as:

$$\begin{aligned}\tilde{P}(t) &= \epsilon_0\left[\chi^{(1)}\tilde{E}(t) + \chi^{(2)}\tilde{E}(t)^2 + \chi^{(3)}\tilde{E}(t)^3 + \cdots\right] \\ &= \tilde{P}^{(1)}(t) + \tilde{P}^{(2)}(t) + \tilde{P}^{(3)}(t) + \cdots,\end{aligned} \tag{2.1.1}$$

where ϵ_0 is the free space permittivity, $\chi^{(1)}$ is the linear susceptibility, $\chi^{(2)}$ is the second-order nonlinear susceptibility, and $\chi^{(3)}$ is the third-order nonlinear susceptibility. Then $\tilde{P}^{(1)}(t)$ is the linear polarization, $\tilde{P}^{(2)}(t)$ is the second order nonlinear polarization and $\tilde{P}^{(3)}(t)$ is the third-order nonlinear polarization and so on. Here we also assume that the material response is instantaneous to the applied electric field, implying the time dependance of the linear and nonlinear susceptibilities is neglected here. In the THz generation and detection process based on the second-order nonlinear crystals, what we are interested in is the second-order nonlinear polarization:

$$\tilde{P}^{(2)}(t) = \epsilon_0\chi^{(2)}\tilde{E}(t)^2. \tag{2.1.2}$$

As we can see, in a three-dimensional space (3D), the electric field and the polarizations will form vector quantities and the nonlinear susceptibilities will be tensors.

In a material with dispersion and loss, the electric field can be described as a sum of discrete frequency components:

$$\tilde{\vec{E}}(\vec{r}\,,t) = \sum_n \tilde{\vec{E}}_n(\vec{r},t), \tag{2.1.3}$$

where:

$$\tilde{\vec{E}}_n(\vec{r},t) = \vec{E}_n(\vec{r})e^{-i\omega_n t} + c.c. = \vec{A}_n e^{i(\vec{k}_n r - \omega_n t)} + c.c.. \tag{2.1.4}$$

Then the full electric field can be written as:

$$\tilde{\vec{E}}(\vec{r}\,,t) = \sum_n \vec{A}_n e^{i(\vec{k}_n r - \omega_n t)} + c.c.. \tag{2.1.5}$$

Similarly, the nonlinear polarization can also be written as:

$$\tilde{\vec{P}}(\vec{r},t) = \sum_n \vec{P}\,(\omega_n)e^{-i\omega_n t} + c.c.. \tag{2.1.6}$$

The second-order nonlinear polarization components we are interested in are:

$$P_i(\,\omega_n + \omega_m) = \epsilon_0 \sum_{jk} \sum_{nm} \chi^{(2)}_{ijk}(\omega_n + \omega_m; \omega_n, \omega_m) E_j(\omega_n) E_k(\omega_m)\,, \tag{2.1.7}$$

where *ijk* are the Cartesian components of the fields.

2.2 The nonlinear optical wave equation

In this section, we investigate how new frequencies are generated by the nonlinear processes starting from the Maxell's equations [43]:

$$\nabla \cdot \vec{D} = \rho, \tag{2.2.1}$$

$$\nabla \cdot \vec{B} = 0, \tag{2.2.2}$$

$$\nabla \times \vec{E} = -\frac{\partial \vec{B}}{\partial t}, \tag{2.2.3}$$

$$\nabla \times \vec{H} = \frac{\partial \vec{D}}{\partial t} + \vec{J}. \tag{2.2.4}$$

Note that starts from this section, we always omit the accent ~, but keep the same assumptions. We are working with Gallium Phosphide (GaP) which is a semiconductor. Assuming it is a perfect semiconductor, it means without a pump, there are no free charges. Thus, in (2.2.1):

$$\rho = 0. \tag{2.2.5}$$

Also, there would be no free currents inside a GaP crystal, so in (2.2.4):

$$\vec{J} = 0. \tag{2.2.6}$$

Also the GaP is not a magnetic material. Thus,

$$\vec{B} = \mu_0 \vec{H}, \tag{2.2.7}$$

where μ_0 is the permeability of the free space. Since we are interested in the nonlinear effect inside the GaP crystal, in this sense, the relation between the electric displacement $\vec{D}$ and the electric field $\vec{E}$ is then:

$$\vec{D} = \epsilon_0 \vec{E} + \vec{P}. \tag{2.2.8}$$

We then derive the optical wave equation by taking the curl of (2.2.3):

$$\nabla \times \nabla \times \vec{E} = -\nabla \times \frac{\partial \vec{B}}{\partial t}. \tag{2.2.9}$$

Interchange the time and space derivative:

$$\nabla \times \nabla \times \vec{E} = -\frac{\partial (\nabla \times \overrightarrow{B})}{\partial t}. \tag{2.2.10}$$

Plug (2.2.7) into (2.2.10):

$$\nabla \times \nabla \times \vec{E} = -\mu_0 \frac{\partial (\nabla \times \overrightarrow{H})}{\partial t}. \tag{2.2.11}$$

Then, plug (2.2.4) into (2.2.11) and we get:

$$\nabla \times \nabla \times \vec{E} + \mu_0 \frac{\partial^2 \vec{D}}{\partial t^2} = 0. \tag{2.2.12}$$

From vector calculus, we know:

$$\nabla \times \nabla \times \vec{E} = \nabla\left(\nabla \cdot \vec{E}\right) - \nabla^2 \vec{E}. \tag{2.2.13}$$

For a transverse plane wave, $\nabla \cdot \vec{E} = 0$. In some cases, although the first term in (2.2.13) does not equal to 0, according to the slowly varying amplitude approximation [43], this term is negligible. Then, the Equation (2.2.12) becomes:

$$\mu_0 \frac{\partial^2 \vec{D}}{\partial t^2} - \nabla^2 \vec{E} = 0, \tag{2.2.14}$$

where $\vec{D} = \epsilon_0 \vec{E} + \vec{P}$, and in the nonlinear optics, the polarization $\vec{P}$ can be decomposed into the linear polarization and nonlinear polarization:

$$\vec{P} = \vec{P}^{(1)} + \vec{P}^{NL}, \tag{2.2.15}$$

and

$$\vec{P}^{(1)} = \epsilon_0 \chi^{(1)} \vec{E}. \tag{2.2.16}$$

As a result, the electric displacement $\vec{D}$ can be rearranged as:

$$\vec{D} = \epsilon_0 \left(1 + \chi^{(1)}\right) \vec{E} + \vec{P}^{NL} = \epsilon_0 \epsilon^{(1)} \vec{E} + \vec{P}^{NL}. \tag{2.2.17}$$

Here $\epsilon^{(1)}$is the relative permittivity tensor and in an isotropic material, it becomes a dimensionless scalar. Then it is linked to the linear refractive index *n* by $\epsilon^{(1)} = n^2$. Then the Equation (2.2.14) can be rewritten as:

$$\nabla^2 \vec{E} - \frac{\epsilon^{(1)}}{c^2} \frac{\partial^2 \vec{E}}{\partial t^2} = \frac{1}{\epsilon_0 c^2} \frac{\partial^2 \vec{P}^{NL}}{\partial t^2}. \tag{2.2.18}$$

Noting that, here the $\mu_0 \epsilon_0 = \frac{1}{c^2}$, where *c* is the speed of light in vacuum.

Now, we need to consider a more realistic case when the material is dispersive. In this case, we need to consider different frequency components of the light electric field separately.

We can decompose the electric field, and the nonlinear polarization into different frequency components and then sum them up. Then we can write:

$$\vec{E}(\vec{r}, t) = \sum_n{}' \vec{E}_n(\vec{r}, t) = \sum_n{}' \vec{E}_n(\vec{r}) e^{-i\omega_n t} + c.c\,, \tag{2.2.19a}$$

$$\vec{P}_{NL}(\vec{r},t) = \sum_n' \vec{P}_{NL}(\vec{r},t) = \sum_n' \vec{P}_{NL}(\vec{r})e^{-i\omega_n t} + c.c. \quad (2.2.19b)$$

The same expansion into different frequency components can also be applied to the linear displacement.

Plugging equations (2.2.19) into (2.2.18) we obtain:

$$\nabla^2 \vec{E}_n(r) + \frac{{\omega_n}^2 \epsilon^{(1)}(\omega_n)}{c^2} \vec{E}_n(r) = -\frac{{\omega_n}^2}{\epsilon_0 c^2} \vec{P}_{NL}(\vec{r}). \quad (2.2.20)$$

This equation is the coupled wave equation in the frequency domain, also known as the Helmholtz equation.

2.3 Coupled-wave equations for difference-frequency generation of THz radiation

The THz generation inside the nonlinear $\chi^{(2)}$ crystal is through difference-frequency generation (DFG) within a single NIR pulse. Such a process, also referred to as optical rectification (OR), involves DFG between high- and low-frequency components of a NIR pulse. This results in the production of a THz pulse oscillating at a frequency substantially lower than the NIR frequencies.

Below we consider the DFG in a lossless nonlinear optical medium with collimated, monochromatic, and continuous input beams at normal incidence.

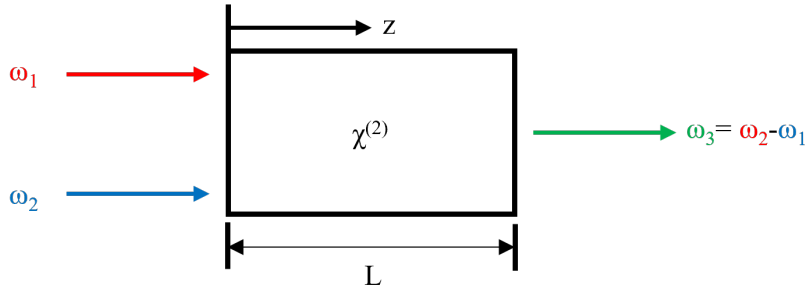

Fig. 2.1 Difference frequency generation in a second-order nonlinear medium. ω_1 and ω_2 are the frequency components of the 2 continuous input beams. ω_3 is the frequency generated from the DFG process. Figure adapted from [43].

The coupled wave equation we derived in the last section (Equation (2.2.20) should hold for each individual frequency component of the difference-frequency generation (ω_1 and ω_2) and of course valid for the difference-frequency component, ω_3. If we do not consider the nonlinear polarization

source term, the solution for Equation (2.2.20) is a plane wave propagating in the +z direction at ω_3:

$$E_3(z,t) = A_3 e^{i(k_3 z - \omega_3 t)} + c.c. \tag{2.3.1}$$

where k_3 is the wave vector:

$$k_3 = \frac{n_3 \omega_3}{c},\ {n_3}^2 = \epsilon^{(1)}(\omega_3). \tag{2.3.2}$$

Here A_3 is the amplitude of the electric field which is a constant. If we consider the nonlinear polarization term in Equation (2.2.20) is not too large, the solution to Equation (2.2.20) should still be of the form of Equation (2.3.1) but the amplitude A_3 will become a slowly varying function of the distance z.

We now can write the nonlinear polarization terms in Equation (2.2.20) as:

$$P_3(z,t) = P_3 e^{-i\omega_3 t} + c.c.. \tag{2.3.3}$$

According to Equation (2.1.7):

$$P_3 = 4\epsilon_0 d_{eff} E(\omega_1) E(\omega_2)^*, d_{eff} = \frac{1}{2}\chi^{(2)}. \tag{2.3.4}$$

Here for i=1 and 2, the electric field can be written as:

$$E_i(z,t) = E_i e^{-i\omega_i t} + c.c., and\ E_i = A_i e^{ik_i z}. \tag{2.3.5}$$

Plug equation (2.3.5) into (2.3.4) and we obtain the amplitude P_3:

$$P_3 = 4\epsilon_0 d_{eff} A_1 A_2^* e^{i(k_1 - k_2)z}. \tag{2.3.6}$$

We can then substitute the Equation (2.3.1), (2.3.3), and (2.3.6) into Equation (2.2.20). Since now we are in the 1D system in z, the Laplace operator ∇^2 can be replaced by $\frac{d^2}{dz^2}$ and the equation becomes:

$$\left[\frac{d^2A_3}{dz^2} + 2ik_3\frac{dA_3}{dz} - k_3^2A_3 + \frac{\omega_3^2}{c^2}\epsilon^{(1)}A_3\right]e^{i(k_3z-\omega_3t)} + c.c.$$
$$= \frac{-4d_{eff}\omega_3^2}{c^2}A_1A_2^*e^{i\left((k_1-k_2)z-\omega_3t\right)} + c.c. \quad (2.3.7)$$

Noting that:

$$k_3^2 = \frac{\omega_3^2}{c^2}\epsilon^{(1)}, \quad (2.3.8)$$

and eliminate the conventions on both sides of the equation. Then the Equation (2.3.7) becomes:

$$\frac{d^2A_3}{dz^2} + 2ik_3\frac{dA_3}{dz} = \frac{-4d_{eff}\omega_3^2}{c^2}A_1A_2^*e^{i(k_1-k_2-k_3)z}. \quad (2.3.9)$$

Now, we can have a look at the two terms on the left-hand side. We can usually assume that:

$$\left|\frac{d^2A_3}{dz^2}\right| \ll \left|k_3\frac{dA_3}{dz}\right|. \quad (2.3.10)$$

This is called slowly varying amplitude approximation which means the fractional change in A_3 within an optical wavelength must be much smaller than unity. Once we apply this approximation, we obtain:

$$\frac{dA_3}{dz} = \frac{2id_{eff}\omega_3}{n_3c}A_1A_2^*e^{i(k_1-k_2-k_3)z}. \quad (2.3.11)$$

Here the n_3 is the refractive index of ω_3, which in our case is the THz frequency.

Now we can take a look at the term:

$$\Delta k = k_1 - k_2 - k_3, \quad (2.3.12)$$

This is the difference between the 3 wavevectors involved in the nonlinear process and we call it wavevector mismatch which is essentially the momentum mismatch.

Now Equation (2.3.11) can be written as:

$$\frac{dA_3}{dz} = \frac{2id_{eff}\omega_3}{n_3c}A_1A_2^*e^{i\Delta kz}. \quad (2.3.13)$$

This equation describes the variation of the electric field amplitude at frequency ω_3 which is THz frequency in our case. We can see that the terms before the $e^{i\Delta kz}$ are all constants assuming that A_1

and A_2^* do not change throughout the z direction. The key term here is the $e^{i\Delta kz}$ which we call it phase matching term. In the next section, we will discuss the phase-matching condition and see how it affects the THz generation and how we can overcome the constraints arising from it.

2.4 Phase-matching condition

We first consider the case when:

$$\Delta k = 0. \tag{2.4.1}$$

Equation 2.3.13 then becomes:

$$\frac{dA_3}{dz} = \frac{2id_{eff}\omega_3}{n_3 c} A_1 A_2^*. \tag{2.4.2}$$

The above equation has a solution:

$$A_3 = \frac{2id_{eff}\omega_3}{n_3 c} A_1 A_2^* z. \tag{2.4.3}$$

This means the amplitude of the generated electric field (in our case, the THz field) will increase linearly with the distance z, and the intensity of the THz beam increases quadratically with the distance z. Therefore, if we have a crystal that satisfies the perfect phase matching condition ($\Delta k = 0$), the THz created at different positions z inside the crystal are in phase. Hence, the thicker the crystal is, the stronger will be the THz beam generated.

We next consider the case $\Delta k \neq 0$. Integrating equation (2.3.13) from $z = 0$ to $z = L$ gives:

$$A_3(L) = \frac{2id_{eff}\omega_3}{n_3 c} A_1 A_2^* \int_0^L e^{i\Delta kz}\, dz = \frac{2id_{eff}\omega_3}{n_3 c} A_1 A_2^* \left(\frac{e^{i\Delta kL} - 1}{i\Delta k}\right). \tag{2.4.4}$$

The intensity of the THz at $z = L$ is given by the time average of Poynting vector:

$$\begin{aligned} I_3 = 2n\epsilon_0 c\left|{A_3}^2\right| &= \frac{8n_3\epsilon_0 {d_{eff}}^2 {\omega_3}^2 |A_1|^2 |A_2|^2}{{n_3}^2 c} \left|\frac{e^{i\Delta kL}-1}{i\Delta k}\right|^2 \\ &= \frac{2{d_{eff}}^2 {\omega_3}^2 I_1 I_2}{n_1 n_2 n_3 \epsilon_0 c^3} L^2 sinc^2\left(\frac{\Delta kL}{2}\right), \end{aligned} \tag{2.4.5}$$

where:

$$sinc^2\left(\frac{\Delta kL}{2}\right) \equiv \frac{\sin^2(\frac{\Delta kL}{2})}{\left(\frac{\Delta kL}{2}\right)^2}. \tag{2.4.6}$$

We can define $L_{coh} = \frac{2}{\Delta k}$. When the distance z is larger than L_{coh}, the THz starts to get out of phase with the THz field generated at the $L = 0$.

Then, the phase mismatch factor can be written as:

$$sinc^2\left(\frac{L}{L_{coh}}\right). \tag{2.4.7}$$

We plot the $sinc^2$ function below.

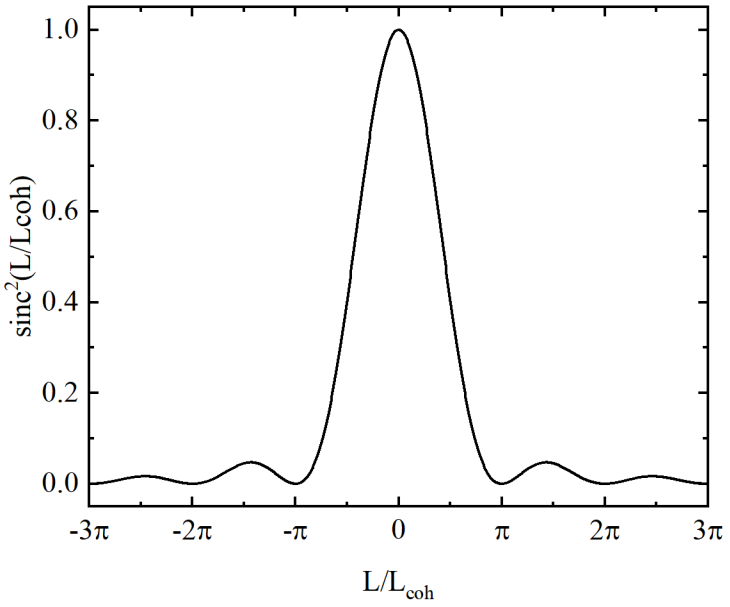

Fig. 2.2. Effects of wavevector mismatching on the efficiency of the difference-frequency generation. Figure adapted from [43].

Let's have a closer look at the wavevector mismatch for THz generation:

$$k_{NIR+THz} - k_{NIR} = k_{THz}, \tag{2.4.8}$$

and the energy conservation:

$$\omega_{NIR+THz} - \omega_{NIR} = \omega_{THz}. \tag{2.4.9}$$

In the THz generation process, we have:

$$\omega_{THz} \ll \omega_{NIR}, \omega_{NIR+THz}. \tag{2.4.10}$$

Then if we divide the Equation (2.4.8) by (2.4.9) and multiply the speed of light c on both sides:

$$c\frac{k_{NIR+THz}-k_{NIR}}{\omega_{NIR+THz}-\omega_{NIR}}=c\frac{k_{THz}}{\omega_{THz}}. \tag{2.4.11}$$

The right-hand side is simply the (phase) refractive index of the THz in the nonlinear medium. On the left-hand side, since the ω_{THz} is very small compared to ω_{NIR}, we can write the division in the form of a derivative:

$$c\ \frac{dk_{NIR}}{d\omega_{NIR}}=\frac{c}{v_{gNIR}}=n_{gNIR}. \tag{2.4.12}$$

This is the well-known criteria for perfect phase matching condition for THz generation: the group index of the NIR generation beam should be equal to the phase index of the THz beam in the nonlinear medium (THz crystal), or equivalently, the group velocity of the NIR beam should be equal to the phase velocity of the THz in the nonlinear medium (THz crystal):

$$n_{gNIR}=n_{THz}\text{ or }v_{gNIR}=v_{THz}. \tag{2.4.13}$$

2.5 Tilted-pulse-front phase matching

We have seen the importance of the phase-matching conditions for the second-order nonlinear processes in the previous section (in our case OR/DFG). As we discussed in the former sections, the perfect phase-matching condition for THz generation is that the group index of the NIR pulse equals to the phase index of the THz frequency to be generated. However, this condition is not always satisfied in the THz crystals for all the desired THz frequencies. The tilted-pulse-front phase matching [44–46] is one of the ideas to adjust the generation configuration to adjust the phase matching inside the generation crystal to achieve a perfect phase matching at demanding frequencies.

The tilted-pulse-front phase matching is similar to the Cherenkov phase-matching [47–49] observed in the 1980s. The Cherenkov THz generation shown in Fig. 2.3. happens when the group velocity of a tightly focused NIR generation pulse is larger than the phase velocity of the THz pulse. It is an automatically satisfied noncollinear phase-matching [49]. The THz generated is in a cone

shape which is known as the Cherenkov cone with a critical angle θ_c between the propagation directions of the NIR pulses and the THz pulses:

$$\theta_c = \cos^{-1}\left(\frac{v(\Omega)}{v_g(\omega_0)}\right), \tag{2.5.1}$$

where $v(\Omega)$ is the phase velocity of the generated THz beam and $v_g(\omega_0)$ is the group velocity of the NIR generation beam.

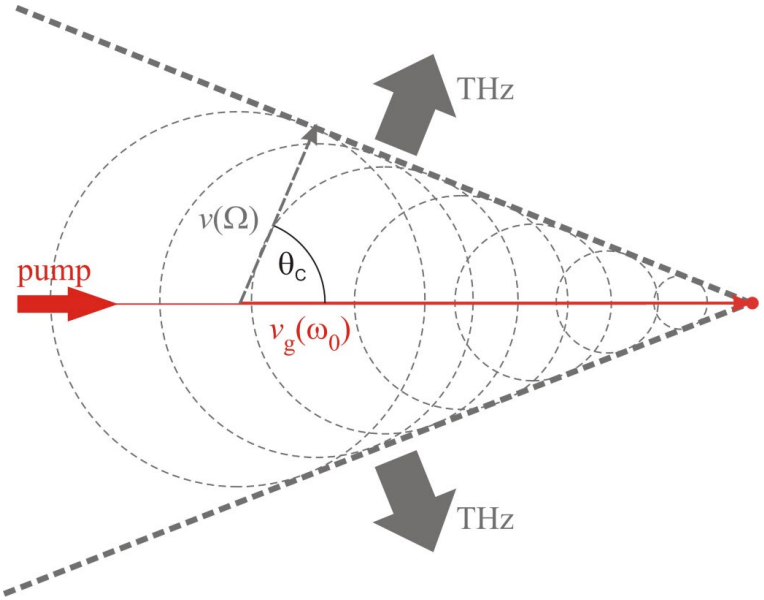

Fig. 2.3 Cherenkov THz generation resulting from OR of a fs optical pulse moving at a velocity $v_g(\omega_0)$ larger than the phase velocity of the generated THz $v(\Omega)$ [50].

Also, the phase-matching condition is automatically satisfied in the Cherenkov geometry and the THz radiation is generated in a cone shape which is hard to collect and guide for applications [46]. Also, the Cherenkov geometry requires a focused NIR beam which is not friendly to the high-field THz generation where the NIR generation beam is always collimated [47,50].

The tilted-pulse-front geometry is constructed by making the intensity front of the NIR plane wave align with one of the Cherenkov lines (thick dashed lines in Fig. 2.3). According to the Huygen-Fresnel principle, every point on the wave front of a propagating electromagnetic wave can be considered as a point emitter. The THz beam generated by each point emitter on the NIR intensity

front constructively interferes with each other as the traveling speed of the intensity front of the NIR beam matches with the phase velocity of the generated THz beam.

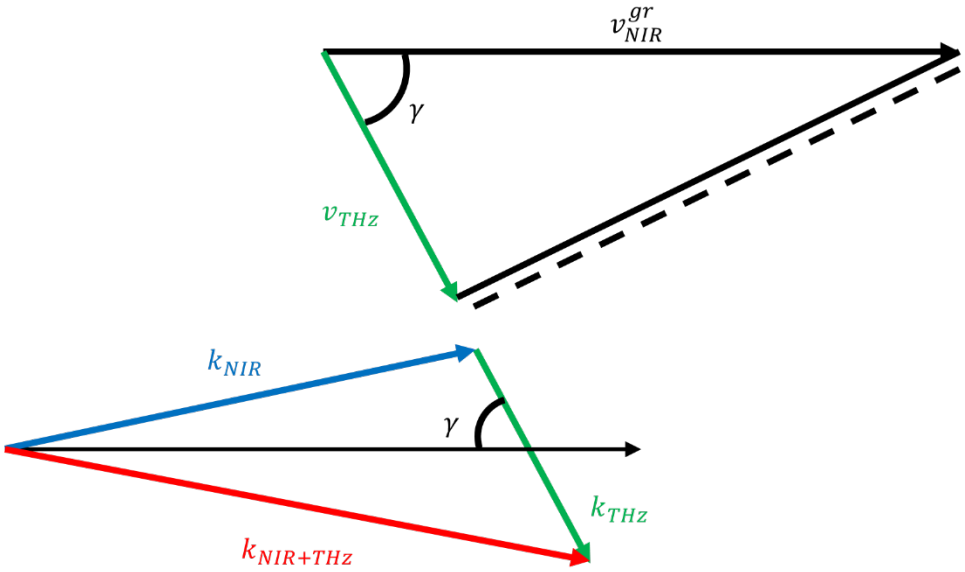

Fig. 2.4 The schematic of the tilted-pulse-front technique. The top part of the figure shows the propagation direction of the NIR pulse and the generated THz pulse. The bottom part of the figure shows the phase-matching in the tilted-pulse-front configuration. Figure adapted from [46].

Figure 2.4 shows that by tilting the pulse front of the NIR generation pulse, we make the THz generated perpendicular to the pulse front of the NIR pulse instead of along the direction of the NIR pulse. As a result, the generated THz pulses form an angle γ with the propagation direction of the NIR generation pulse. The collinear phase-matching condition is:

$$\Delta k = k_{NIR+THz} - k_{NIR} - k_{THz}. \tag{2.5.2}$$

The tilted-pulse-front phase-matching condition is:

$$\Delta k = \frac{k_{NIR+THz} - k_{NIR}}{\cos\gamma} - k_{THz}. \tag{2.5.3}$$

According to the linear diffraction property of the nonlinear material, we can adjust the angle of the pulse front tilt according to:

$$\theta = \cos^{-1}\frac{n_g(\omega_{NIR})}{n(\omega_{THz})}. \tag{2.5.4}$$

A typical tilted pulse front THz generation system uses a grating and one or two lenses to image the grating onto the front surface of the generation crystal. During my PhD, I was involved in 2 projects using a tilted pulse front THz generation setup built by Dr. Lauren Gingras which I have reoptimized and operated, leading to 2 publications [51,52]. The schematic of the tilted pulse front THz generation system I have operated is shown in Fig. 2.5.

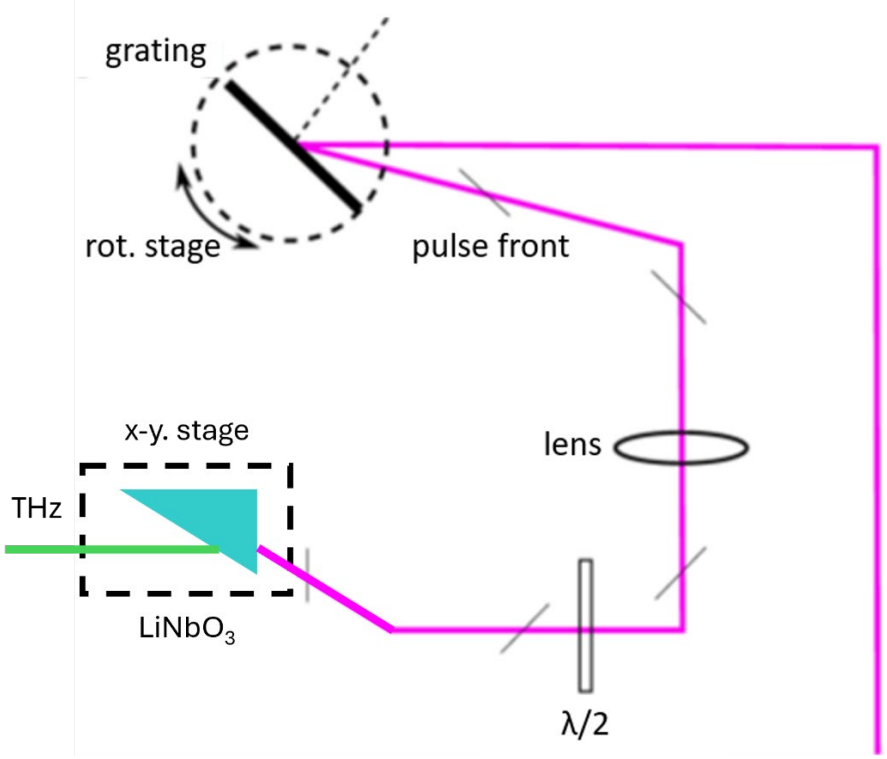

Fig. 2.5 Tilted-pulse-front THz generation system in our lab. A grating tilted the pulse front and imaged by a lens onto the front surface of the generation crystal. Figure adapted from [53].

The alignment of such a system is complicated and the THz generation efficiency is affected by the imaging distortion due to the lens [54]. Physicists have been working on eliminating this imaging distortion by optimizing the imaging system. Also, another idea is to avoid imaging the grating onto the front surface of the generation crystal, but instead, to fabricate a grating on the front surface of the generation crystal to directly tilt the pulse front of the NIR generation beam [54–58]. The

contact grating is the component of the 2 main projects for my PhD and will be explained in detail in Chapter 5 and 6.

2.6 THz detection

The detection technique for the THz experiment in my PhD work is called electro-optical sampling (EOS), which was invented almost simultaneously by 3 groups in 1996 [36–38]. This technique also utilizes the second-order nonlinearity in non-centrosymmetric crystals. The nonlinear effect used in the EOS technique is called the Pockels effect or Pockels electro-optic effect and can be considered as the reciprocal process of optical rectification in the THz generation process. The Pockels effect describes the change in refractive index for electric polarizations along different axes of a nonlinear crystal caused by a DC electric field.

For a zincblende crystal, such as GaP and ZnTe, when an electric field is applied on the crystal, the crystal's ellipsoid of the refractive index changes according to [41]:

$$\frac{x^2 + y^2 + z^2}{{n_0}^2} + 2\gamma_{41}E_x yz + 2\gamma_{41}E_y zx + 2\gamma_{41}E_z xy = 1, \tag{2.6.1}$$

where n_0 is the crystal's refractive index without the electric field; x, y, z are the coordinate units of the refractive index ellipsoid, E_x, E_y, E_z are the components of the electric field along the x, y, z directions and γ_{41} is the electro-optical coefficient of the nonlinear crystal.

When light of wavelength λ is transmitted through such a nonlinear crystal of thickness d and experiences this refractive index change, a phase delay Γ is created according to:

$$\Gamma = \frac{2\pi d}{\lambda}\Delta n. \tag{2.6.2}$$

In our case, the detection crystal is a <110> cut GaP and the NIR beam is normally incident into the detection crystal. The phase delay can be expressed as [17]:

$$\Gamma = \frac{\pi d {n_0}^3 r_{41} E}{\lambda}\sqrt{1 + 3sin^2\phi}, \tag{2.6.3}$$

where ϕ is the angle between the electric field and the <001> axis of the detection crystal.

When a gating beam with an intensity I_0 interacts with the electric field in the gating crystal, the signal on the balanced detector is:

$$S = I_0 \sin 2\phi \sin \Gamma \approx I_0 \Gamma \sin 2\phi\,, \tag{2.6.4}$$

assuming that the phase delay induced by the change the electric field is small.

The above discussions treat the THz electric field as a DC field. In electro-optical sampling, the THz pulse acts as the "DC electric field" to change the polarization of the NIR gating pulses since the THz pulse is of a period of ps, which is much longer than that of a fs NIR gating pulse. In this case, this process involves 2 more processes. The first one is the nonlinear interaction between the NIR gating beam and the THz beam through sum-frequency generation (SFG) and DFG. This part can be considered as the reciprocal process of the DFG happening in the THz generation process. Thus, its derivation is similar to that of the THz generation through DFG. We just need to look into the phase-matching condition for the SFG and DFG here.

For DFG, the phase-matching condition is:

$$\Delta k_{DFG} = k_{NIR} - k_{THz} - k_{NIR-THz}. \tag{2.6.5}$$

This can be derived into:

$$\Delta k_{DFG} = \frac{k_{NIR} - k_{NIR-THz}}{\omega_{THz}} \omega_{THz} - k_{THz}. \tag{2.6.6}$$

Since $\omega_{THz} \ll \omega_{NIR}$, the equation above can be further written as:

$$\Delta k_{DFG} = \left(\frac{dk}{d\omega}\right)_{\omega_{NIR}} \omega_{THz} - k_{NIR-THz} = \frac{\omega_{THz}}{v_{g_{NIR}}} - k_{NIR-THz}. \tag{2.6.7}$$

Similarly, for SFG, the phase-matching can also be written as:

$$\Delta k_{SFG} = k_{NIR+THz} - k_{NIR} - k_{THz} = \frac{\omega_{THz}}{v_{g_{NIR}}} - k_{NIR-THz}. \quad (2.6.8)$$

We can see that, in the approximation that $\omega_{THz} \ll \omega_{NIR}$, the phase-matching conditions of the DFG and SFG are equivalent to each other. As a result, the phase-matching conditions contribute to a term below in the EOS THz detection:

$$f_{phase-matching} = \frac{e^{i\Delta kL} - 1}{i\Delta k}. \quad (2.6.9)$$

Another factor in EOS is the spectral autocorrelation between the initial gating beam and the generated NIR beam in the SFG and DFG process [59]. This term can be written as:

$$A_{opt}(\omega_{THz}) = \int_{-\infty}^{+\infty} A^*(\omega_{NIR}) A(\omega_{NIR-THz}) d\omega \,. \quad (2.6.10)$$

This spectral autocorrelation term describes the fact that the EOS detection efficiency drops as the NIR gating beam is red-/blue- shift away from the original wavelength through DFG and SFG processes.

One more factor to be considered is the phonon resonances in the desired THz detection spectral range. The first phonon absorption for ZnTe is at 5.3 THz and that for GaP is at 11 THz [41]. For efficient THz detection from 0.5 to 6.5 THz, we choose GaP as the detection crystal.

2.7 Extraction of real refractive index and the absorption coefficient using THz-TDS

The direct application of the THz-TDS system is to measure the linear dispersion information of a given material in the THz range. The following part references [60]. The way it works is to put the sample under investigation at the THz focus of the THz-TDS system at THz field strengths not strong enough to induce extra nonlinear effects and take a reference measurement subsequently under the same conditions with the sample removed. When a sample is put inside the THz beam, as shown in Fig. 2.6(a) in the time domain, the measured THz pulses will be delayed by a certain

amount according to the material's real refractive index and thickness. Also, the amplitude of the THz signal is attenuated due to the absorption inside the material as well as the Fresnel transmission of the THz beam through material-air interfaces. The absorption coefficient of the material is frequency dependent. Thus, by performing a Fourier transform on to the time-domain reference and sample signal (see Fig. 2.6(b)), the frequency dependent absorption coefficient can be calculated accordingly.

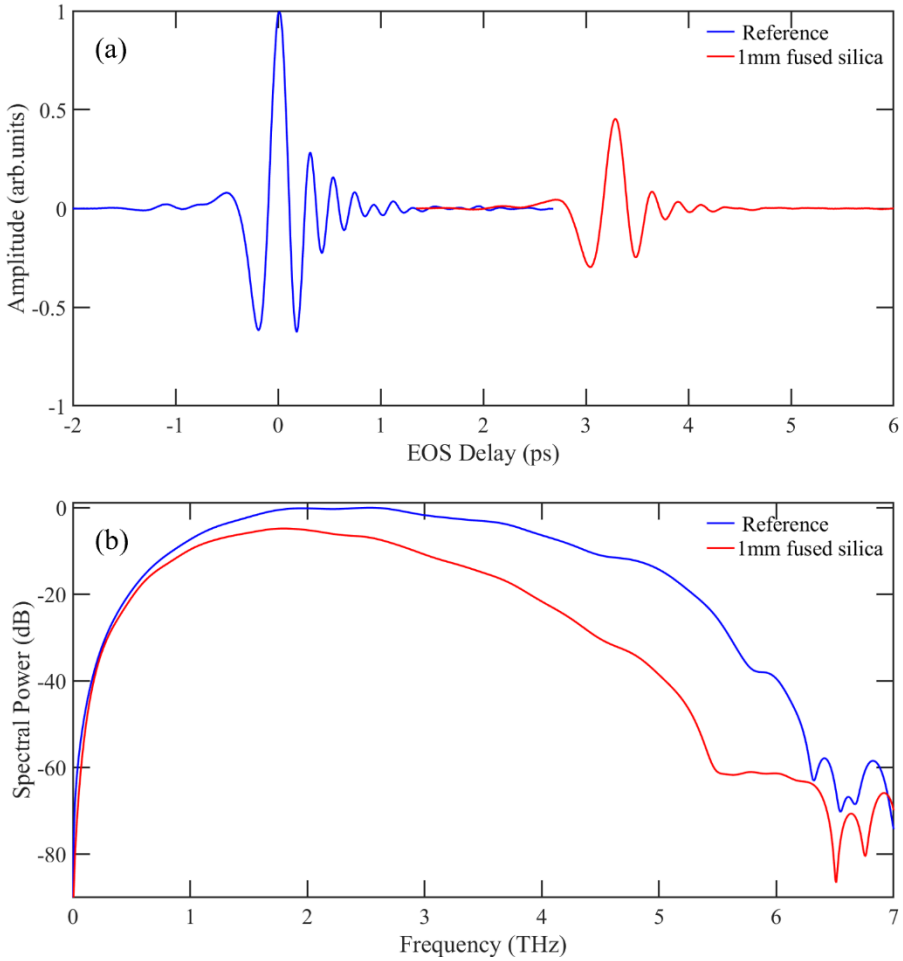

Fig. 2.6 (a) Time-domain signal of THz pulses with no sample in the THz-TDS system (reference signal) and the time-domain signal measured after the THz pulse transmitted through a 1 mm-thick fused silica sample. (b) The Fourier transform of the reference signal and the sample signal.

When a THz pulse $E_0(\omega)$ transmits through a sample with a thickness d, the resulting THz pulse $E_s(\omega)$ can be represented as:

$$E_s(\omega) = T(\varepsilon_\omega)E_0(\omega)e^{-ik_s(\omega,\varepsilon_\omega)d}, \tag{2.7.1}$$

where ω is the frequency of the THz pulse; $T(\varepsilon_\omega)$ is the Fresnel transmission coefficient account for the THz transmission through the air-material interfaces; $k_s(\omega,\varepsilon_\omega)d$ is the phase delay created from the transmission through the materials itself. The sample signal can be further written as:

$$E_s(\omega) = \frac{4\tilde{n}_{s(\omega)}}{\left(1+\tilde{n}_{s(\omega)}\right)^2}E_0(\omega)e^{-i\frac{\tilde{n}_s(\omega)\omega}{c}d}, \tag{2.7.2}$$

where $\tilde{n}_{s(\omega)} = n_s(\omega) - i\kappa_s(\omega)$ is the complex refractive index of the material in the THz range. For the reference signal we measured in the THz-TDS system, it can be considered that the initial THz pulse transmits through a slab of air with the same thickness as the sample material:

$$E_r(\omega) = E_0(\omega)e^{-i\frac{\omega}{c}d}, \tag{2.7.3}$$

where c is the speed of light in air.

From the information above, we can calculate the total transmission function of the THz pulse:

$$H(\omega) = \frac{E_s(\omega)}{E_r(\omega)} = \frac{4\tilde{n}_{s(\omega)}}{\left(1+\tilde{n}_{s(\omega)}\right)^2}e^{-i\frac{(n_s(\omega)-1)\omega}{c}d}e^{-\kappa_s\frac{\omega}{c}d}. \tag{2.7.4}$$

We can assume that $n_s(\omega) \gg \kappa_s(\omega)$, which means the absorption of the material in the sample is weak. Thus, the complex refractive index, $\tilde{n}_{s(\omega)}$can be approximated as the real refractive index, $n_s(\omega)$.

Then, the total transmission function gets simplified to:

$$H(\omega) = \frac{4n_s(\omega)}{\left(1+n_s(\omega)\right)^2}e^{-i\frac{(n_s(\omega)-1)\omega}{c}d}e^{-\kappa_s\frac{\omega}{c}d}. \tag{2.7.5}$$

The absolute value of the transmission function (take the natural logarithm of this value) is:

$$\ln|H(\omega)| = \ln\left(\frac{4n_s(\omega)}{\left(1+n_s(\omega)\right)^2}\right) - \kappa_s(\omega)\frac{\omega}{c}d. \tag{2.7.6}$$

The phase of the complex-valued total transmission function is

$$\angle H(\omega) = \frac{(n_s(\omega) - 1)\omega}{c} d. \tag{2.7.7}$$

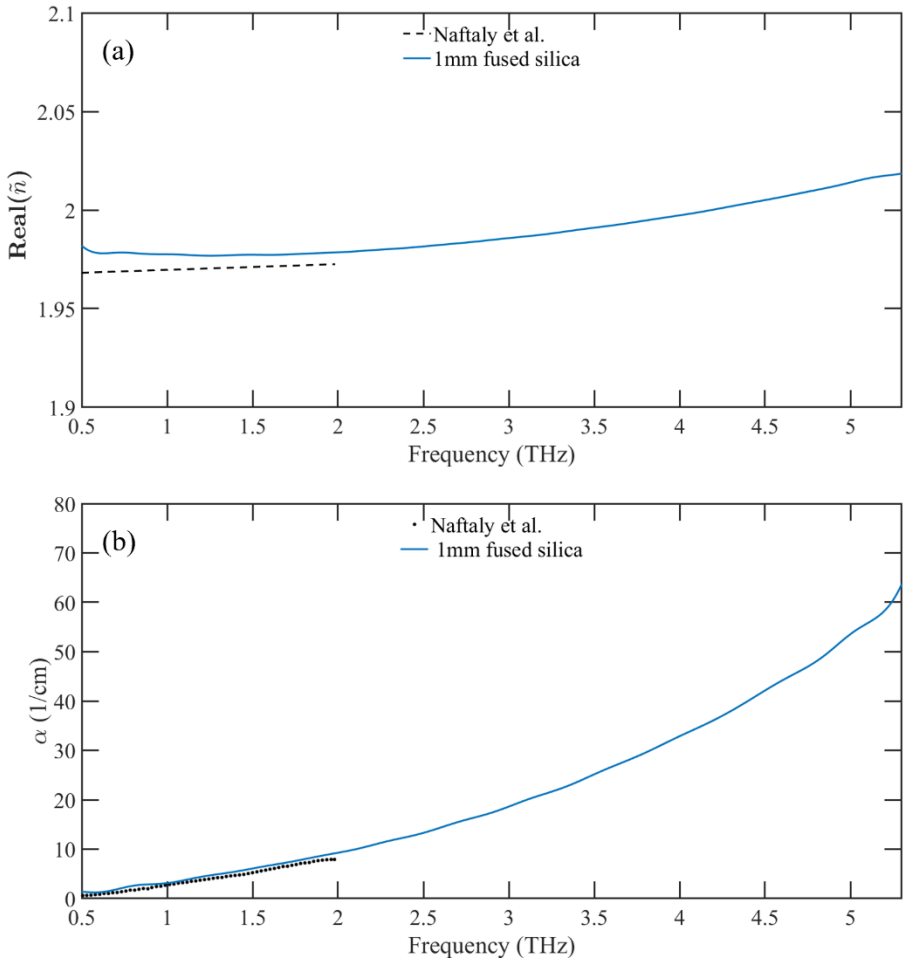

Fig. 2.7. With the measurements presented in Fig. 2.6, (a) the refractive index and (b) the absorption coefficient of the 1 mm-thick UV fused silica is extracted. The results are compared with the Ref [61].

As a result, once we can obtain the absolute value and the phase of the total transmission function from the THz-TDS measurement. We can calculate the real refractive index and absorption coefficient of the sample material according to the equations:

$$n_s(\omega) = 1 - \frac{c}{\omega d}\big(\angle H(\omega)\big), \tag{2.7.8}$$

$$\kappa_s(\omega) = \frac{c}{\omega d}\left(\ln\left(\frac{4n_s(\omega)}{\big(1 + n_s(\omega)\big)^2}\right) - ln|H(\omega)|\right). \tag{2.7.9}$$

The power absorption coefficient is:

$$\alpha_s(\omega) = 2\frac{\omega\kappa_s}{c}. \tag{2.7.10}$$

In real applications, the $|H(\omega)|$ is the ratio between the spectral amplitudes of the sample signal and the reference signal. The $\angle H(\omega)$ can be obtained by using the "angle" function (in Matlab) on the result of calculated $H(\omega)$.

Applying the aforementioned theory, we calculated the refractive index and absorption coefficient of the 1mm-thick fused silica, as depicted in Fig. 2.7. Our measurements for the refractive index and the absorption coefficient align closely with those reported in Ref [61] from 0.5 to 2 THz. Notably, our specialized THz-TDS system, elaborated upon Chapter 5, offers linear dispersion information of the fused silica in the 2 to 6 THz range with a peak dynamic range of 90 dB (shown in Fig. 2.6(b)), a capability not typically found in standard THz-TDS system available commercially.

Chapter 3

Experimental methods

In the following sections, we discuss the experimental methods used to collect the data presented in this thesis. We provide a concise overview of the amplified NIR femtosecond pulse generation and focus primarily on the construction and operation of a THz-TDS system. Several experiments characterizing the THz-TDS system are presented, and some specific experimental tricks developed during my PhD study will be elaborated upon.

3.1 Amplified femtosecond Yb:KGW laser system

As discussed in the previous chapters, using an amplified NIR femtosecond pulse for THz generation and detection is one of the most efficient methods for mode-locked THz pulse generation and detection. Perhaps the most well-known method of achieving ultra-short pulses with millijoule pulse energy is the chirped-pulse amplification (CPA) of broadband and low-intensity NIR pulses, illustrated in Fig. 3.1. This method garnered significant attention since its invention and especially after the 2018 Nobel prize awarded to Arthur Ashin, Gérard Mourou and Donna Strickland. Dr. Gérard Mourou and Dr. Donna Strickland, inventors of the chirped-pulse amplification method, indirectly laid the foundation for the research on THz time-domain spectroscopy based on nonlinear optics methods. Since the CPA technique has been extensively covered in scientific and popular literature, we focus here only on the parameters of the laser amplifier used for our experiments.

The femtosecond laser system in our lab is the Pharos laser system (Light Conversion, Ltd. Model PH1-SP-1.5 mJ). Part of the system includes an oscillator using Yb:KGW crystal generating 90 fs (FWHM) pulses at a wavelength of 1035 nm. The oscillator's repetition rate is 76 MHz and it outputs, at full average power, around 3.5 W. In addition to this 3.5 W laser power, another 1 W of laser power from the oscillator is directed into the regenerative amplifier (RA), which employs the

CPA method to amplify the pulse energy of the NIR pulses. The gain medium in this RA is also Yb:KGW. This system is a closed-box system, eliminating the need for regular alignment.

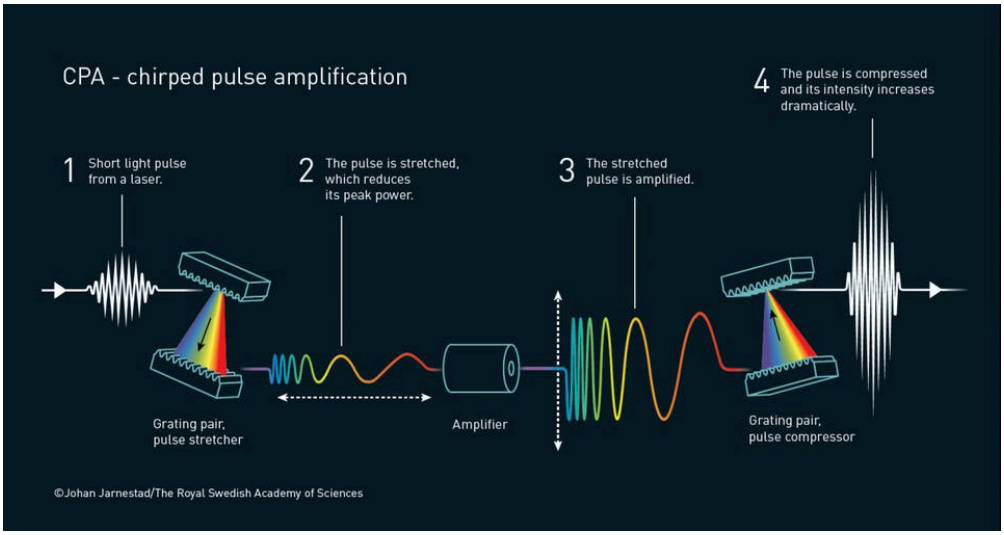

Fig. 3.1 Schematic illustration of the chirped pulse amplification used in a regenerative amplifier. Credits: Royal Swedish Academy of Sciences.

A warm-up time of 1 hour suffices for most experiments. The RA of the Pharos laser produces NIR pulses with a full average power of 6 W and its repetition rate can range from 6 kHz to 1.1 MHz. There is also a special mode where the RA can generate 4.5 W average power at 3 kHz, corresponding to the laser's highest pulse energy, 1.5 mJ. The high repetition rate mode of this RA is ideal for operating the THz-TDS system with a high signal-to-noise ratio since more pulses are measured per unit time. The low repetition rate is suitable for generating high-field THz for nonlinear experiments. The minimal pulse duration can be generated from the RA is 180 fs. Additionally, we can adjust the compressor in the RA system to add positive and negative chirp to the NIR pulses depending on the experimental needs.

3.2 THz time-domain spectroscopy system

The schematic of the first THz system is depicted in Fig. 3.2. Since we have already described the THz time-domain spectroscopy in general terms in Chapter 1, here we delve deeper into the details and considerations of building the system.

3.2.1 Reference iris pair

The NIR beam emitted from Pharos Yb:KGW amplifier first passes through 2 irises positioned roughly 2 feet away from each other. These 2 irises serve as a reference of the entire system, with their height determining the beam height of the whole THz-TDS system. Generally, the lower the optical components are at, the more stable the system will be since lower height reduces the effect of vibration and airflow on the optics. However, we must also account for other system components whose height is challenging to adjust, such as the translational stage and the parabolic mirrors. Once the system is well-aligned and before any measurements are taken, ensuring the incident NIR beam passes through the center of both irises indicates the setup is ready, providing no modifications were made to the components beyond these 2 irises. For the initial alignment of the THz-TDS system, we utilize a visible laser diode as it saves time compared to using an IR-viewer. Additionally, since the parabolic mirrors guiding the THz beam are free of chromatic aberration, the optical paths for visible and THz beams overlap under such a component. Aligning the NIR beam through the iris pair involves two mirrors placed before the first iris. The mirror farther from the first iris aligns the beam through the first iris, while the mirror closer to the first iris aligns the beam through the second iris. Typically, we have to adjust these 2 mirrors repeatedly to ensure the NIR beam passes through the centers of both irises. It is crucial to note that when aligning the beam through the second iris, the first iris must be fully open. A helpful tip for faster alignments is to position the mirror before the first iris as close as possible to it, ensuring the other mirror is not too close to the first one.

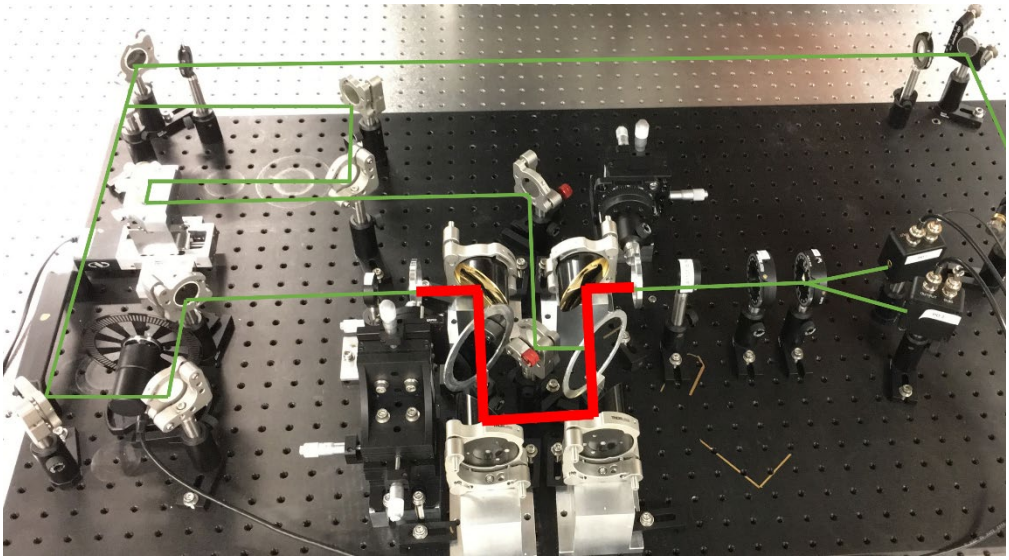

Fig. 3.2 The first THz-TDS system in our lab. The NIR beams at 1035 nm are shown in green and the THz beams are in red. The NIR beam is split into two arms. The first arm with 80% of the original power, generates THz using nonlinear crystals. The second arm with 20% of the original power serves as a gating beam to time-resolve the THz beam on the detection crystal through electro-optical sampling.

3.2.2 Parabolic mirrors

The NIR beam is then split into 2 arms. The first arm is focused on a generation crystal with a beam size of 27 μm ($1/e^2$ diameter) to generate THz. Since the THz wavelength is typically larger than the NIR focus size, the THz beam can be considered nearly a perfect point source. The first off-axis parabolic mirror then collects as much of the generated THz as possible. We use the metallic parabolic mirror to guide the THz beam because the THz beam's broad bandwidth causes chromatic aberration if regular lenses are used. Moreover, compared to lenses, parabolic mirrors can effectively reduce the energy loss in the THz band.

Aligning the off-axis parabolic mirror is one of the most challenging tasks for the THz time-domain system. The initial step is to ascertain the correct rotational position for the parabolic mirror within its mirror mount. To my knowledge, there are 3 distinct methods to achieve this. Typically, at least two of these methods are combined for verification.

Method 1: As shown in Fig. 3.3, the back of a parabolic mirror has three collinear holes. These three holes can serve as a reliable reference for the parabolic mirror's rotational position. When the center of these 3 holes align at the same height, it indicates the rotational position of the parabolic mirror is correct.

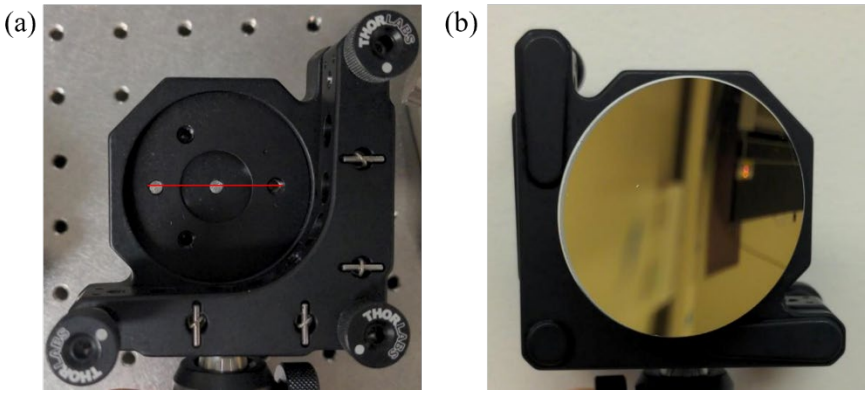

Fig. 3.3 Image of a typical 2" diameter and 2" focal length parabolic mirror. (a) The back view of the parabolic mirror. The red line connecting the three 3 holes serves as a reference for the rotational position of the parabolic within its mirror mount. (b) The front view of the parabolic mirror. Collimated beams of the height of the parabolic mirror will be focused into a horizontal line in the beam profile if it strikes the left side of the parabolic mirror and into a vertical line if it hits the right side of the parabolic mirror.

Method 2: A perfectly metal block vertical surface can be placed against the circular edge of the parabolic mirror. If no gap exists between the parabolic mirror's edge and the vertical surface, the rotation position of the parabolic mirror is correct.

Method 3: A circular beam at the height of the parabolic mirror center can be shone horizontally onto the mirror. Based on experimental observations, when the beam strikes the left side of the parabolic mirror, it forms a line shape (a very flat ellipse horizontally) in the far field. If this line is perfectly horizontal and at the height of the parabolic mirror's center, it indicates the rotational position of the parabolic mirror is correct.

For the alignment of the first parabolic mirror, another pair of irises, the same height as the first pair, can help ensure that the incident beam entering the first parabolic mirror follows a series of

straight holes on the optical table. We then insert the lens, which focuses the NIR beam onto the generation crystal, into the incident NIR beam, ensuring the beam after the lens remains straight and at the correct height. It is advisable to mount the focusing lens on a translational stage that moves along the incident visible beam, as the lens's dispersion difference must be compensated after switching to the 1035 nm laser. Instead of inserting the generation crystal, a 25 μm diameter pinhole can be placed at the focal point of this lens. This pinhole creates circular ring diffraction patterns in the visible beam, aiding in observing beam profile distortions when the parabolic mirrors are misaligned. We position the parabolic mirror a distance of its focal length away from the pinhole to collimate the expanding visible beam. The collimated NIR beam has to be perpendicular to the incident beam and remains collimated over a long distance and exhibits perfect circular diffraction patterns in its profile. This process requires fine-tuning the position and direction of the parabolic mirror manually. It is easier if the parabolic mirror is mounted on a heavy base and having a second person to check the far-field beam profile can expedite the entire process. The alignment of the second parabolic mirror has the same requirements as the first, except the outcoming beam is focusing and then expanding. The third parabolic mirror's alignment mirrors the first one and the fourth's alignment mimics that of the second. A useful tip to make sure that parabolic mirrors reflect the incident beam by 90° is to have the incident beam along a series of holes on the optical table in a straight line. A pair of irises of the correct height in the perpendicular direction can assist in positioning the parabolic mirrors.

3.2.3 Motorized translational delay stage

In our system, the motorized translational delay stage is in the other arm, known as the gating line. Its role is to adjust the beam path of the gating line, making it shorter or longer than the generation line in increments. This allows us to use the femtosecond gating pulse to time-resolve the longer picosecond THz pulse in time steps. Before installing the motorized translational delay stage, it is crucial to premeasure the designed beam path lengths of both the generation and gating lines. The

translational stage's middle point should correspond to the point where both beam lines have identical path lengths.

When the translational stage moves, the outgoing beam should remain unaffected by the translation. Otherwise, as the stage moves, the gating beam will lose its spatial overlap with the THz beam. The technique to align the translational stage is illustrated in Fig. 3.4.

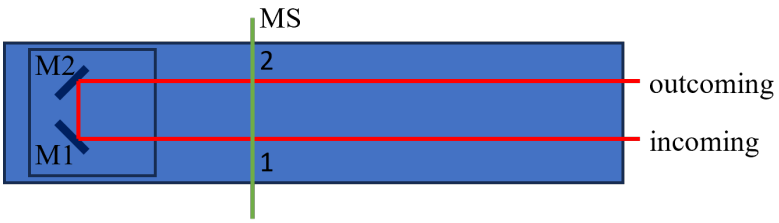

Fig. 3.4 The schematic for the alignment of the motorized translational stage. The red line indicates the beam path within the translational stage. M1: mirror 1; M2: mirror 2; MS: microscope slide. Points 1 and 2 mark the 2 intersection points between the optical beam and the MS.

To align the translational stage, the first thing is to align the incoming beam along the movement direction of the translational stage. We can then insert the microscope slide in the beam line, adjusting the microscope slide so that the reflection of the incoming beam overlaps with the incoming beam itself. Semi-transparent mirror paper can be used to verify beam overlap. The next steps involve adjusting M1 and M2 to ensure the beam reflected at point 2 overlaps with the incoming beam at point 1. The final step is to move the translational stage from one end to the other to double-check the pointing of the beam in the far field.

3.2.4 Spatial overlap of 2 beams on the gating crystal

Another crucial component of the THz-TDS system is the spatial overlap between the THz beam and the NIR gating beam on the gating crystal. As mentioned earlier, the parabolic mirror guiding the THz beam is free from chromatic aberration. This means the beam path of the visible alignment laser aligns with the THz beam when guided by the parabolic mirrors. To make sure the spatial overlap between the generation and the gating beam, once the 4 parabolic mirrors are well aligned,

we can place another pinhole at the focus of the 4th parabolic mirror. Then we can insert in the silicon wafer, adjusting both the silicon wafer and the mirror preceding the silicon wafer to ensure the gating beam is also focused by the 4th parabolic mirror into the pinhole and the height of the beam after the pinhole remains the same. This guaranteed the spatial overlap.

3.2.5 EOS alignment

The last part is the EOS. For the EOS, the most crucial part is balancing the photodetector. When balancing the photodetectors, we only insert the Wollaston prism into the gating beam line, adjusting it until the weaker of the two output beams reaches its minimum power by with the help of the IR viewer. To further verify this minimum power, we can direct the weaker beam onto the center of the photodetector and measure the voltage on the diode using the lock-in amplifier. If the weaker beam reaches its minimum and strikes the center of the photodetector and we rotate the Wollaston polarizer in either direction, the voltage on this photodiode should always increase. The subsequent step is to make sure the stronger of the two output beams hits the center of the second photodetector and then put the quarter-wave plate into the gating beam. At this point, we measure the voltage difference between these 2 photodetectors, and by rotating the quarter-wave plate, we adjust the voltage difference between the two photodetectors to zero, indicating that two photodetectors are well balanced.

3.3 Measurements characterizing the THz-TDS system

3.3.1 NIR pulse and THz pulse measurements

In Fig. 3.5, we display the autocorrelation trace and the NIR spectrum of the pulse from the Yb:KGW amplifier. The autocorrelation trace corresponds to a pulse duration of 185 fs and the NIR spectrum centers around 1035 nm and with a bandwidth of 3.5 THz (FWHM).

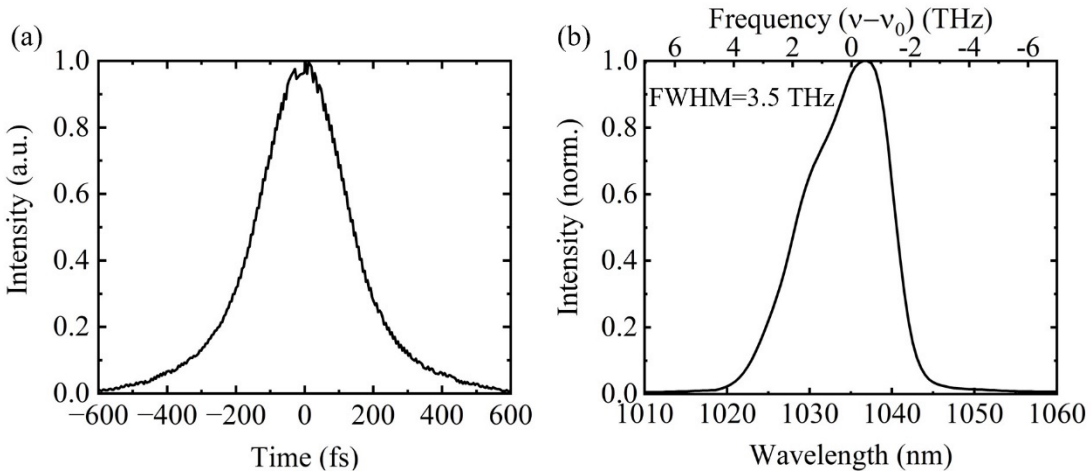

Fig. 3.5 (a) The autocorrelation trace of the femtosecond pulse from the Yb:KGW amplifier. (b) The NIR spectrum of the femtosecond pulse from the Yb:KGW amplifier, where ν_0 is the center frequency of the laser spectrum corresponding to a wavelength of 1035 nm.

Fig. 3.6 presents the time-domain signal and the calculated Fourier transform of the THz generated and detected with NIR pulses in Fig. 3.5, using a pair of identical 300 μm-thick GaP crystals for both THz generation and detection. The THz oscillation occurs in the picosecond range and the THz spectrum spans 0.1-5 THz with a 2.2 THz bandwidth (FWHM). In the next chapter, we will demonstrate that by using a hollow-core photonic-crystal fiber pulse shaper to spectrally broaden the NIR pulse, and compressing the output pulse with chirped mirrors, both the THz amplitude and spectral bandwidth can be enhanced.

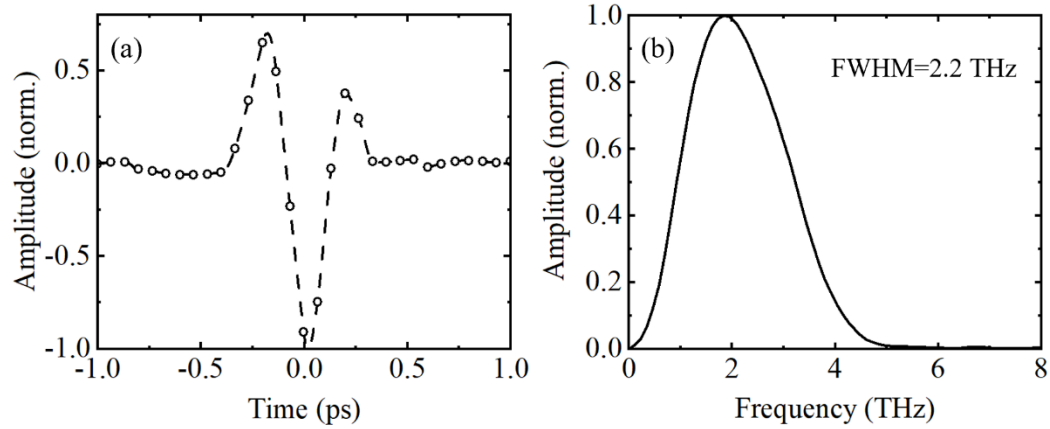

Fig. 3.6 (a) The THz time-domain signal measured with the NIR pulse in Fig. 3.5 using a 300 μm thick GaP generation crystal and detected by an identical GaP crystal. (b) Corresponding THz spectrum calculated by Fourier transform.

In the following subsections, we describe some experiments that utilized the NIR pulses from the hollow-core photonic-crystal fiber pulse shaper to operate the THz-TDS system. This pulse shaper increases the high-frequency limit of the THz spectrum to approximately 6.5 THz, assuming that the thicknesses of the generation and detection crystals do not limit the THz bandwidth due to the phase-matching condition.

3.3.2 Iris clipping THz beam

For this experiment, we place a fully open 2-inch iris in the collimated section of the THz beam. We gradually close the iris to gradually cut the THz beam and measure the time-domain signal of the THz beam. In this experiment, the generation crystal is a 1 mm-thick GaP and the gating crystal is a 100 μm-thick GaP crystal. The results are presented in Fig. 3.7. When the iris is fully open, the THz spectrum ranges from 0 to 4 THz with a spectral peak around 1.7 THz. The 4 THz full spectral width results from the phase-matching condition for the DFG process. As we progressively close the iris and block more of the THz beam's area, the measured THz amplitude decreases. Interestingly, as the open area of the iris reduces, the spectral peak of the THz shifts towards higher frequencies, except when the iris diameter is between 4 cm to 2.8 cm. This observation suggests that in the collimated section of the THz beam, the low-frequency components expand over a larger area while the high-frequency components concentrate more at the center of the THz beam. This is consistent with the fact that when the THz is generated with a focused NIR beam, the THz wavelengths are typically larger than that of the focal point size. Consequently, the generated THz behaves like a point source, and the longer the THz wavelength is (the lower the THz frequency is) the more spatial expansion of the THz beam is expected. The observed changes when the iris diameter decreases from 4 cm to 2.8 cm could be attributed to the iris not being perfectly centered within the THz beam.

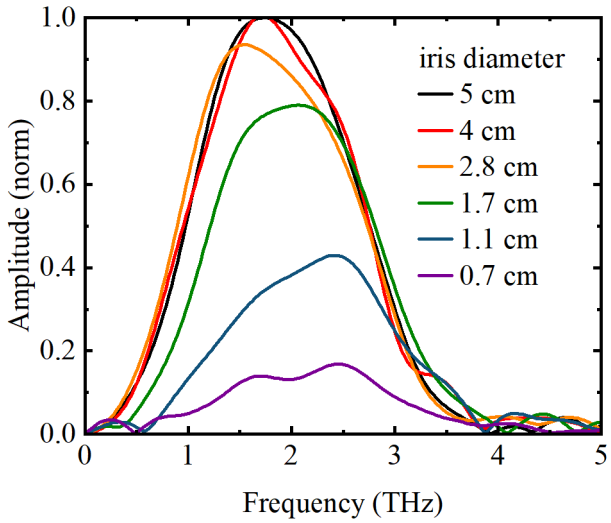

Fig. 3.7 THz spectra measured when an iris is open at specific sizes to cut the THz beam.

3.3.3 Saturation in the THz generation process

In this subsection, we increase the NIR pulse energy for THz generation to observe how the THz amplitude varies with the NIR generation pulse energy. This measurement is performed using a 2 mm-thick GaP crystal for THz generation and a 450 μm thick GaP for THz detection. The result is presented in Fig. 3.8. From Chapter 2, we understand that without saturation, the THz electric field is proportional to the power of the NIR generation beam. Here, when the laser power increases from 0.9 W to 1.8 W, the peak amplitude of the THz both in time and spectrum increases by a factor of 1.75, indicating the presence of saturation effects. As the laser power increases from 0.9 to 3.6 W, the THz peak amplitudes both temporally and spectrally increase by only a factor of 2.5. As the laser power further increases to 6 W, the peak THz amplitude both temporally and spectrally does not show a significant increase, indicating that the THz generation process is almost entirely saturated. To study the saturation effect of the THz generation, it is more appropriate to consider the fluence of the NIR beam on the generation crystal rather than the beam power. When the laser power is 0.9 W, the generation beam power reaching the generation crystal is approximately 0.7 W and the $1/e^2$ diameter of the beam is 27 μm on the surface of the generation crystal. The peak fluence of the NIR pulse on the generation crystal is calculated to be 22 mJ/cm^2. This is consistent

with the value (5.1 mJ/cm^2) where the saturation onset occurs, measured in Chapter 6. The saturation effect can be attributed to the multiphoton absorption [46] and heat effect [62]. Additionally, if we look into Fig. 3.8 (b), as the NIR generation beam power increases and the saturation of THz generation intensifies, the peak of the THz spectrum shifts towards low frequencies. This phenomenon has been observed in [63] but the cause of this shift remains under exploration.

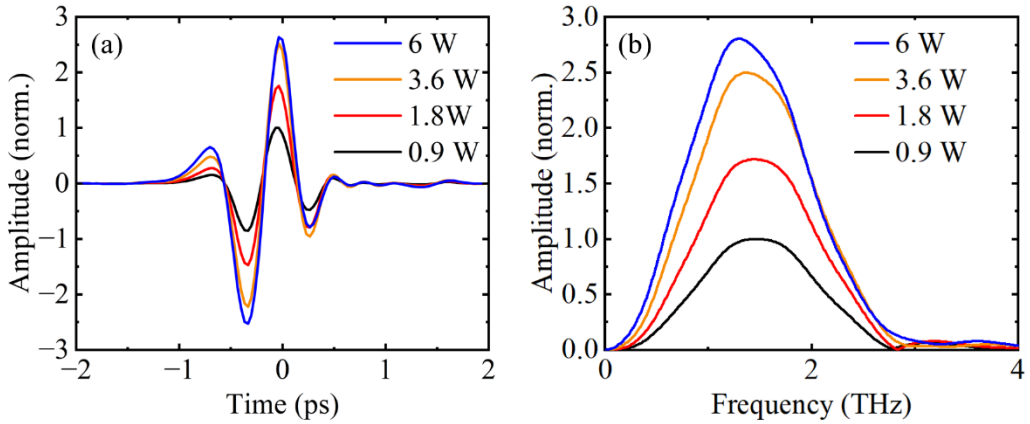

Fig. 3.8 (a) THz time-domain signal measured with different average power from the laser at 1.1 MHz. (b) Fourier transforms of the THz time-domain signals in (a). The generation crystal is a 2 mm-thick GaP and the detection crystal is a 450 µm-thick GaP. In both plots, the measured THz amplitudes are first normalized to the fluences on the balanced photodetectors and then normalized to the peak amplitude when the laser power is 0.9 W.

The peak THz field strength of the THz pulse is calculated to be 0.84 kV/cm, when the NIR laser average power is at 0.9 W. The calculation is according to [64]:

$$E_{THz} = \frac{A-B}{A+B}\frac{\lambda_{gat}K_{gat}}{2\pi r_{41}n_0^3 L t_{tot}}, \tag{3.3.1}$$

where A and B are the voltages on the balanced photodetectors, λ_{gat} is the central wavelength of the NIR gating beam (1035 nm), r_{41} = 1 pm/V is the electro-optical coefficient of GaP at 1035 nm [65], n_0 is the refractive index of the GaP at 1035 nm [66], L = 0.45 mm is the thickness of the GaP detection crystal, t_{tot} is the transmission coefficient taking into account the THz transmission through the GaP detection crystal at 1.3 THz (spectral peak) and the refractive index of the silicon

wafer at 1.3 THz [67]. In addition to the equation in [64], we introduce a damping factor K_{gat}=1.62 describing the "smooth effect" due to a non-infinitely short gating beam in the EOS process [68]. The method of calculating the THz peak field strength is also applied when estimating the field strength of THz generated with grating-assisted GaP crystals.

3.3.4 Measurement of typical THz crystals

The THz-TDS system's primary function is to measure the material's linear dispersion in the THz range. To validate the functionality of the system, my colleague Aidan Schiff-Kearn and I measured the refractive index and of GaP and ZnTe crystals using our first THz system. The results have been presented in his Master's thesis in 2018 [42]. Here, I present another set of measurements using the NIR pulse out of the hollow-core photonic-crystal fiber in the THz system, which can provide material dispersion information from 0.5 THz to 6 THz. I measured the 1 mm-thick and 2 mm-thick GaP crystals we have in our lab and compared them with the result in Parsons et al [69].

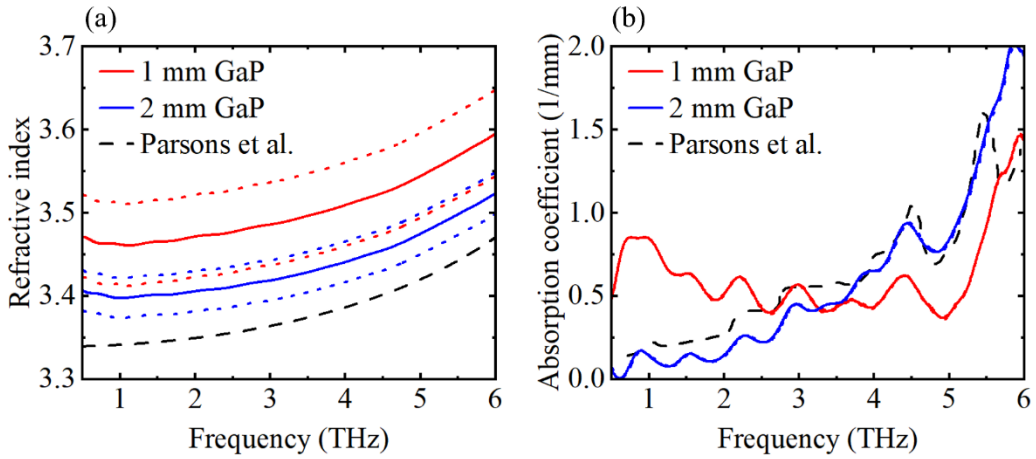

Fig. 3.9 Measured refractive index and the power absorption coefficient from 0.5 to 6 THz. The dot lines indicate uncertainties in these two calculated parameters due to the limited accuracy of the crystal thickness measurements. The accuracy of the caliper for thickness measurement is ±0.02 mm. These measured results are compared to those reference values in [69].

The refractive indices of the GaP crystals in our lab are consistent with that presented in [69], exhibiting minor deviations of approximately 0.13. This discrepancy, which equals to an

underestimate of the crystal thickness by 0.05 mm, may stem from the system errors arising from the use of different thickness measurement tools between us and Parsons et al. We determined the thickness of our crystal using a caliper with a precision of ±0.02 mm. Parsons et al. did not indicate the tool for the thickness measurements. Also, the refractive indices of the 1 mm-thick and 2 mm-thick GaP crystals differ by roughly 0.07. The overlapped uncertainty regions between these two measurements suggest a potential underestimation of the 1 mm-thick GaP's thickness by 0.02 mm and a corresponding overestimation for the 2 mm-thick GaP by the same margin. The uncertainty in the absorption coefficient influenced by thickness measurement errors is negligible. The 2 mm-thick GaP's absorption coefficient measurement aligns very well with the reference curve. The absorption coefficient of the 1 mm-thick GaP is higher than the reference value below 3 THz and lower than the reference value above 3 THz. For these measurements of GaP crystals, the measured absorption coefficients are more consistent with the reference curves in contrast to what is presented in Aidan Schiff-Kearn's thesis, which was much higher than the reference value. The differences in the absorption coefficient of GaP crystals of varying thickness arise from the fact that these GaP crystals were sourced from different manufacturers. Different manufacturing processes result in crystals with varying impurities, leading to different absorption coefficients. For example, the absorption coefficient of the 1 mm-thick GaP below 3 THz is higher than that in Ref [69], which could be due to slight doping in this crystal.

Chapter 4

Broadband and tunable time-resolved THz system using argon-filled hollow-core photonic-crystal fiber

4.1 Background and relevance

Previous chapters introduced THz time-domain spectroscopy based on nonlinear electro-optical crystals. Also, in the third chapter, we presented the dispersion information measurement performed using the THz time-domain system that operates with the Yb:KGW laser amplifier. This amplifier generates a NIR pulse with 180 fs pulse duration at 1035 nm wavelength and a spectral bandwidth of 3.5 THz (FWHM). In this chapter, the work focuses on improving the performance of such a THz-TDS system in terms of bandwidth and sensitivity [70].

THz generation within nonlinear crystals relies on difference-frequency mixing within an NIR pulse. Consequently, the spectral bandwidth of the NIR pulse directly affects the bandwidth of the THz pulses generated, assuming that the generation crystal does not restrict the generation bandwidth. In this study, the NIR beam from the Yb:KGW laser amplifier is launched into an argon-filled hollow-core photonic-crystal fiber (HC-PCF) that acts as a pulse shaper. The NIR beam broadens inside the HC-PCF through self-phase modulation (SPM), a third-order nonlinear effect. Another factor that impacts the THz generation bandwidth is the dispersion within the generation pulse. Put simply, different frequency components in the NIR pulse should reach the generation crystal simultaneously to interact efficiently. For this purpose, a pair of chirped mirrors compensates for the positive dispersion that occurs within the HC-PCF during the SPM. The reason that we chose gas as the nonlinear medium for the NIR broadening is that such substances resist

irreversible optical damage at high intensities, with the exception of molecular gases that undergo photochemical dissociation under such conditions. Additionally, the nonlinearity and dispersion properties of the gases can be fine-tuned by adjusting the pressure and composition of the gas mixture [71]. However, compared to solids, the gases exhibit significantly lower nonlinearity. As a consequence, they require longer nonlinear interaction lengths, necessitating the need for hollow waveguides. A potential solution to this problem is to use hollow-core fiber (HCF). Some research groups have employed the gas-filled HCF to spectrally broaden their NIR pulse and use such NIR pulse to generate broadband THz [72,73]. Typically, HCFs used in such works have an inner core diameter exceeding 200 μm and a length over 1 m, with the NIR pulse energies in the millijoule range. In our THz-TDS system, where the generation NIR beam is focused on the generation crystal, the generation NIR pulse energy is typically below 20 μJ. Using the same gas-filled HCF fiber for our NIR pulse would necessitate a much longer fiber, complicating the experimental setup and demanding more experimental space. Consequently, we select the Kagomé hollow-core photonic-crystal fiber to be the hollow-core waveguide. The thread of glass with a lattice of hollow microchannels creates a two-dimensional photonic-crystal structure extending longitudinally. These two-dimensional photonics crystal structures establish a complete or partial photonic band gap (PBG) that confines light within its central hollow core [71,74,75]. Fig. 4.1 presents a scanning electron microscope (SEM) scan of the cross-section of the Kagomé fiber in our experiments. This fiber has an inner core diameter of 34 μm. With this small core size, we broaden the NIR pulse of 0.9 μJ pulse energy from a spectral bandwidth of 3.5 THz to 8.7 THz using a 50 cm long fiber.

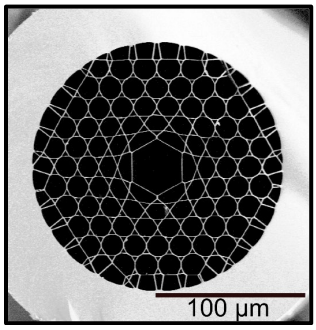

Fig. 4.1 A scanning electron microscope (SEM) scan of the cross-section of the Kagomé HC-PCF (provided by Dr. Jean-Michel Ménard).

Broadband and tunable time-resolved THz system using argon-filled hollow-core photonic crystal fiber

Wei Cui,[1,2] Aidan W. Schiff-Kearn,[1,2] Emily Zhang,[1,2] Nicolas Couture,[1,2] Francesco Tani,[2,3] David Novoa,[2,3] Philip St.J. Russell,[2,3] and Jean-Michel Ménard[1,2]

[1]*Department of Physics, University of Ottawa, Ottawa, Ontario K1N 6N5, Canada*
[2]*Max Planck Centre for Extreme and Quantum Photonics, Ottawa, Ontario K1N 6N5, Canada*
[3]*Max Planck Institute for the Science of Light, Erlangen 91058, Germany*

(Received 7 June 2018; accepted 11 August 2018; published online 7 September 2018)

We demonstrate broadband, frequency-tunable, phase-locked terahertz (THz) generation and detection based on difference frequency mixing of temporally and spectrally structured near-infrared (NIR) pulses. The pulses are prepared in a gas-filled hollow-core photonic crystal fiber (HC-PCF), whose linear and nonlinear optical properties can be adjusted by tuning the gas pressure. This permits optimization of both the spectral broadening of the pulses due to self-phase modulation (SPM) and the generated THz spectrum. The properties of the prepared pulses, measured at several different argon gas pressures, agree well with the results of numerical modeling. Using these pulses, we perform difference frequency generation in a standard time-resolved THz scheme. As the argon pressure is gradually increased from 0 to 10 bar, the NIR pulses spectrally broaden from 3.5 to 8.7 THz, while the measured THz bandwidth increases correspondingly from 2.3 to 4.5 THz. At 10 bar, the THz spectrum extends to 6 THz, limited only by the spectral bandwidth of our time-resolved detection scheme. Interestingly, SPM in the HC-PCF produces asymmetric spectral broadening that may be used to enhance the generation of selected THz frequencies. This scheme, based on a HC-PCF pulse shaper, holds great promise for broadband time-domain spectroscopy in the THz, enabling the use of compact and stable ultrafast laser sources with relatively narrow linewidths (<4 THz). https://doi.org/10.1063/1.5043270

I. INTRODUCTION

Terahertz time-domain spectroscopy (THz-TDS) is a broadband optical characterization technique increasingly applied in many fields for non-invasive imaging and identification of molecules.[1–8] In condensed matter research, this technique is also used to trace ultrafast dynamics of low-energy excitations when combined with a pump pulse to excite non-equilibrium states inside materials such as semiconductors, strongly correlated materials, superconductors, and topological insulators.[8–18] Common THz-TDS systems, including most of the ones commercially available, are now able to resolve with great sensitivity the spectral range covering 0.5–4 THz. One of the next frontiers in THz photonics is therefore the development of efficient schemes for expanding this spectral window beyond 4 THz, so as to allow access to both a wider range of molecular resonances for sensing applications and new microscopic interactions in condensed matter. Some experimental schemes have already been reported for achieving ultra-broadband THz spectroscopy. They are based on nonlinear optical generation and detection in laser-induced gas plasmas (THz wave air photonics),[19–22] GaP or several-micron-thick ZnTe crystals[23–25] and birefringent $LiGaS_2$ (LGS),[26,27] GaSe,[27–31] and organic crystals such as DAST.[32,33] Although these configurations rely on different types of nonlinear media, they all share an essential common component: an ultrafast near-infrared (NIR) laser capable of delivering broadband femtosecond pulses. Such an optical source is crucial for accessing the high

THz frequency range since THz radiation is generated by nonlinear difference frequency mixing of NIR pulses, which means that the highest generated THz frequencies are determined by the spectral bandwidth of the NIR pulses. Furthermore, efficient time-resolved THz detection requires ultrashort NIR pulses with a duration shorter than the oscillation cycle of the highest THz frequency components to achieve broadband detection. These two conditions impose stringent requirements on the NIR ultrafast source. As a result, expensive and bulky optical systems are often necessary for broadband THz-TDS. We propose an alternative setup for generating broadband THz radiation, one that can be used with a compact and stable MHz laser system delivering pulses of sub-microjoule energy and a few hundreds of femtoseconds in duration. We use a commercial Yb:KGW ultrafast amplifier in combination with a gas-filled kagomé-type hollow-core photonic crystal fiber (kagomé-PCF) to achieve efficient broadband THz generation and detection.[34] Gas-filled hollow-core photonic crystal fiber (HC-PCF) is one of the most efficient and versatile nonlinear platforms for spectral and temporal structuring of NIR pulses.[35–39] It provides weak anomalous dispersion that can be counter-balanced by the normal dispersion of the gas filling the fiber, allowing propagation of ultrashort pulses with minimal temporal distortion. In contrast to solid-core fibers or highly nonlinear materials, the linear and nonlinear properties of the system can be adjusted simply by changing the species and the pressure of the gas filling the HC-PCF. Here, we take advantage of this unique feature to broaden the spectrum covered by the THz-TDS system out to ~6 THz, limited only by the choice of the nonlinear crystal for time-resolved detection. More importantly, the general concept of using a HC-PCF pulse shaper in combination with a relatively narrow spectral linewidth (<4 THz) laser could be extended to other schemes based on different generation and detection crystals such as LGS or GaSe, which would extend further the spectral coverage of THz-TDS.

II. EXPERIMENT AND NUMERICAL SIMULATIONS

The experimental configuration is sketched in Fig. 1. The optical source is a commercial Yb:KGW amplifier delivering 185 fs pulses at a central wavelength of 1035 nm, an average power of 1 W, and a repetition rate of 1.1 MHz. The emitted pulses are launched into an Ar-filled HC-PCF with 75% coupling efficiency. The fiber, a 55 cm-long kagomé-PCF with a 34 μm-diameter core, is entirely placed inside a gas cell within which the Ar pressure can easily be adjusted. This scheme allows us to change the properties of the optical medium and tune the effects of self-phase modulation (SPM) broadening and restructuring the NIR pulse spectrum. A pair of identical chirped mirrors (CMs), providing a total dispersion of -2500 fs^2, is placed after the HC-PCF to compensate for the positive chirp resulting from SPM and to ensure that the pulses are nearly Fourier-transform-limited. A standard THz-TDS configuration is then used to generate and detect the THz radiation.[35] Briefly, the NIR beam is split into two paths. In the first path, phase-locked THz radiation is generated by difference frequency mixing inside a 220 μm thick 110-oriented GaP crystal. The second path is used as an optical gate for time-resolved electro-optical detection. An identical GaP nonlinear crystal is used for detection.

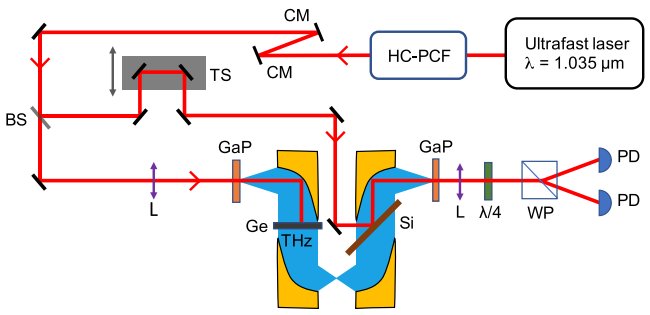

FIG. 1. Schematic of the experimental setup. NIR pulses are launched into a HC-PCF filled with Ar gas at an adjustable pressure. A standard THz-TDS scheme is then used to generate and detect THz radiation.[40] CM: chirped mirror; BS: beam splitter; TS: translational stage; L: lens, GaP: 110-oriented 220 μm-thick gallium phosphide crystal; Ge: germanium wafer; Si: silicon wafer; $\lambda/4$: quarter-wave plate; WP: Wollaston prism; PD: photodetector.

A. Near-infrared pulse propagation in the HC-PCF pulse shaper

The NIR pulse properties are measured after the CMs using a USB spectrometer and a home-made autocorrelator based on second harmonic generation in a 150-μm-thick beta-barium borate (BBO) crystal. As the Ar pressure (P_{Ar}) is increased from 0 to 10 bar, the NIR spectrum gradually broadens from a full-width at half-maximum (FWHM) of 3.5 to 8.7 THz [Fig. 2(a)]. The spectral broadening manifests itself mainly in two sidelobes separated by $\Delta\nu_{SL}$ = 3.1 THz at 7.5 bar and 4.7 THz at 10 bar. The corresponding autocorrelation traces are shown in Fig. 2(b) from which, assuming that the structured NIR pulses have a sech^2 temporal shape, the original pulse duration can be recovered. The pulse duration is observed to decrease gradually, from 185 fs to 65 fs (FWHM), as P_{Ar} is increased. The fact that the spectral bandwidth increases by a factor of 2.5 while the temporal duration decreases by 2.8 indicates that the pulses are close to Fourier-transform-limited at all the pressures used in the experiment.

Figure 2(c) shows the simulated spectra at the fiber output at different Ar pressures for a 185 fs (FWHM) Gaussian pulse with 0.85 μJ energy. The simulations are based on a unidirectional field equation[41] and approximate the fiber dispersion by that of a narrow-bore capillary.[42] Over the pressure range used, the NIR pulses lie in the anomalous dispersion range within the fiber. For these spectral bandwidths, however, the fiber dispersion is insufficient to compensate for the positive chirp resulting from SPM, which therefore requires further compensation using negatively chirped mirrors after the fiber. Figure 2(d) shows the simulated temporal profiles at the fiber output after introducing 2000 fs^2 negative chirp (as in the experiment). As the argon pressure increases from 0 to 10 bar the temporal FWHM decreases from 189 fs to 68 fs, which is in excellent agreement with the experiments. The simulations show no contribution related to pulse-induced gas ionization over the range of parameters used in the experiments.

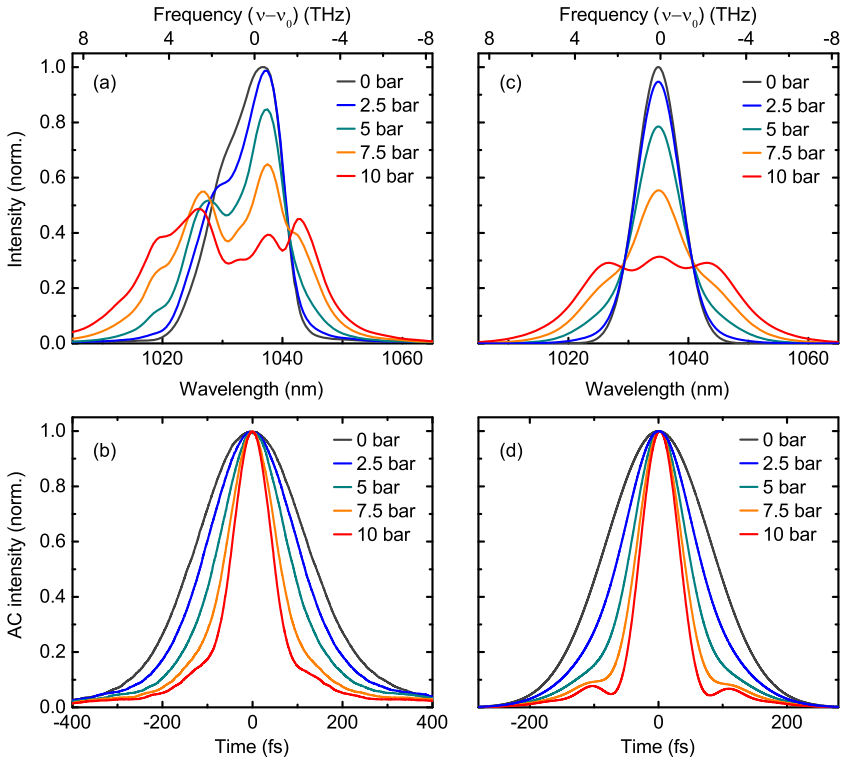

FIG. 2. (a) Spectra of the NIR pulses measured after the HC-PCF and the CM pair for different Ar pressures. (b) Corresponding autocorrelation traces. The FWHM durations measured at P_{Ar} = 0, 2.5, 5, 7.5, and 10 bar are 185, 150, 115, 85, and 65 fs, respectively. [(c) and (d)] For the same conditions, the numerical simulations[41] of the pulse spectra and duration show good agreement with the experiments.

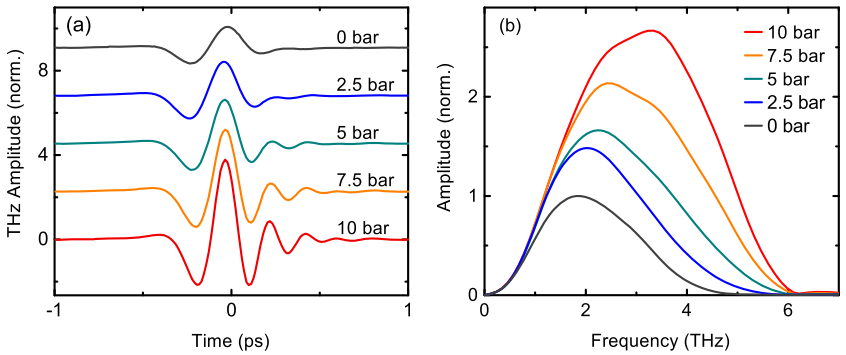

FIG. 3. (a) Phase-locked THz transients measured with NIR pulses prepared in the HC-PCF at different Ar pressures, as shown in Fig. 2. (b) Corresponding THz spectral amplitude calculated by Fourier transforming. In (a) and (b), the maximum amplitude of the measurement at 0 bar is normalized to 1.

B. Phase-locked THz generation

The NIR pulses measured in Figs. 2(a) and 2(b) are injected in the THz-TDS scheme for phase-locked THz generation and detection by electro-optic sampling. Figure 3(a) shows the resulting time-resolved THz field. Simply by adjusting the gas pressure, the peak THz amplitude can be increased by a factor of ~4. This increase is caused by temporal compression of the NIR pulses, leading to higher peak powers and, consequently, to more efficient nonlinear frequency down-conversion. The corresponding THz spectral amplitudes are shown in Fig. 3(b). Distinctly different behavior is observed above and below a frequency of 1 THz: the amplitude of higher spectral components is enhanced as P_{Ar} is increased, while no significant change is observed in the sub-1-THz portion of the spectrum. As a result, the THz bandwidth can be increased from 2.3 THz to 4.5 THz (FWHM). The sudden drop in the spectral amplitude at 6.2 THz is related to the restricted phase-matching conditions in the two 220 μm-thick GaP crystals used for THz generation and detection, which ultimately limit the attainable THz bandwidth. The results agree well with the calculated phase-matching cut-off frequency at 6.6 THz.[43]

Interestingly, SPM in kagomé-PCF produces an unevenly distributed spectrum in the NIR pulses, which will have a direct impact on the generated THz spectrum. At $P_{Ar} > 5$ bar the NIR spectrum departs from a Gaussian-like distribution, displaying two side-lobes separated by $\Delta\nu_{SL}$. Since the THz radiation is produced by difference frequency mixing between NIR pulse components, these side-lobes are expected to enhance THz generation around $\Delta\nu_{SL}$, resulting in distinct peaks in the spectra. However, in the experiment, the electro-optic detection process prevents us from clearly distinguishing this peak since the detection efficiency is not homogeneous over the whole spectral bandwidth.[44,45] Due to the time-resolved configuration, the amplitude of the lowest and highest THz frequencies is under-estimated: Low frequencies have a larger spot size on the detection crystal and do not overlap as well with the focused gating pulse, while high THz frequencies suffer from a phase mismatch with the gating pulse inside the detection crystal. The peak in the measured THz spectra is therefore mostly determined by the time-resolved detection response rather than the spectral shape of the generated THz radiation.

III. CONCLUSION

A pressure-tunable pulse shaper based on gas-filled kagomé-PCF can be used to prepare NIR pulses for efficient broadband THz-TDS. As the Ar pressure is increased in the PCF, spectral broadening and temporal compression of the NIR pulses allow the bandwidth of the measured THz spectrum to be broadened by a factor of 2, the highest frequency component at ~6 THz being limited only by phase-matching conditions in the experiment. This scheme could also be used for accessing higher THz frequencies if the argon pressure is increased beyond 10 bar and different nonlinear generation and detection crystals are used, such as GaSe, LGS, DAST, or $AgGaS_2$. In brief, a single fiber-based module, combined with an ultrafast source with relatively narrow linewidth (<4 THz), can be used

for broadband THz-TDS, paving the way to the design of more compact and cost-effective THz-TDS setups capable of reaching high THz frequencies without the need for complex optical sources based on ultrashort Ti-sapphire amplifiers, synchronized fiber lasers, or optical parametric chirped-pulse amplifiers. Since HC-PCFs are robust and able to guide extremely high peak powers, they may also enable the use of high power and high repetition rate lasers for THz-TDS.[46,47]

ACKNOWLEDGMENTS

J.-M. Ménard acknowledges support from the National Sciences and Engineering Research Council (NSERC), Canada foundation for innovation (CFI), and Ministry of Research and Innovation's (MRI) Ontario Research Fund.

[1] P. Daukantas, "Cultural artifacts in terahertz light," Opt. Photonics News **29**, 28–35 (2018).
[2] C. Seco-Martorell, V. López-Domínguez, G. Arauz-Garofalo, A. Redo-Sanchez, J. Palacios, and J. Tejada, "Goya's artwork imaging with terahertz waves," Opt. Express **21**, 17800–17805 (2013).
[3] A. Redo-Sanchez, B. Heshmat, A. Aghasi, S. Naqvi, M. Zhang, J. Romberg, and R. Raskar, "Terahertz time-gated spectral imaging for content extraction through layered structures," Nat. Commun. **7**, 12665 (2016).
[4] J. F. Federici, B. Schulkin, F. Huang, D. Gary, R. Barat, F. Oliveira, and D. Zimdars, "THz imaging and sensing for security applications—Explosives, weapons and drugs," Semicond. Sci. Technol. **20**, S266 (2005).
[5] B. Fischer, M. Hoffmann, H. Helm, G. Modjesch, and P. U. Jepsen, "Chemical recognition in terahertz time-domain spectroscopy and imaging," Semicond. Sci. Technol. **20**, S246 (2005).
[6] E. P. Parrott and J. A. Zeitler, "Terahertz time-domain and low-frequency Raman spectroscopy of organic materials," Appl. Spectrosc. **69**, 1–25 (2015).
[7] P. D. Cunningham, N. N. Valdes, F. A. Vallejo, L. M. Hayden, B. Polishak, X.-H. Zhou, J. Luo, A. K.-Y. Jen, J. C. Williams, and R. J. Twieg, "Broadband terahertz characterization of the refractive index and absorption of some important polymeric and organic electro-optic materials," J. Appl. Phys. **109**, 043505 (2011).
[8] P. U. Jepsen, D. G. Cooke, and M. Koch, "Terahertz spectroscopy and imaging—Modern techniques and applications," Laser Photonics Rev. **5**, 124–166 (2011).
[9] R. A. Kaindl, M. A. Carnahan, D. Hägele, R. Lövenich, and D. S. Chemla, "Ultrafast terahertz probes of transient conducting and insulating phases in an electron–hole gas," Nature **423**, 734–738 (2003).
[10] R. Huber, F. Tauser, A. Brodschelm, M. Bichler, G. Abstreiter, and A. Leitenstorfer, "How many-particle interactions develop after ultrafast excitation of an electron–hole plasma," Nature **414**, 286–289 (2001).
[11] J.-M. Ménard, C. Poellmann, M. Porer, U. Leierseder, E. Galopin, A. Lemaître, A. Amo, J. Bloch, and R. Huber, "Revealing the dark side of a bright exciton–polariton condensate," Nat. Commun. **5**, 4648 (2014).
[12] M. C. Beard, G. M. Turner, and C. A. Schmuttenmaer, "Transient photoconductivity in GaAs as measured by time-resolved terahertz spectroscopy," Phys. Rev. B **62**, 15764–15777 (2000).
[13] R. Ulbricht, E. Hendry, J. Shan, T. Heinz, and M. Bonn, "Carrier dynamics in semiconductors studied with time-resolved terahertz spectroscopy," Rev. Mod. Phys. **83**, 543–586 (2011).
[14] M. Porer, U. Leierseder, J.-M. Ménard, H. Dachraoui, L. Mouchliadis, I. E. Perakis, U. Heinzmann, J. Demsar, K. Rossnagel, and R. Huber, "Non-thermal separation of electronic and structural orders in a persisting charge density wave," Nat. Mater. **13**, 857–861 (2014).
[15] C. Poellmann, P. Steinleitner, U. Leierseder, P. Nagler, G. Plechinger, M. Porer, R. Bratschitsch, C. Schüller, T. Korn, and R. Huber, "Resonant internal quantum transitions and femtosecond radiative decay of excitons in monolayer WSe_2," Nat. Mater. **14**, 889–893 (2015).
[16] C. J. Docherty, P. Parkinson, H. J. Joyce, M.-H. Chiu, C.-H. Chen, M.-Y. Lee, L.-J. Li, L. M. Herz, and M. B. Johnston, "Ultrafast transient terahertz conductivity of monolayer MoS_2 and WSe_2 grown by chemical vapor deposition," ACS Nano **8**, 11147–11153 (2014).
[17] R. Valdés Aguilar, J. Qi, M. Brahlek, N. Bansal, A. Azad, J. Bowlan, S. Oh, A. J. Taylor, R. P. Prasankumar, and D. A. Yarotski, "Time-resolved terahertz dynamics in thin films of the topological insulator Bi_2Se_3," Appl. Phys. Lett. **106**, 011901 (2015).
[18] L. Junpeng and L. Hongwei, "A critical review on the carrier dynamics in 2D layered materials investigated using THz spectroscopy," Opt. Commun. **406**, 24–35 (2018).
[19] D. J. Cook and R. M. Hochstrasser, "Intense terahertz pulses by four-wave rectification in air," Opt. Lett. **25**, 1210–1212 (2000).
[20] X. Xie, J. Dai, and X.-C. Zhang, "Coherent control of THz wave generation in ambient air," Phys. Rev. Lett. **96**, 075005 (2006).
[21] J. Dai, X. Xie, and X.-C. Zhang, "Detection of broadband terahertz waves with a laser-induced plasma in gases," Phys. Rev. Lett. **97**, 103903 (2006).
[22] E. Matsubara, M. Nagai, and M. Ashida, "Ultrabroadband coherent electric field from far infrared to 200 THz using air plasma induced by 10 fs pulses," Appl. Phys. Lett. **101**, 011105 (2012).
[23] A. Leitenstorfer, S. Hunsche, J. Shah, M. C. Nuss, and W. H. Knox, "Detectors and sources for ultrabroadband electro-optic sampling: Experiment and theory," Appl. Phys. Lett. **74**, 1516 (1999).
[24] K. Aoki, J. Savolainen, and M. Havenith, "Broadband terahertz pulse generation by optical rectification in GaP crystals," Appl. Phys. Lett. **110**, 201103 (2017).
[25] R. Huber, B. Schmid, R. Kaindl, and D. Chemla, "Femtosecond THz studies of intra-excitonic transitions," Phys. Status Solidi B **245**, 1041–1048 (2008).

[26] I. Pupeza, D. Sánchez, J. Zhang, N. Lilienfein, M. Seidel, N. Karpowicz, T. Paasch-Colberg, I. Znakovskaya, M. Pescher, W. Schweinberger, V. Pervak, E. Fill, O. Pronin, Z. Wei, F. Krausz, A. Apolonski, and J. Biegert, "High-power sub-two-cycle mid-infrared pulses at 100 MHz repetition rate," Nat. Photonics **9**, 721 (2015).
[27] M. Knorr, J. Raab, M. Tauer, P. Merkl, D. Peller, E. Wittmann, E. Riedle, C. Lange, and R. Huber, "Phase-locked multi-terahertz electric fields exceeding 13 MV/cm at a 190 kHz repetition rate," Opt. Lett. **42**, 4367–4370 (2017).
[28] C. Kübler, R. Huber, S. Tübel, and A. Leitenstorfer, "Ultrabroadband detection of multi-terahertz field transients with GaSe electro-optic sensors: Approaching the near infrared," Appl. Phys. Lett. **85**, 3360 (2004).
[29] K. Liu, J. Xu, and X.-C. Zhang, "GaSe crystals for broadband terahertz wave detection," Appl. Phys. Lett. **85**, 863 (2004).
[30] A. Sell, A. Leitenstorfer, and R. Huber, "Phase-locked generation and field-resolved detection of widely tunable terahertz pulses with amplitudes exceeding 100 MV/cm," Opt. Lett. **33**, 2767–2769 (2008).
[31] J. Zhang, K. F. Mak, N. Nagl, M. Seidel, D. Bauer, D. Sutter, V. Pervak, F. Krausz, and O. Pronin, "Multi-mW, few-cycle mid-infrared continuum spanning from 500 to 2250 cm^{-1}," Light: Sci. Appl. **7**, 17180 (2018).
[32] H. Adachi, T. Taniuchi, M. Yoshimura, S. Brahadeeswaran, T. Higo, M. Takagi, Y. Mori, T. Sasaki, and H. Nakanishi, "High-quality organic 4-dimethylamino-N-methyl-4-stilbazolium tosylate (DAST) crystals for THz wave generation," Jpn. J. Appl. Phys., Part 2 **43**, L1121 (2004).
[33] M. Martin, J. Mangeney, P. Crozat, and P. Mounaix, "Optical phase detection in a 4-N,N-dimethylamino-4′-N′-methyl-stilbazolium tosylate crystal for terahertz time domain spectroscopy system at 1.55 μm wavelength," Appl. Phys. Lett. **97**, 111112 (2010).
[34] F. Benabid, J. C. Knight, G. Antonopoulos, and P. St. J. Russell, "Stimulated Raman scattering in hydrogen-filled hollow-core photonic crystal fiber," Science **298**, 399–402 (2002).
[35] K. F. Mak, M. Seidel, O. Pronin, M. H. Frosz, A. Abdolvand, V. Pervak, A. Apolonski, F. Krausz, J. C. Travers, and P. St. J. Russell, "Compressing μJ-level pulses from 250 fs to sub-10 fs at 38-MHz repetition rate using two gas-filled hollow-core photonic crystal fiber stages," Opt. Lett. **40**, 1238–1241 (2015).
[36] P. St. J. Russell, P. Hölzer, W. Chang, A. Abdolvand, and J. C. Travers, "Hollow-core photonic crystal fibres for gas-based nonlinear optics," Nat. Photonics **8**, 278–286 (2014).
[37] M. Saleh and F. Biancalana, "Tunable frequency-up/down conversion in gas-filled hollow-core photonic crystal fibers," Opt. Lett. **40**, 4218 (2015).
[38] J. Travers, W. Chang, J. Nold, N. Joly, and P. St. J. Russell, "Ultrafast nonlinear optics in gas-filled hollow-core photonic crystal fibers," J. Opt. Soc. Am. B **28**, A11 (2011).
[39] O. Heckl, C. Saraceno, C. Baer, T. Südmeyer, Y. Wang, Y. Cheng, F. Benabid, and U. Keller, "Temporal pulse compression in a xenon-filled Kagome-type hollow-core photonic crystal fiber at high average power," Opt. Express **19**, 19142 (2011).
[40] X.-C. Zhang and J. Xu, *Introduction to THz Wave Photonics* (Springer, 2010).
[41] F. Tani, J. C. Travers, and P. St.J. Russell, "Multimode ultrafast nonlinear optics in optical waveguides: Numerical modeling and experiments in kagomé photonic-crystal fiber," J. Opt. Soc. Am. B **31**, 311–320 (2014).
[42] E. A. J. Marcatili and R. A. Schmeltzer, "Hollow metallic and dielectric waveguides for long distance optical transmission and lasers," Bell Syst. Tech. J. **43**, 1783–1809 (1964).
[43] D. R. Parsons and P. D. Coleman, "Far infrared optical constants of gallium phosphide," Appl. Opt. **10**, 1683–1685 (1971).
[44] G. Gallot and D. Grischkowsky, "Electro-optic detection of terahertz radiation," J. Opt. Soc. Am. B **16**, 1204–1212 (1999).
[45] A. Tomasino, A. Parisi, S. Stivala, P. Livreri, A. C. Cino, A. C. Busacca, M. Peccianti, and R. Morandotti, "Wideband THz time domain spectroscopy based on optical rectification and electro-optic sampling," Sci. Rep. **3**, 3116 (2013).
[46] F. Emaury, C. J. Saraceno, B. Debord, D. Ghosh, A. Diebold, F. Gerome, T. Sudmeyer, F. Benabid, and U. Keller, "Efficient spectral broadening in the 100-W average power regime using gas-filled kagomé HC-PCF and pulse compression," Opt. Lett. **39**, 6843–6846 (2014).
[47] U. Elu, M. Baudisch, H. Pires, F. Tani, M. H. Frosz, F. Köttig, Al. Ermolov, P. St.J. Russell, and J. Biegert, "High average power and single-cycle pulses from a mid-IR optical parametric chirped pulse amplifier," Optica **4**, 1024–1029 (2017).

4.2 Additional comments

The THz spectral range presented in this work is not the upper limit of the THz generation and detection from our laser system when combined with the HC-PCF. By launching more NIR pulse energy into the HC-PCF or elevating the gas pressure in the HC-PCF, we can further enhance the SPM inside the HC-PCF, leading to a broader NIR spectrum. The pressure in the gas cell for this APL Photonics paper was set at 10 bar. Subsequently, we attempted to increase the gas pressure to 15 bar to further enhance the NIR bandwidth and replaced the generation and detection crystals with ZnTe. Unlike GaP, which exhibits phonon absorption around 11 THz [63], ZnTe possesses a phonon resonance only around 5 THz, thereby allowing higher THz frequencies to be detected, albeit with limited sensitivity due to imperfect phase-matching conditions. Utilizing a 200 μm thick ZnTe pair for both THz generation and detection, we not only observed a primary THz signal spanning from 0.1 to 4 THz but also detected a THz spectrum ranging from 7 to14 THz. This extra THz bandwidth comes from the fact that with a higher pressure in the HC-PCF Additionally, by further increasing the NIR pulse energy and gas pressure in the HC-PCF, and using a GaSe as the generation and detection crystal, our group has achieved THz generation and detection above 20 THz [76].

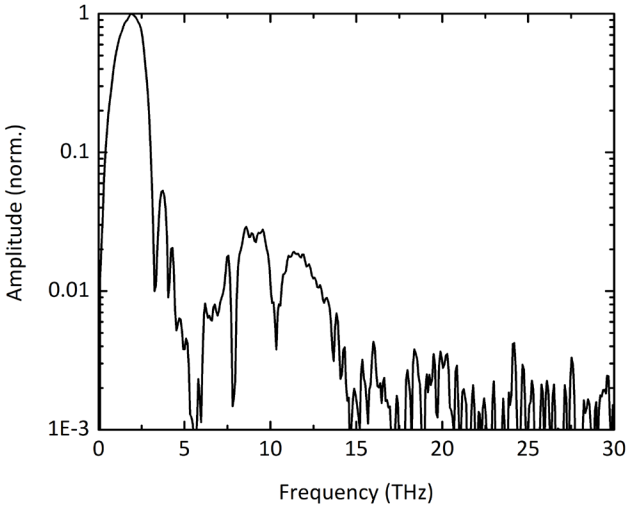

Fig. 4.2 THz spectrum measured with the NIR pulse out of argon-filled HC-PCF at 15 bar for THz generation and detection. The generation and detection crystals are 200 μm thick ZnTe.

In our system, the highest coupling efficiency achieved using a single lens to focus the NIR beam into the HC-PCF was 81%. The input pulse energy was 0.9 μJ and output pulse energy was approximately 0.7 μJ. Our primary object is to produce high-field THz radiation with the dominant spectral components exceeding 2 THz. The generation of high-field THz typically involves in NIR generation pulse energy in the millijoule range. In our lab, the highest NIR pulse energy we have launched into this HC-PCF is 5.5 μJ. In order to guide the mJ NIR pulses using the HC-PCF, we could further refine the focusing optics for fiber coupling. According to our collaborators, it is possible to achieve a 98% coupling efficiency with this HC-PCF fiber with optimized coupling optics. Under such conditions, the majority of the pulse energy is guided within the hollow core of the fiber, preventing damage to glass structure in the HC-PCF.

4.3 Appendix

4.3.1 Installation of the HC-PCF in the gas cell

The Kagomé HC-PCF fiber is positioned inside an Argon-filled gas cell. The gas cell was designed by Dr. Philip Russel's group at the Max Planck Institute for the Science of Light and manufactured

at the University of Ottawa's machine shop. As depicted in Fig. 4.3 (a), the gas cell comprises 2 distinct gas chambers interconnected with a metal tube. Both sides of the gas cell, equipped with optical windows, are supported by 2 MAX362D fiber launch systems from Thorlabs. Raised ridges in the middle of the bottom of the 2 gas chambers aligned with the grooves on top of the L-shape fixed angle brackets (AMA009 from Thorlabs). It is important to note that these L-shape Fix angle brackets remain stationary and do not move with the MAX362D stages. The opposite side of the gas chamber fits into the grooves on the Thorlabs AMA029A platform. All the supporting structures maintain the same height and their design ensures that the grooves align with a series of holes on the optical table. Consequently, the fiber positioned centrally inside the gas cell aligns with these holes.

Upon initially receiving the gas cell components, it is essential to clean them with acetone to eliminate any residual oil from the fabrication process. Failing to do so can lead to oil will start vaporization when purging the enclosure, contaminating the optical windows on both sides of the gas cell and the HC-PCF tips with oil vapors.

To accurately launch the beam into the HC-PCF, it is crucial to ensure the beam is perfectly horizontal and at the same height as the fiber's position. Our approach involves placing 2 irises on the 2 L-shape Fixed angle bracket and aligning the collimated beam through the center of the 2 irises. Subsequently, we position the gas cell and insert the fiber.

(a) 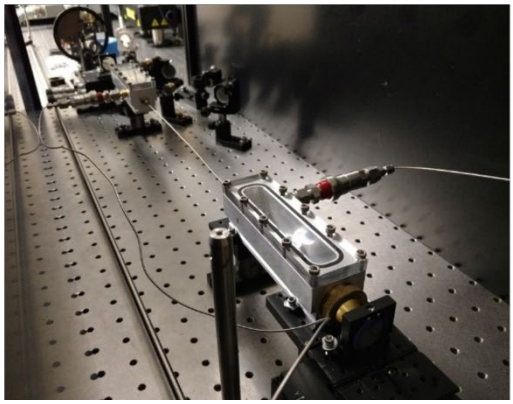 (b) 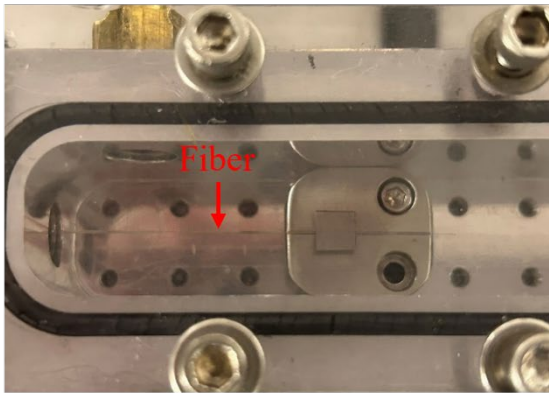

Fig. 4.3 The gas cell containing the Kagomé HC-PCF. (b) An overshot picture of one chamber of the gas cell showing how the HC-PCF is placed inside the gas cell.

As depicted in Fig. 4.3 (b), the central portion of the fiber resides within the metal tube connecting the 2 chambers. Both tips of the fiber are supported by 2 base metal blocks, each featuring a central groove. This design makes sure the fiber is precisely aligned with the center line of the gas cell which corresponds to a series of holes on the optical table. These 2 base metal blocks are designed to hold the fiber at the same elevation as the metal tube. Another 2 small blocks with the same groove to is placed over the fiber tips to hold it in place. When installing the fiber into the gas cell, the procedures begin by cleaving one end of the fiber and positioning it within one of the gas chambers. Subsequently, the opposite fiber tip is gently guided through the tube connecting the 2 chambers. It is essential to avoid cleaving this fiber tip beforehand, as any friction or impact during the guiding process could damage the freshly cleaved tip. Once the other fiber tip is in place within the other gas chamber, we cleave it and leave it in place. This step should be a collaborative effort involving 2 people: one focusing on cleaving the fiber and the other using tweezers to restrict the movement of the fiber tip in the other chamber. This ensures the cleaved fiber does not come into contact with any hard surface, which could compromise the integrity of the cleaved end.

The subsequent step is to couple the light into the HC-PCF and collimate the output beam. Initially. a ruler can be employed to gauge the distance between the fiber tip and the middle point of the MAX362D stage along the direction of the fiber. Based on this measurement, a lens with a

corresponding focal length is positioned. If one tip is too close or too far from the middle of the MAX362D stage along the direction of the fiber, a soft-tipped tweezer can be used to adjust the position of the fiber within the gas cell. Again, this procedure benefits from a second individual to who ensures the proper positioning of the fiber tip in the other chamber. Following this is to place the lens and put a power meter at the output of the fiber. We experimented with lenses of different focal lengths to optimize the coupling. For the Kagomé fiber, a lens with 7 cm focal length proved the most effective. Given that the laser is at 1035 nm, an IR-viewer aids in this process. We use the 3D stage to adjust the lens in the plane perpendicular to the fiber's direction, ensuring the beam roughly targets the fiber tip. When light is coupled to the cladding of the fiber, visible light emanates from the fiber tip due to the nonlinear effects such as self-phase modulation happening in the glass cladding. After the beam is coupled to the core of the fiber, the visible light vanishes. Fine-tuning the 3D MAX362D stage to achieve maximum output power. We have achieved a peak coupling efficiency of 81% with this Kagomé HC-PCF. After coupling, we collimate the beam out of the fiber by adjusting the lens on the 3D MAX362D stage. It is essential to guide the beam far away from the output and ensure the beam is of the same size along the beam path, maintaining a distortion-free beam profile.

The final procedures involve purging the gas cell with the argon gas. We first seal the gas cell and subsequently vacuum the gas cell with a vacuum pump. If there is no leakage in the gas cell, the vacuum pump should work briefly and turn into a low output mode, characterized by minimal operational noise. Then the gas cell is typically maintained under vacuum for at least 12 hours before introducing argon.

Fig. 4.4 The picture of the gas cell pressure control panel. There are 3 valves on the panel to increase the pressure in the gas cell in stages. The gas cell pressure sensor measures the gas pressure inside the tube connecting to the gas cell.

To make sure the minimal fiber displacement during the process of increasing the pressure, both chambers are interconnected to the gas pressure panel. This configuration ensures simultaneous pressure increases in both chambers. Otherwise, the fiber will be blown to the chamber with no gas input when the gas pressure increases. Fig. 4.4 depicts the gas pressure controlling panel in our lab. The following steps are designed to gradually elevate the gas pressure in the gas cell. We

1. open and close the valve on the gas cylinder to fill the argon gas into the tube preceding valve 1.
2. swiftly open and close valve 1, directing the argon gas into the tube segment between valves 1 and 2.
3. rapidly open and close valve 2, directing the argon gas into the tube segment between valves 2 and 3.
4. open and close valve 3 quickly and monitor the pressure in the gas cell. We reiterate this action multiple times until we achieve a stable gas pressure in the gas cell.
5. repeat steps 3, 4 until valve 2 does not affect the pressure in the gas cell.
6. keep repeating steps 2-6 until valve 1 does not affect the pressure in the gas cell.
7. repeat steps 1-7 until the pressure in the gas cell reaches the set value.

It is imperative to adhere to the steps above, especially when the gas cell's pressure is below 5 bar. Upon reaching 5 bar in the gas cell, we can expedite these procedures by keeping valve 2 open.

Note that after changing the pressure in the gas cell, we should always reoptimize the coupling of the fiber. It often involves moving the lens before the fiber along the fiber direction using the MAX362D stage. The adjustment compensates for the altered refractive index of high-pressure argon, which deviates from that of ambient air. Such variations in refractive index influence the lens's focal length, subsequently affecting the coupling.

4.3.2 Chirped mirrors alignment

Once the fiber is aligned, we align the beam through the chirped mirrors (Layertech 141266). A single chirped mirror is priced at approximately 10 times that of a standard optical mirror. To achieve a negative dispersion of -2500 fs^2, the beam after the fiber must reflect off the chirped mirrors 10 times. If the optical beam reflects only once off each chirped mirror, it results in significant resource inefficiencies, both in terms of cost and spatial utilization on the optical table.

Fig. 4.5 shows a typical alignment for a chirped mirror pair where we achieve 6 bounces on a pair of chirped mirrors. Two critical considerations arise from the alignment.

1. Efficient Spatial Utilization: The goal is to maximize the number of reflections on the chirped mirrors. To achieve this, the two chirped mirrors have to be parallel with each other, with the incident beam approaching mirror #2 at a near-perpendicular angle. Such an angle requires that the edge of the mirror mount for the chirped mirror does not obstruct either the incoming or outgoing beam. For this purpose, the Clear Edge Ultima Mirror Mount (U100-A-LH-2K) from Newport was selected. Also, the knobs on this mirror mount provide a higher fine-tuning capability compared to standard mirror mounts like KM-100 and the Kinetic Mounts from Thorlabs.

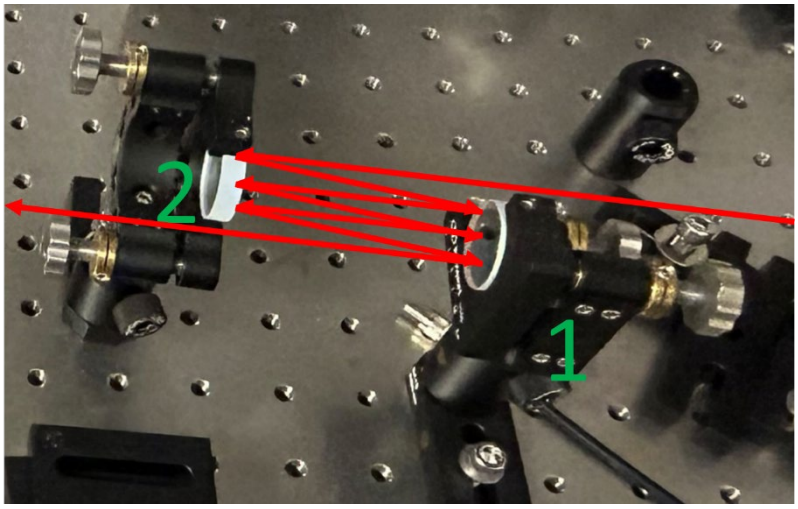

Fig. 4.5 A typical alignment of the chirped mirror to achieve 3 bounces on each mirror in our lab.

2. Avoid Beam Clipping: It is essential to prevent the beam from being clipped by the edges of the chirped mirrors. For an 8 mm ($1/e^2$ diameter) beam emanating from the fiber setup, achieving 3 bounces on each chirped mirror is optimal. In this paper, we put an additional metal mirror behind the chirped mirror #2, reflecting the outgoing beam back onto chirped mirror #1 to achieve another 2 bounces on each chirped mirror. In this configuration, we achieved 10 bounces across the 2 chirped mirrors, albeit with some beam clipping. In the context of this APL Photonics paper, where the primary concern was the NIR pulse duration and bandwidth for THz generation, minor NIR beam clipping was deemed acceptable. In the subsequent applications aiming to guide more power into the THz system, 2 chirped mirror pairs were employed to achieve 10 or 12 bounces.

Chapter 5

Broadband and high-sensitivity time-resolved THz system using grating-assisted tilted-pulse-front phase matching

5.1 Background and relevance

To achieve broadband THz generation based on the difference-frequency mixing in nonlinear crystals, besides a broadband NIR pulse, the phase matching inside the nonlinear crystal is another key factor. As we have discussed in Chapter 2, no crystal in nature is designed for the THz generation of all the desired frequencies. The simplest solution to achieve THz generation and detection with a broad bandwidth is to use a nonlinear crystal having a thickness less than 2 times the coherence length at the THz frequency expected to be generated and detected [77]. However, a thin generation/detection crystal means a short nonlinear interaction length leading to a low THz generation/detection efficiency. With the same setup, thin generation/detection crystals generally lead to a lower signal-to-noise ratio than thick generation/detection crystals.

We have also discussed the tilted-pulse-front THz generation technique inside $LiNbO_3$ and GaAs crystals for high-field THz generation below 2 THz [45,46,78]. Such a THz system requires a crystal wedge cut at a certain crystal orientation and the alignment of the system is more complicated than collinear THz systems. Furthermore, the tilted-pulse-front THz generation system uses imaging optics to image the grating used for pulse-front-tilt on the front surface of the generation crystal. The imaging distortion, which is unavoidable, affects the NIR generation beam quality and as a result, affects the THz generation efficiency inside the crystal [54]. To avoid the imaging distortion, we can realize the pulse-front-tilt with a contact grating at the front surface of the generation crystal. In the introduction of the following paper [79], several trials made by different groups in the world to perform THz generation using contact grating on different crystals have been introduced for the purpose of high-field THz generation below 2 THz. Among them, the

work from J. A. Fülöp and J. Hebling et al. demonstrated the first tilted-pulse-front high-field THz generation with contact grating on a ZnTe crystal [54]. The THz spectrum from this THz source is mostly below 2 THz. Later on, a few more theoretical and experimental works realized tilted-pulse-front phase matching in the THz generation process with a contact grating design in different nonlinear crystals [80,81]. Before the publication of the manuscript in this chapter, there has not been a THz source based on nonlinear semiconductor crystals that can generate high-field THz centered beyond 2 THz. In this work, we demonstrated, for the first time, efficient THz generation above 2 THz with the tilted-pulse-front phase matching using a contact grating. The contact grating design we followed is the phase grating with a rectangular profile [54,82]. Also, as we know from Chapter 2, the THz generation process via DFG and THz detection via electro-optical sampling share the same phase-matching condition. In this sense, the contact grating which is designed to optimize the THz generation process could also be applied to optimize the THz detection process. In 2018, we used the first batch of fabricated gratings on 1 mm-thick GaP crystal to demonstrate the grating-assisted THz detection with tilted-pulse-front phase matching [83] (more information about this paper is in the additional comment in section 5.2). This work also led to a patent [84]. In the manuscript associated to this chapter, we also combined the tilted-pulse-front THz generation and detection in our collinear THz-TDS system, aiming to achieve a broadband THz generation and detection with thick nonlinear crystals while utilizing the long interaction length of the thick crystals to obtain high efficiency. The dual grating-assisted THz generation and detection scheme increased the signal in intensity by a factor of 400 compared to that measured with the collinear scheme using a pair of 0.2 mm-thick GaP crystals for THz generation and detection. Moreover, the dynamic range of the dual grating system has a peak dynamic range of 90 dB at 3 THz which is 30 dB higher than that of a system employing thin GaP crystals for THz generation and detection.

ADVANCED OPTICAL MATERIALS
www.advopticalmat.de

Broadband and High-Sensitivity Time-Resolved THz System Using Grating-Assisted Tilted-Pulse-Front Phase Matching

*Wei Cui, Kashif Masud Awan, Rupert Huber, Ksenia Dolgaleva, and Jean-Michel Ménard**

A broadband and sensitive time-resolved terahertz (THz) configuration relying on noncollinear optical interactions is presented. This noncollinear scheme enables a higher THz generation and detection efficiency in nonlinear crystals. The concept relies on a pair of thick (2 mm) GaP crystals with a phase grating etched on their surface to achieve phase matching between a diffracted near-infrared pulse and a THz wave propagating at normal incidence. This system is compared to a standard collinear scheme based on thin (0.2 mm) crystals and, while both systems provide access to a spectral bandwidth extending up to 6.5 THz, it is found that the noncollinear configuration improves the THz signal by more than a factor of 400 and the dynamic range of the system by 30 dB at a frequency of 3 THz.

1. Introduction

Time-resolved terahertz (THz) spectroscopy is an optical characterization technique now routinely used in the spectral range between 0.5 and 3 THz to monitor microscopic interactions and resolve key signature resonances in diverse materials such as superconductors,[1–4] semiconductors,[5,6] topological insulators,[7–10] heavy fermions,[11–13] ferroelectrics,[14,15] antiferromagnets,[16] and metal-organic compounds.[17,18] One configuration commonly used for these experiments relies on a near infrared (NIR) ultrafast source and a pair of second-order nonlinear crystals to generate and detect phase-locked THz transients.[19]

Recently, there have been considerable efforts to improve time-domain THz systems by broadening their spectral window toward the high-frequency part of the spectrum without losing sensitivity at low frequencies.[20–25] In some cases, the spectral bandwidth and duration of the pulses delivered by the NIR ultrafast source determine the highest THz frequency that can be efficiently resolved by the system. This issue can be addressed with self-phase modulation inside a nonlinear medium broadening the spectrum of these ultrashort pulses and with dispersion compensation optics recompressing the pulse in the time domain.[21,22,26] In other cases, it is the second-order nonlinear crystals used for THz generation and detection that limit the accessible THz bandwidth. However, there is only a short list of candidate crystals suited for these applications since they must possess specific linear and nonlinear optical properties, including a relatively large second-order nonlinear coefficient, a high optical damage threshold (to sustain intense NIR pumping), and a low optical absorption in both the NIR and THz regions. Furthermore, the dispersion and thickness of the crystals are additional parameters that determine the nonlinear interaction length, the coherence length, and, ultimately, the THz signal strength. Interestingly, these latter parameters can be adjusted with the experimental configuration without modifying the crystal material properties. One simple method consists in selecting a crystal thickness equal to the coherence length. This ensures a constructive nonlinear build up during the THz generation and detection processes. However, for broadband applications, this condition often involves a very thin crystal,[27,28] resulting in a low THz signal amplitude due to the short interaction length. A more versatile approach consists in implementing a noncollinear geometry where an angle is formed between the directions of propagation of the NIR and THz pulses. Not only can this scheme be used to adjust phase-matching conditions, and therefore control the accessible THz bandwidth, but it can also be carried out inside a thick crystal to enable a long and efficient nonlinear process.

W. Cui, J.-M. Ménard
Department of Physics
University of Ottawa
25 Templeton Street, Ottawa, Ontario K1N 6N5, Canada
E-mail: jean-michel.menard@uottawa.ca
K. M. Awan
Stewart Blusson
Quantum Matter Institute
2355 East Mall, Vancouver, British Columbia V6T 1Z4, Canada
R. Huber
Institute of Experimental and Applied Physics
University of Regensburg
93053 Regensburg, Germany
K. Dolgaleva
School of Electrical Engineering and Computer Science
University of Ottawa
25 Templeton Street, Ottawa, Ontario K1N 6N5, Canada

The ORCID identification number(s) for the author(s) of this article can be found under https://doi.org/10.1002/adom.202101136.

DOI: 10.1002/adom.202101136

The tilted-pulse-front THz generation technique in $LiNbO_3$ is an example of noncollinear scheme utilized to generate high-field THz pulses centered around 1 THz.[29–32] A similar concept involving a phase grating located at the surface of the generation crystal has also been proposed theoretically[33–38] and demonstrated experimentally.[39,40] This surface grating design can eliminate the imaging distortions occurring in the conventional tilted-pulse-front THz setup, thus leading to an improved THz beam quality.[33,36,39] In this configuration, the grating diffracts the normally incident NIR pulse, which then propagates in a different direction than the emitted THz pulse inside the crystal. While the nonlinear interaction is intrinsically noncollinear, the general setup can remain essentially collinear,[33,35,38,39] thus easier to align since both incoming NIR and emitted THz pulses are impinging on the front surface of the crystal at normal incidence. Recently, a similar phase grating was used on the surface of a THz detection crystal to extend the accessible spectral window and enhance the overall system's sensitivity.[41]

Here we demonstrate a time-resolved THz configuration taking advantage of surface phase gratings to achieve tilted-pulse-front phase matching in both THz generation and detection processes inside thick (2 mm) gallium phosphide (GaP) crystals. A phase grating is etched directly onto the surface of these two crystals to adjust phase-matching conditions and provide access to a spectral bandwidth extending up to 6.5 THz. Most importantly, we maximize the nonlinear interaction length inside a thick crystal leading to THz signal amplitudes >20 times larger than those recorded using a standard collinear geometry relying on a pair of thin (0.2 mm thick) unpatterned GaP crystals. This enhancement factor due to a more efficient THz generation and detection processes is around 400 in signal strength. We also collect data with a standard collinear geometry using a pair of 2 mm thick unpatterned GaP crystals. This system also exhibits a relatively strong signal but the covered spectral bandwidth is limited to the frequencies below 3 THz. The results obtained with both collinear schemes show the typical tradeoff between the THz signal amplitude and the accessible spectral bandwidth. This tradeoff is circumvented in our dual-grating configuration by shifting the optimal phase-matching conditions at higher frequencies, where phase mismatch effects are more critical at a given crystal thickness.

2. Theory

In a standard collinear THz generation (or detection) geometry governed by optical rectification (OR), the phase mismatch corresponds to

$$\Delta k = k(\omega_{\mathrm{NIR}}) - k(\omega_{\mathrm{NIR}} - \omega_{\mathrm{THz}}) - k(\omega_{\mathrm{THz}}) \tag{1}$$

where $k = |\vec{k}|$ is the magnitude of the wavevector and ω is the radial frequency corresponding to any spectral component of the incident NIR pulse (ω_{NIR}) or the generated (or detected) THz pulse (ω_{THz}). In a noncollinear geometry, the phase mismatch has been defined as[30,31,41,42]

$$\Delta k = \frac{k(\omega_{\mathrm{NIR}}) - k(\omega_{\mathrm{NIR}} - \omega_{\mathrm{THz}})}{\cos\theta} - k(\omega_{\mathrm{THz}}) \tag{2}$$

where θ is the angle formed by the direction of propagation of the diffracted NIR pulse relative to the direction of propagation of the THz pulse. The condition to achieve perfect phase matching can be expressed as[43]

$$\theta = \cos^{-1}\frac{n_g(\omega_{\mathrm{NIR}})}{n(\omega_{\mathrm{THz}})} \tag{3}$$

Therefore, the angle θ can be a control knob to adjust phase matching. We consider the configuration where the NIR pulse impinges on the grating at normal incidence. Then, the diffracted orders have a pulse front parallel to the crystal surface, which corresponds to a tilt angle γ equal to the diffraction angle $\gamma = \theta = \sin^{-1}(\lambda/n\Lambda)$, where λ is the central wavelength of the NIR pulse in vacuum, n is the refractive index of the crystal and Λ is the pitch of the grating.

3. Experiments

We use a time-domain THz configuration based on an NIR ultrafast source centered at 1035 nm and delivering 60 fs pulses at a repetition rate of 1.1 MHz. Phase-locked THz transients are generated by optical rectification of these NIR pulses in a (110)-oriented GaP crystal and then detected by electro-optical sampling inside an identical crystal.[21,22] The NIR pulse incident on the THz generation crystal has a spot size of 24.8 μm ($1/e^2$ diameter) and an energy of 0.5 μJ. The NIR gating pulse incident on the THz detection crystal has a spot size of 8.2 μm ($1/e^2$ diameter) and an energy of 291 pJ if the configuration uses a phase grating at the surface of the crystal. When an unpatterned detection crystal is used instead, the gating pulse energy is reduced to 58 pJ to ensure that all the measurements are performed with the same optical power impinging on the photodiodes. This allows us to directly compare the performances of different system configurations. A mechanical stage enables point-by-point sampling of the terahertz waveform while a lock-in amplifier with a time constant of 30 and 200 ms waiting time allows sensitive acquisition of 1000 points in about 5 min. We then use the Fourier transform of the time-domain data to obtain the THz spectrum. Our tilted-pulse-front phase-matching schemes for THz generation and detection processes (schematically represented in **Figure 1**) rely on binary gratings etched at the surface of 2 mm thick GaP crystals to diffract incident NIR pulses. In the detection scheme, the THz pulse incident on the crystal is not diffracted by the periodic surface modulation due to its longer wavelength. The grating is oriented horizontally, allowing the TE-polarized NIR pulse to keep its polarization orientation unchanged upon diffraction. This geometry allows us to directly compare results obtained with diffracted and non-diffracted NIR pulses since both configurations involve the same projection of the pulses' polarization components onto the crystal's nonlinear tensor elements. The grating pitch Λ = 1.635 μm is selected from Equation (3) to satisfy phase-matching conditions between the diffracted NIR pulse and the THz component at 4 THz propagating along the

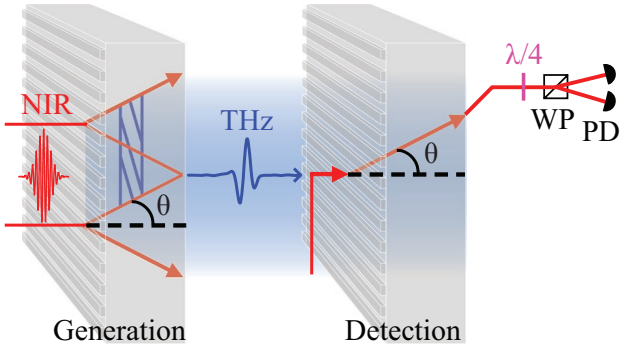

Figure 1. Schematic representation of the noncollinear dual grating configuration. A periodic modulation (Λ = 1.635 µm) at the surface of both THz generation and detection crystals diffracts the incoming NIR pulse. Tilted-pulse-front phase matching is satisfied at the frequency 4 THz. In the generation process, both first diffraction orders (m = –1, +1) contribute to the generated THz wave, while the detection relies on a single diffracted order, which is monitored in polarization as we perform electro-optical sampling. NIR: near infrared; THz: terahertz; λ/4: quarter-wave plate; WP: Wollaston prism; PD: photodetector.

direction of normal incidence, leading to a diffraction angle of 11.7° inside the GaP crystal. The grating's filling ratio is 50%, and the modulation depth is optimized to approach 245 nm during the fabrication process, which is based on the reactive ion etching (see details in Supporting Information).[41] This precise height corresponds to an optical phase difference of π to achieve destructive interference in the 0th order and maximize the signal (theoretically ≈80%) in the first diffracted orders.[44] In our experiment, we confirm a low percentage (7%) of the total transmitted power in the 0th order and obtain 61% of the transmitted power in the ±1 orders. This efficient power redistribution is crucial for efficient noncollinear THz generation involving OR of the first diffracted orders. For the noncollinear detection scheme, optimal grating diffraction in the first order is preferable, but not essential, since the detected signal is normalized by the intensity of the diffracted NIR pulse.

4. Results and Discussion

We first investigate the THz generation process with two crystals of different thicknesses and, more importantly, compare results obtained with the collinear and noncollinear geometries. As such, we measure THz signals produced inside three different generation GaP crystals with the following characteristics: 0.2 mm thick and unpatterned surface ($C_{0.2}$), 2 mm thick and unpatterned surface (C_2), and 2 mm thick with a phase grating on the incident surface (C_2^{PG}). Nonlinear THz detection is performed in this first set of experiments with another $C_{0.2}$ crystal. The black and red lines in **Figure 2** correspond to the two unpatterned generation crystals with the thicknesses of 0.2 mm ($C_{0.2}$) and 2 mm (C_2), respectively. The thickest crystal (red curve) yields the largest signal amplitude in the low-frequency part of the spectrum, while the thin crystal (black curve) possesses a larger spectral bandwidth, even leading to higher signal amplitudes at frequencies above 4 THz. These results illustrate the tradeoff between signal amplitude and spectral bandwidth. The noncollinear THz generation geometry

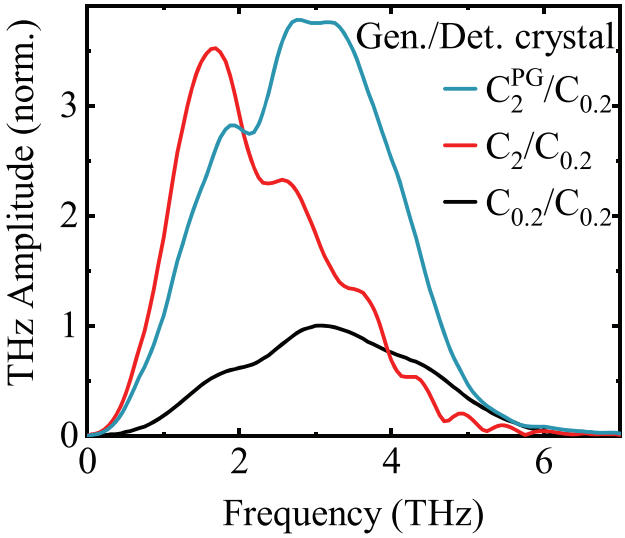

Figure 2. THz spectral amplitude measured with three different THz generation GaP crystals: $C_{0.2}$ and C_2 are unpatterned and have thicknesses of 0.2 and 2 mm, respectively, while C_2^{PG} is 2 mm thick and has a phase grating (PG) on its incident surface. Nonlinear THz detection is performed inside another $C_{0.2}$. The displayed THz spectral amplitudes are normalized by the maximum signal obtained when $C_{0.2}$ is used for both THz generation and detection processes.

(cyan curve) is implemented by a phase grating on a 2 mm thick crystal (C_2^{PG}) with a pitch selected to satisfy phase-matching conditions at 4 THz. This optimization of phase-matching conditions combined with the fact that low THz frequencies are inherently associated with longer nonlinear coherence lengths [45] effectively broadens the signal spectral bandwidth. In comparison with the results obtained with $C_{0.2}$, we find that the noncollinear geometry leads to a large THz spectral bandwidth and a larger signal amplitude, by a factor of 3.8 at 3 THz. The maximum amplitude obtained with C_2^{PG} is comparable to the one obtained with C_2, but it is now centered at 3 THz instead of 1.7 THz.

In another series of experiments involving the same three crystals presented above, we change the detection crystal in the electro-optical sampling part of the time-domain THz setup, while keeping $C_{0.2}$ as the generation crystal. Results in **Figure 3** obtained with the detection crystals $C_{0.2}$ (black curve) and C_2(orange curve) show a strong signal dependence on the crystal thickness, which is similar to the one seen in Figure 2 when the positions of the generation and detection crystals were inverted. In a grating-assisted noncollinear THz detection geometry, provided by C_2^{PG} (blue curve), we observe a relatively large spectral bandwidth comparable to the one obtained with $C_{0.2}$. More importantly, the relative signal amplitude is now much larger. At the peak amplitude, the signal is a factor of ≈9 higher than the one measured with $C_{0.2}$, and also a factor of ≈2 higher than the one measured with C_2. This increase is due to an intrinsic polarization filtering effect occurring at the back surface of the detection crystal.[41,46,47] Briefly, partial reflection of the s-polarized component of the diffracted NIR pulse reduces the total power on the photodiodes, while the p-polarized component containing the THz information, is preferentially transmitted. Since the THz signal is normalized

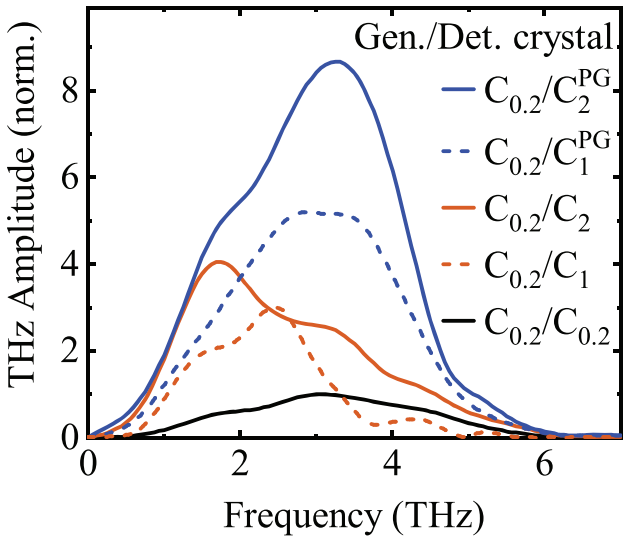

Figure 3. THz spectral amplitude measured with three different THz detection GaP crystals: $C_{0.2}$, C_1,[41] and C_2 are unpatterned and have thicknesses of 0.2, 1, and 2 mm, respectively, while C_1^{PG}[41] and C_2^{PG} are 1 and 2 mm thick, respectively, and have a phase grating (PG) on their incident surface. Nonlinear THz generation is performed inside another $C_{0.2}$ crystal. The displayed THz spectral amplitudes are normalized by the maximum signal obtained when $C_{0.2}$ is used for both THz generation and detection processes.

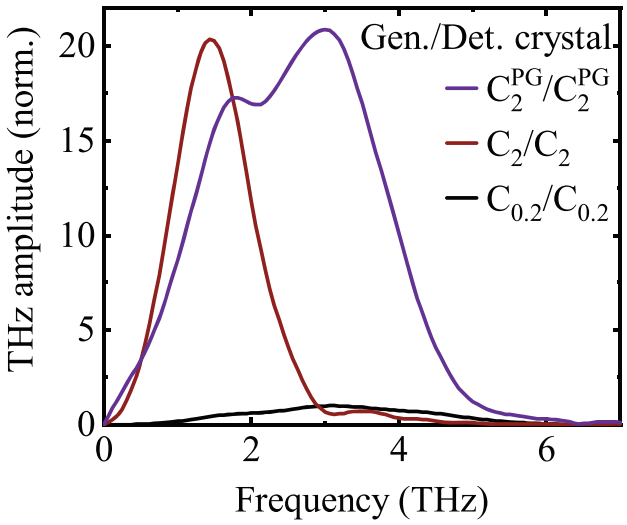

Figure 4. THz spectral amplitude measured with three pairs of identical generation and detection GaP crystals having thicknesses of 0.2 and 2 mm. A phase grating (PG) on the incident surface of a 2 mm thick crystal modulates phase-matching conditions to enhance THz generation and detection above 2 THz.

by the power incident on the photodiodes, the spectral amplitude obtained with C_2^{PG} is therefore larger. Our group also previously reported a noncollinear geometry inside a 1 mm thick GaP crystal, the results of which are added to Figure 3 for comparison (dashed lines).[41] We observe that increasing the thickness of the crystal by a factor of 2 in a noncollinear geometry increases the amplitude by a factor of 1.5. This discrepancy can be attributed to a gradual loss of spatial overlap between the NIR and THz pulses as they propagate in different directions inside the crystal. This ultimately sets a limit on the maximum angular deflection and effective crystal thickness for this detection scheme.

In a third experiment, we perform noncollinear THz generation and detection with a pair of C_2^{PG} (purple curve) and compare the measured signal amplitude with the one obtained with a pair of unpatterned $C_{0.2}$ (black curve; same shown in Figures 2 and 3) and a pair of unpatterned C_2 (dark red curve). The collinear C_2/C_2 configuration for nonlinear THz generation/detection yields a limited spectral bandwidth but a large signal amplitude peaking at 1.5 THz. This amplitude is a factor of 20 larger than the maximum spectral amplitude measured with a configuration using a pair of $C_{0.2}$. The dual patterned crystal configuration C_2^{PG}/C_2^{PG} enables a long nonlinear interaction length which contributes to a large THz peak amplitude, comparable to the one obtained with C_2/C_2, while the spectral bandwidth still extends up to 6.5 THz on a linear scale. We also perform simulations solving the coupled wave equations[45] in the frequency domain and found good qualitative agreement with our experimental data. These simulated spectra are presented in Figures S1–S4 (Supporting Information).

Figure 4 clearly indicates a net advantage in terms of signal amplitude and spectral bandwidth in using a dual noncollinear configuration in time-resolved THz spectroscopy. For any spectroscopy applications, another crucial parameter is the dynamic range allowing us to determine the ability of a system to characterize samples, especially when they are strongly absorptive. To investigate this value, we collect the THz amplitude $E(\omega)$ and the noise floor $\varepsilon(\omega)$ corresponding to the absolute square of the recorded signal when the THz pulse is blocked. The dynamic range (DR) is then defined by[48,49]

$$\mathrm{DR} = \left|E(\omega)\right|^2 / \varepsilon(\omega) \tag{4}$$

We focus on the two configurations in Figure 4 providing the largest spectral bandwidth: $C_{0.2}/C_{0.2}$ and C_2^{PG}/C_2^{PG}. **Figure 5**a shows on a log scale that both configurations yield similar spectral bandwidth, with a signal extending up to 6.5 THz, after which the spectral power approaches the noise level corresponding to the fluctuations in the THz signal amplitude. The noise floor (thinner lines in Figure 5a) is obtained by performing a regular time-resolved scan while blocking the THz beam. The noise is fitted with the model: $A^*(1/f + B)$, where both A and B are fitting parameters and f is the frequency. This model includes a term inversely proportional to the frequency to account for the flicker noise ($1/f$ noise or pink noise).[49,50] Using the fitted noise curves and spectral power curve, we extract the DR, which has a maximum of 60 dB with the $C_{0.2}/C_{0.2}$ configuration, and 90 dB with the C_2^{PG}/C_2^{PG} configuration. This 30 dB improvement is mainly due to the higher-amplitude signal generated and detected in a thick nonlinear crystal, but also partially due to the intrinsic polarization filtering effect at the back surface of the detection crystal enhancing the detection sensitivity. Overall, the dynamic range obtained with the dual grating configuration is >80 dB over a relatively broad bandwidth extending from 1.1 to 4.3 THz.

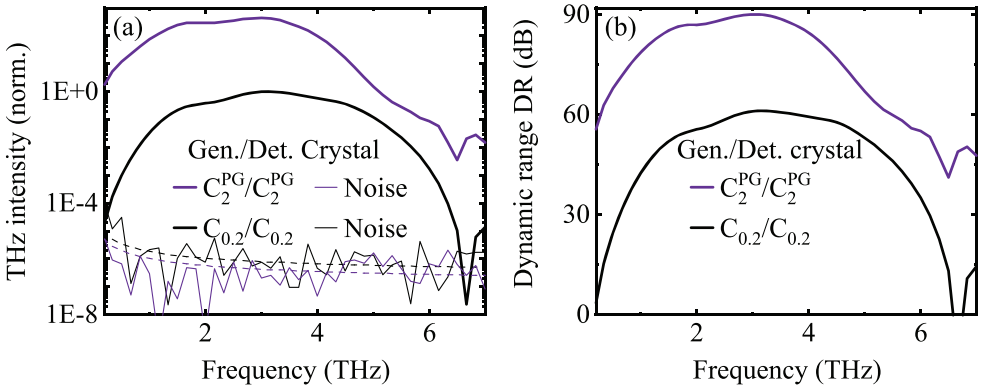

Figure 5. a) THz spectral intensities and the noise floors measured with 2 pairs of identical generation and detection GaP crystals having a thickness of 0.2 and 2 mm. A phase grating (PG) on the incident surface of a 2 mm thick crystal modulates phase-matching conditions to enhance THz generation and detection above 2 THz. The dashed lines are the noise floors fitted with the model $A^*(1/f+B)$, where both A and B are fitting parameters and f is the frequency. b) Dynamic ranges calculated based on Equation (4) and the measurement results in (a).

5. Conclusion

Our configuration based on a pair of nonlinear GaP crystals with a surface phase grating overcomes some limits imposed by phase-matching conditions at normal incidence, while allowing a longer nonlinear interaction length to achieve high signal amplitude over a large bandwidth. We notably achieve a dynamic range above 80 dB between 1.1 and 4.3 THz and obtain a peak dynamic range of 90 dB at 3 THz. This represents a 30 dB improvement in comparison to signals collected with the same system using thin (0.2 mm) unpatterned GaP generation and detection crystals.

Our system sensitivity could be further improved by combining our technique with other techniques, including a continuous data acquisition technique.[51,52] Our concept can be easily implemented in a standard THz-TDS system, since the crystals with an etched phase grating can simply replace the conventional (unpatterned) generation and detection crystals. Only minimum adjustments are required in the detection stage to direct one of the first diffracted orders into the EO detection system.

Although this work focuses only on improving spectroscopy applications in the region between 3 and 6.5 THz using GaP as a nonlinear crystal, the idea can be applied to other materials to improve THz generation and detection in other spectral regions. This technique can be applied to a wide range of nonlinear crystals and with different types of optical sources to optimize phase-matching conditions at specific THz frequencies. Table S1 (Supporting Information) shows calculated diffraction angles to achieve tilted-pulse-front phase matching in common nonlinear THz crystals for optimal THz generation and detection at 1 and 3 THz. Since our simple noncollinear geometry allows phase-matching conditions to be adjusted, a broader range of nonlinear materials may also become appealing to THz applications.[53] Finally, our results pave the way toward efficient THz spectroscopy across a broad bandwidth and could enable high-field THz generation at frequencies above 3 THz.

Supporting Information

Supporting Information is available from the Wiley Online Library or from the author.

Acknowledgements

J.-M.M. acknowledges funding from the Natural Sciences and Engineering Research Council of Canada (NSERC) Discovery Grant RGPIN-2016-04797, the Canada Foundation for Innovation (CFI) (Project Number 35269), and the Alexander von Humboldt Foundation. K.D. acknowledges Canada Research Chairs program and NSERC Discovery Grant RGPIN-2020-03989.

Conflict of Interest

The authors declare no conflict of interest.

Data Availability Statement

Research data are not shared.

Keywords

broadband, grating-assisted tilted-pulse-front phase matching, high-sensitivity, time-resolved terahertz system

Received: June 6, 2021
Revised: September 18, 2021
Published online: October 19, 2021

[1] S. Rajasekaran, J. Okamoto, L. Mathey, M. Fechner, V. Thampy, G. D. Gu, A. Cavalleri, *Science* **2018**, *359*, 575.
[2] X. Yang, L. Luo, M. Mootz, A. Patz, S. L. Bud'ko, P. C. Canfield, I. E. Perakis, J. Wang, *Phys. Rev. Lett.* **2018**, *121*, 267001.
[3] P. Chauhan, F. Mahmood, D. Yue, P.-C. Xu, X. Jin, N. P. Armitage, *Phys. Rev. Lett.* **2019**, *122*, 017002.
[4] F. Mahmood, X. He, I. Božović, N. P. Armitage, *Phys. Rev. Lett.* **2019**, *122*, 027003.
[5] E. Cinquanta, D. Meggiolaro, S. G. Motti, M. Gandini, M. J. P. Alcocer, Q. A. Akkerman, C. Vozzi, L. Manna, F. De Angelis, A. Petrozza, S. Stagira, *Phys. Rev. Lett.* **2019**, *122*, 166601.
[6] X. Li, K. Yoshioka, Q. Zhang, N. M. Peraca, F. Katsutani, W. Gao, G. T. Noe II, J. D. Watson, M. J. Manfra, I. Katayama, J. Takeda, J. Kono, *Phys. Rev. Lett.* **2020**, *125*, 167401.

[7] K. N. Okada, Y. Takahashi, M. Mogi, R. Yoshimi, A. Tsukazaki, K. S. Takahashi, N. Ogawa, M. Kawasaki, Y. Tokura, *Nat. Commun.* **2016**, *7*, 12245.
[8] J. Reimann, S. Schlauderer, C. P. Schmid, F. Langer, S. Baierl, K. A. Kokh, O. E. Tereshchenko, A. Kimura, C. Lange, J. Güdde, U. Höfer, R. Huber, *Nature* **2018**, *562*, 396.
[9] L. Luo, X. Yang, X. Liu, Z. Liu, C. Vaswani, D. Cheng, M. Mootz, X. Zhao, Y. Yao, C.-Z. Wang, K.-M. Ho, I. E. Perakis, M. Dobrowolska, J. K. Furdyna, J. Wang, *Nat. Commun.* **2019**, *10*, 607.
[10] S. Sim, S. Lee, J. Moon, C. In, J. Lee, M. Noh, J. Kim, W. Jang, S. Cha, S. Y. Seo, S. Oh, D. Kim, A. Soon, M.-H. Jo, H. Choi, *ACS Photonics* **2020**, *7*, 759.
[11] C. Wetli, S. Pal, J. Kroha, K. Kliemt, C. Krellner, O. Stockert, H. v. Löhneysen, M. Fiebig, *Nat. Phys.* **2018**, *14*, 1103.
[12] S. Pal, C. Wetli, F. Zamani, O. Stockert, H. v. Löhneysen, M. Fiebig, J. Kroha, *Phys. Rev. Lett.* **2019**, *122*, 096401.
[13] L. Prochaska, X. Li, D. C. MacFarland, A. M. Andrews, M. Bonta, E. F. Bianco, S. Yazdi, W. Schrenk, H. Detz, A. Limbeck, Q. Si, E. Ringe, G. Strasser, J. Kono, S. Paschen, *Science* **2020**, *367*, 285.
[14] S. Pal, N. Strkalj, C.-J. Yang, M. C. Weber, M. Trassin, M. Woerner, M. Fiebig, *Phys. Rev. X* **2021**, *11*, 021023.
[15] G. Folpini, K. Reimann, M. Woerner, T. Elsaesser, J. Hoja, A. Tkatchenko, *Phys. Rev. Lett.* **2017**, *119*, 097404.
[16] S. Schlauderer, C. Lange, S. Baierl, T. Ebnet, C. P. Schmid, D. C. Valovcin, A. K. Zvezdin, A. V. Kimel, R. V. Mikhaylovskiy, R. Huber, *Nature* **2019**, *569*, 383.
[17] B. Pattengale, J. Neu, S. Ostresh, G. Hu, J. A. Spies, R. Okabe, G. W. Brudvig, C. A. Schmuttenmaer, *J. Am. Chem. Soc.* **2019**, *141*, 9793.
[18] J. Nyakuchena, S. Ostresh, D. Streater, B. Pattengale, J. Neu, C. Fiankor, W. Hu, E. D. Kinigstein, J. Zhang, X. Zhang, C. A. Schmuttenmaer, J. Huang, *J. Am. Chem. Soc.* **2020**, *142*, 21050.
[19] P. U. Jepsen, D. G. Cooke, M. Koch, *Laser Photonics Rev.* **2011**, *5*, 124.
[20] K. Aoki, J. Savolainen, M. Havenith, *Appl. Phys. Lett.* **2017**, *110*, 201103.
[21] W. Cui, A. W. Schiff-Kearn, E. Zhang, N. Couture, F. Tani, D. Novoa, P. St. J. Russell, J.-M. Ménard, *APL Photonics* **2018**, *3*, 111301.
[22] A. Halpin, N. Couture, J.-M. Ménard, *Opt. Mater. Express* **2019**, *9*, 3115.
[23] J. Drs, N. Modsching, C. Paradis, C. Kränkel, V. J. Wittwer, O. Razskazovskaya, T. Südmeyer, *J. Opt. Soc. Am. B* **2019**, *36*, 3039.
[24] G. Barbiero, H. Wang, J. Brons, B.-H. Chen, V. Pervak, H. Fattahi, *J. Phys. B: At. Mol. Opt. Phys.* **2020**, *53*, 125601.
[25] D. Jang, J. H. Sung, S. K. Lee, C. Kang, K.-Y. Kim, *Opt. Lett.* **2020**, *45*, 3617.
[26] R. Piccoli, A. Rovere, Y.-G. Jeong, Y. Jia, L. Zanotto, F. Légaré, B. E. Schmidt, R. Morandotti, L. Razzari, *Opt. Express* **2019**, *27*, 32659.
[27] A. Leitenstorfer, S. Hunsche, J. Shah, M. C. Nuss, W. H. Knox, *Appl. Phys. Lett.* **1999**, *74*, 1516.
[28] R. Huber, B. A. Schmid, R. A. Kaindl, D. S. Chemla, *Phys. Status Solidi B* **2008**, *245*, 1041.
[29] J. Hebling, G. Almási, I. Kozma, J. Kuhl, *Opt. Express* **2002**, *10*, 1161.
[30] J. Hebling, A. G. Stepanov, G. Almási, B. Bartal, J. Kuhl, *Appl. Phys. B* **2004**, *78*, 593.
[31] J. Hebling, K.-L. Yeh, M. C. Hoffmann, B. Bartal, K. A. Nelson, *J. Opt. Soc. Am. B* **2008**, *25*, B6.
[32] F. Blanchard, B. E. Schmidt, X. Ropagnol, N. Thiré, T. Ozaki, R. Morandotti, D. G. Cooke, F. Légaré, *Appl. Phys. Lett.* **2014**, *105*, 241106.
[33] L. Pálfalvi, J. A. Fülöp, G. Almási, J. Hebling, *Appl. Phys. Lett.* **2008**, *92*, 171107.
[34] K. Nagashima, A. Kosuge, *Jpn. J. Appl. Phys.* **2010**, *49*, 122504.
[35] M. I. Bakunov, S. B. Bodrov, *J. Opt. Soc. Am. B* **2014**, *31*, 2549.
[36] Z. Ollmann, J. Hebling, G. Almási, *Appl. Phys. B* **2012**, *108*, 821.
[37] Z. Ollmann, J. A. Fülöp, J. Hebling, G. Almási, *Opt. Commun.* **2014**, *315*, 159.
[38] P. S. Nugraha, G. Krizsán, Gy. Polónyi, M. I. Mechler, J. Hebling, G. Tóth, J. A. Fülöp, *J. Phys. B: At. Mol. Opt. Phys.* **2018**, *51*, 094007.
[39] J. A. Fülöp, Gy. Polónyi, B. Monoszlai, G. Andriukaitis, T. Balciunas, A. Pugzlys, G. Arthur, A. Baltuska, J. Hebling, *Optica* **2016**, *3*, 1075.
[40] M. Tsubouchi, K. Nagashima, F. Yoshida, Y. Ochi, M. Maruyama, *Opt. Lett.* **2014**, *39*, 5439.
[41] A. Halpin, W. Cui, A. W. Schiff-Kearn, K. M. Awan, K. Dolgaleva, J.-M. Ménard, *Phys. Rev. Appl.* **2019**, *12*, 031003.
[42] J. A. Fülöp, L. Pálfalvi, G. Almási, J. Hebling, *Opt. Express* **2010**, *18*, 12311.
[43] A. Nahata, A. S. Weling, T. F. Heinz, *Appl. Phys. Lett.* **1996**, *69*, 2321.
[44] J. E. Harvey, R. N. Pfisterer, *Opt. Eng.* **2019**, *58*, 087105.
[45] R. W. Boyd, *Nonlinear Optics*, 4th ed., Academic Press, San Diego, CA **2020**.
[46] M. Porer, J.-M. Ménard, R. Huber, *Opt. Lett.* **2014**, *39*, 2435.
[47] S. Ahmed, J. Savolainen, P. Hamm, *Rev. Sci. Instrum.* **2014**, *85*, 013114.
[48] M. Naftaly, R. Dudley, *Opt. Lett.* **2009**, *34*, 1213.
[49] J. Neu, C. A. Schmuttenmaer, *J. Appl. Phys.* **2018**, *124*, 231101.
[50] P. Horowitz, W. Hill, *The Art of Electronics*, 3rd edition, Cambridge University Press, New York, NY, USA **2015**.
[51] B. Urbanek, M. Möller, M. Eisele, S. Baierl, D. Kaplan, C. Lange, R. Huber, *Appl. Phys. Lett.* **2016**, *108*, 121101.
[52] C. Hoberg, P. Balzerowski, M. Havenith, *AIP Adv.* **2019**, *9*, 035348.
[53] L. Tokodi, A. Buzády, J. Hebling, L. Pálfalvi, *Appl. Phys. B* **2016**, *122*, 235.

Supporting Information

Broadband and high-sensitivity time-resolved THz system using grating-assisted tilted-pulse-front phase matching

*Wei Cui, Kashif Masud Awan, Rupert Huber, Ksenia Dolgaleva, and Jean-Michel Ménard**

This document provides supplementary information to "Broadband and high-sensitivity time-resolved THz with grating-assisted tilted-pulse-front phase matching". We show that numerically simulated THz spectra agree well with experimental data in terms of overall spectral shape and bandwidth. We also include the measured time-domain THz signals corresponding to the THz spectra of Figures 2-4 of the main text. A section describing the fabrication process of the phase grating on GaP is also included at the end.

Numerical simulations:

Figure S1 shows the simulation results of the THz spectra generated and detected with the same combinations of GaP crystals than the measurements displayed in Figures 2-4 of the main article. We simulate the THz generation process by numerically solving the coupled wave equation for the difference-frequency mixing process [1]. We use the measured spectrum of our NIR pulse as the input of the simulation and consider a flat phase across the spectrum so that the difference-frequency generation can involve all the possible combinations of spectral components contained within the NIR pulse bandwidth. The dispersion information of the GaP in the NIR range [2] and the THz range [3] are considered to calculate the phase-matching conditions and the THz absorption in the GaP crystal. The phase-matching conditions for the unpatterned and patterned crystal are calculated following Eqs. (1) and (2) of the main text. The spectral dependence of the nonlinear coefficient of GaP is taken into account [4]. The THz detection part of this simulation follows the well-

established electro-optical sampling theory [5]. This part of the simulation calculates the detected THz amplitude considering the frequency-dependent electro-optical sampling coefficient of GaP [4], the autocorrelation function of the NIR detection pulse, and the phase-matching condition. Then, we consider the intrinsic polarization filtering effect [6] enhancing the THz detection efficiency in the patterned GaP crystal, which is obtained by calculating the ratio between the Fresnel transmission coefficients of the p- and s-polarized NIR beams incident on the back surface of the GaP with an incident angle equal to the grating diffraction angle.

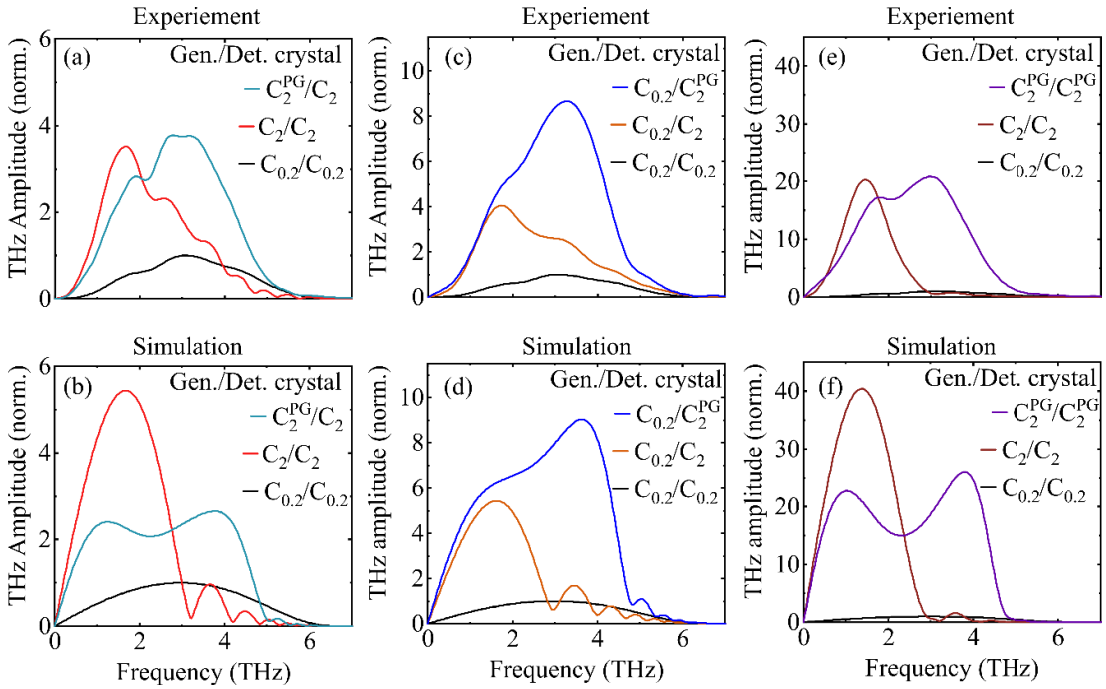

Figure S1. THz spectral amplitudes obtained experimentally (on top row) and from numerical simulations (on bottom row). In (a) and (b) we explore the THz spectra corresponding to a configuration based on three different THz generation GaP crystals while the detection crystal is a 0.2 mm-thick GaP window. In (c) and (d), we investigate the opposite situation where the generation process uses a fixed 0.2 mm-thick GaP window while we consider three different THz detection GaP crystals. Finally in (e) and (f), we use three pairs of identical generation and detection GaP crystals. Note that $C_{0.2}$ and C_2 correspond to unpatterned GaP window with a thickness of 0.2 mm and 2 mm, respectively, while C_2^{PG} is a 2 mm-thick window with a phase grating on its incident surface. The displayed THz spectral amplitudes are normalized by the maximum signal obtained when $C_{0.2}$ is used for both THz generation and detection processes.

Time-domain data:

Figure S2 shows the measured THz time-domain signals corresponding to the THz spectra of Figures 2-4 of the main article. These THz transients are collected with a 30 ms lock-in time constant and a 5 fs step size controlled by a motorized delay stage. A full transient can be measured in 5 mins or less.

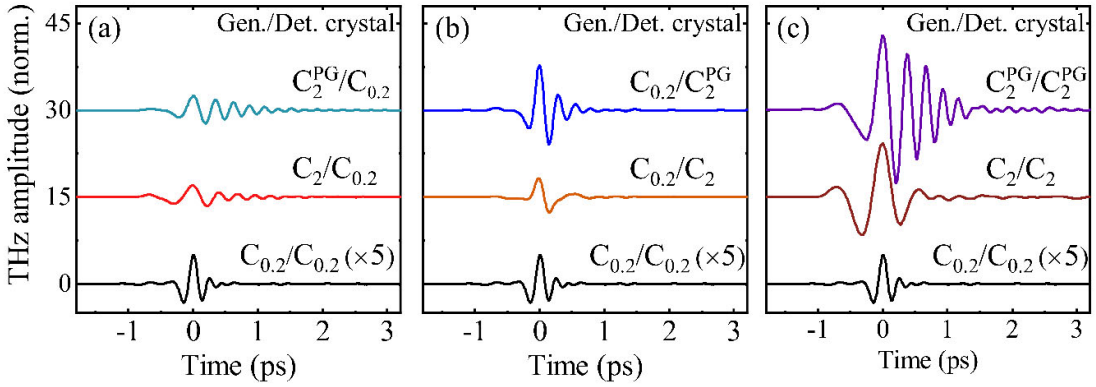

Figure S2. THz time-domain amplitude measured with (a) three different THz generation GaP crystals and a fixed 0.2 mm-thick GaP detection crystal, (b) three different THz detection crystals and a fixed 0.2 mm-thick GaP generation crystal (c) three pairs of identical generation and detection GaP crystals. The displayed THz spectral amplitudes are normalized by the maximum signal obtained when $C_{0.2}$ is used for both THz generation and detection processes.

Figures S2 a, b and c show the time-domain THz signals corresponding to Figures 2, 3 and 4 of the main text, respectively. Note that the signal with the highest field strength is obtained when both generation and detection crystals have a phase grating etched on their incident surface (C_2^{PG}/C_2^{PG}).

Phase grating fabrication:

The lithographic technique used to fabricate the grating on the surface of GaP follows the general steps described in Ref. [6]. A positive-tone electron-beam resist is spin-coated on the surface of GaP at 2000 rpm for 1 min and then baked for 2 mins at 180 °C. We write the grating pattern with a 100-kV electron-beam-lithography system using a dose of 300 μC/cm^2.

Then the sample is developed in N-amyl acetate for 1 min. The transfer of the grating onto the semiconductor is done through plasma etching using a Samco inductively coupled plasma-ion-etching (ICP-RIE system). The process gas in the system is BCl_3 at 2.5 sccm and we use a 50-W ICP power and 25-W radio frequency power at a pressure of 0.15 Pa. A 2 min and 20 s etching time results in a 250 nm etching depth approximately. The remaining resist is removed in the commercially available 1165 remover at 80 °C. In this way, a phase-grating pattern is transferred onto the GaP surface. Two 1×1 cm^2 gratings are fabricated on 2 separate GaP samples. A scanning electron microscope image of the sample was not taken since it requires a thin gold deposition that would render the device ineffective.

Candidate crystals for surface phase grating technique:

Table S1. Properties of some common THz crystals suitable for tilted pulse front phase matching and their corresponding noncollinear angle for efficient generation at a frequency of 1 THz (ϑ_{1THz}) or 3 THz (ϑ_{3THz}). We also consider three scenarios involving optical sources centered at a wavelength of 800 nm, 1030 nm or 1550 nm. Perfect (collinear) phase matching is achieved when the refractive index (n) at a THz frequency is equal to the group index (n_g) in the NIR region.

Material	n_{1THz}	n_{3THz}	$n_g^{0.8\mu m}$	θ_{1THz} (^{o})	θ_{3THz} (^{o})	$n_g^{1.03\mu m}$	θ_{1THz} (^{o})	θ_{3THz} (^{o})	$n_g^{1.55\mu m}$	θ_{1THz} (^{o})	θ_{3THz} (^{o})	*Ref*
ZnTe	3.17	3.37	3.13	9.11	21.75	2.98	19.94	27.84	2.81	27.57	33.51	[7-10]
CdTe	3.24	3.65	3.13	14.97	30.96	3.13	14.97	30.96	2.81	29.86	39.65	[7,9,11,12]
$LiNbO_3$	4.96	5.26	2.36	61.59	63.34	2.3	62.37	64.07	2.26	62.89	64.55	[13-15]
$LiTaO_3$	6.3	7.42	2.23	69.27	72.51	2.018	71.3	74.2	2.15	70.05	73.16	[16, 17]
GaP	3.34	3.36	3.58	-	-	3.31	7.69	9.9	3.16	18.9	19.87	[12, 18, 19]
GaSe (ne)	2.88	2.98	2.85	8.28	16.99	2.62	24.53	28.45	2.49	30.16	33.32	[20]
GaSe (no)	3.27	3.4	3.17	14.2	21.2	2.96	24.15	29.47	2.82	30.41	33.96	[20]
GaAs	3.59	3.63	4.18	-	-	3.99	-	-	3.56	7.41	11.27	[12, 21-23]
DAST	-[a]	2.3	3.39	-	-	2.6	-	-	2.25	-	11.97	[24, 25]

[a] *There is strong absorption at 1 THz in DAST.*[25]

References

[1] R. W. Boyd, *Nonlinear Optics*, 4th ed., Academic Press, San Diego, CA **2020**.

[2] W. L. Bond, Journal of Applied Physics **1965**, 36, 1674.

[3] D. F. Parsons and P. D. Coleman, Appl. Opt. **1971**, 10, 1683.

[4] S. Casalbuoni, H. Schlarb, B. Schmidt, P. Schmüser, B. Steffen, and A. Winter, Phys. Rev. ST Accel. Beams **2008**, 11, 072802.

[5] G. Gallot and D. Grischkowsky, J. Opt. Soc. Am. B **1999**, 16, 1204.

[6] A. Halpin, W. Cui, A. W. Schiff-Kearn, K. M. Awan, K. Dolgaleva, and J.-M. Ménard, Phys. Rev. Applied **2019**, 12, 031003.

[7] K. Wynne and J. J. Carey, Opt. Commun. **2015**, 256, 400.

[8] M. Schall, M. Walther, and P. Uhd Jepsen, Phys. Rev. B **2001**, 64, 094301.

[9] D. T. F. Marple, J. Appl. Phys. **1964**, 35, 539.

[10] G. Gallot, J. Zhang, R. W. McGowan, T. Jeon, D. Grischkowsky, Applied Physics Letters, **1999**, 74, 3450

[11] R. E. Treharne, A. Seymour-Pierce, K. Durose, K. Hutchings, S. Roncallo, D. Lane, *J. Phys.: Conf. Ser.* **2011**, 286 012038

[12] E. D. Palik, *Handbook of Optical constants*, Academic Press, San Diego, CA **1985**.

[13] M. Nakamura, S. Higuchi, S. Takekawa, K. Terabe, Y. Furukawa, and K. Kitamura, Jpn. J. Appl. Phys., Part 1 **2002**, 41, L49.

[14] L. Pálfalvi, J. Hebling, J. Kuhl, A. Péter, and K. Polgár, J. Appl. Phys. **2005**, 97, 123505.

[15] D. E. Zelmon, D. L. Small, and D. Jundt, J. Opt. Soc. Am. B, **1997**, 14, 3319

[16] H. Igawa, T. Mori, S. Kojima, Jpn. J. Appl. Phys., **2014**, 53, 05FE01

[17] K. Moutzouris, G. Hloupis, I. Stavrakas, D. Triantis, and M. -H. Chou, Optical Materials Express, **2011**, 1, 458

[18] W. L. Bond, J. Appl. Phys. **1965**, 36, 1674.

[19] D. F. Parsons and P. D. Coleman, Appl. Opt. **1971**, 10, 1683.

[20] K. Kato, F. Tanno, and N. Umemura, Appl. Opt. **2013**, 52, 2325.

[21] D. Grischkowsky, S. Keiding, M. van Exter, and C. Fattinger, J. Opt. Soc. Am. B **1990**, 7, 2006.

[22] E. A. Mashkovich, A. I. Shugurov, S. Ozawa, E. Estacio, M. Tani, and M. I. Bakunov, IEEE Transactions on Terahertz Science and Technology, **2015**, 5, 732.

[23] T. Skauli, P. S. Kuo, K. L. Vodopyanov, T. J. Pinguet, O. Levi, L. A. Eyres, J. S. Harris, M. M. Fejer, B. Gerard, L. Becouarn, and E. Lallier. J. Appl. Phys. **2003**, 94, 6447.

[24] F. Pan, G. Knöpfle, C. Bosshard, S. Follonier, R. Spreiter, M. S. Wong, and P. Günter, Appl. Phys. Lett. **1996**, 69, 13.

[25] M. Jazbinsek, U. Puc, A. Abina, and A. Zidansek, Applied Sciences, **2019**, 9, 882.

5.2 Additional comments

5.2.1 More about the gratings used in [83]

In this chapter paper, the grating we used is the second batch fabricated by Dr. Kashif Masud Awan. He also fabricated the first batch of the gratings on a 1 mm-thick GaP. Three different grating periods designed for perfect phase matching at 3 THz, 4 THz, and 5 THz were fabricated. Each grating has an area of 500 μm × 500 μm. The diffraction efficiency of the best spot on the grating optimizing the DFG phase matching at 3 THz gives a diffraction efficiency of approximately 20% into each of the 1st diffraction orders. The other two gratings' first-order diffraction efficiency is even lower. We focus the NIR generation beam onto the grating and carefully move the crystal with the 3D stage to find the best spot on the grating. We compared the THz spectrum generated with an unpatterned crystal and the crystals with grating, whose measured spectra are shown in Fig. 5.1. For the THz generated with 1 mm-thick unpatterned GaP, the THz spectrum peaks at 2 THz and the first phase-matching dip is at 4 THz.

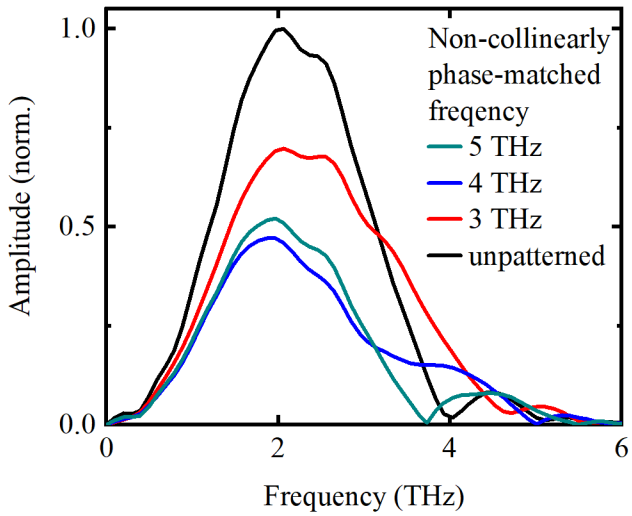

Fig. 5.1 The experimentally measured THz spectra for a 1 mm-thick GaP crystal and contact gratings optimized for THz generation at 3 THz, 4 THz, and 5 THz. The detection crystal is a 100 μm thick GaP.

The patterned crystals optimizing DFG phase matching at 3 THz and 4 THz also increase the spectral bandwidth compared to the THz spectrum generated by the unpatterned crystal. Notably, we can see some THz is generated at 4 THz, which cannot be generated by the 1 mm-thick unpatterned crystal due to the phase matching condition. However, for these two gratings, the frequency upshift effect is limited by their diffraction efficiency and defects in the grating that affect the THz generated by the 0^{th} diffraction order. The grating optimizing the DFG phase matching at 5 THz has not shown the effect of generating frequency components at 5 THz due to the low diffraction efficiency and it also suppresses the THz generation at low frequencies.

Although the diffraction efficiency of the first batch of gratings is not high enough to improve THz generation at higher frequencies, we can still use them to enhance the efficiency of the THz detection. The reason is that in the EOS detection technique, the modulation of the NIR detection beam induced by the THz beam is measured, or, in another word, the amount of change in NIR polarization due to the nonlinear interaction with a THz field. This means that as long as the detection beam is weak enough such that self-induced nonlinear effects, thereby changing the NIR polarization, are negligible, the polarization rotation induced by the THz field does not change with the power of the NIR gating beam.

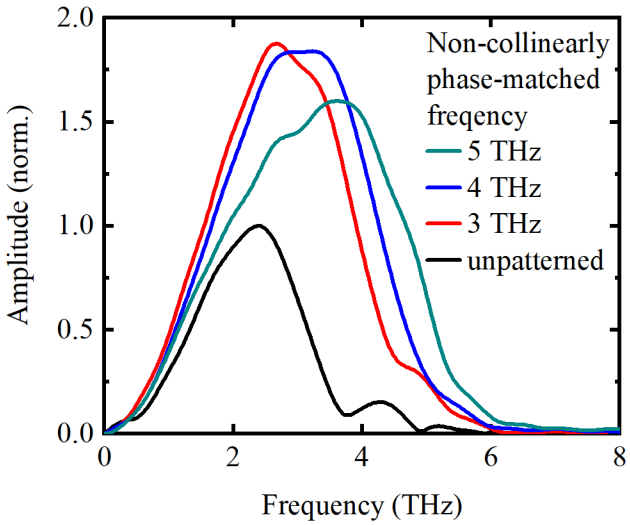

Fig. 5.2 The experimentally measured THz spectra for a 1 mm-thick GaP crystal and contact gratings optimized for THz detection at 3 THz, 4 THz, and 5 THz. (Adapted from [83])

The effect of the grating for THz detection is shown below, adapted from our work in 2019 [83]. The gratings enhance the THz detection efficiency above 2.5 THz. Gratings designed for optimizing THz detection at higher frequencies consistently extend the detection window towards higher frequencies. Note that even though the gratings optimized the THz detection at higher frequencies, the detection efficiency at low frequencies is not significantly affected. This could be partly explained by looking into the phase-matching factor of the difference frequency generation in the THz detection process. The phase-matching factor is defined as $f_{PM} = \frac{e^{i\Delta kL}-1}{i\Delta k}$, which is the term representing the effect of the phase matching in the solution to the coupled wave equations for DFG. Figure 5.3 plots the phase-matching factor for the DFG process for THz detection with 1 mm-thick crystal, 3 THz grating (Λ_1), 4 THz grating (Λ_2), and 5 THz grating (Λ_3).

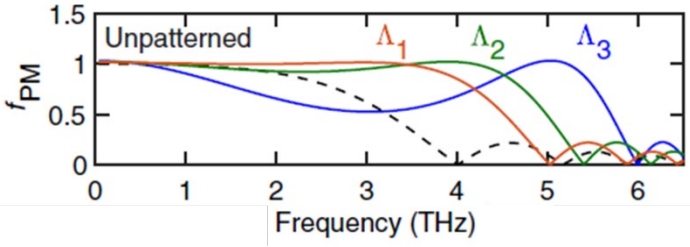

Fig. 5.3 The DFG phase-matching factor for calculated for 1 mm-thick GaP, gratings with periods $\Lambda_1 = 1.935\ \mu m$, $\Lambda_2 = 1.635\ \mu m$, $\Lambda_3 = 1.335\ \mu m$. (Adapted from [83])

Even though the gratings are designed to optimize the corresponding phase-matching at 3 THz, 4 THz and 5, THz, they do not significantly affect the phase matching at lower frequencies. Especially for Λ_1 and Λ_2 gratings, they optimize the phase matching almost over the whole spectral range. The other reason that the THz detection efficiency at low frequencies was not affected by the phase matching change is that there is a polarization filtering effect at the back surface at the GaP crystal which enhances the EOS detection efficiency in the whole THz bandwidth. This effect is thoroughly explained in [83] and the manuscript in this chapter.

5.2.2 About the dynamic range measurement of the THz-TDS

To describe the sensitivity of the THz time-domain spectroscopy, dynamic range is one of the most important metrics. There have been several different ways of defining the dynamic range of THz-TDS systems [85–87]. Generally, these definitions are dividing the peak signal amplitude/power by the amplitude/power of the spectral noise and taking the logarithm of this result. Calculating the dynamic range using the spectral power or amplitude is equivalent since their results always differ by a factor of 2. The main difference in these definitions of the dynamic range is how the spectral noise level is defined in a THz-TDS system. One way of defining the noise level is by taking the root-mean-square (RMS) value of the signal at frequencies where there is no real THz signal. One example of using this definition is shown in Fig. 5.4.

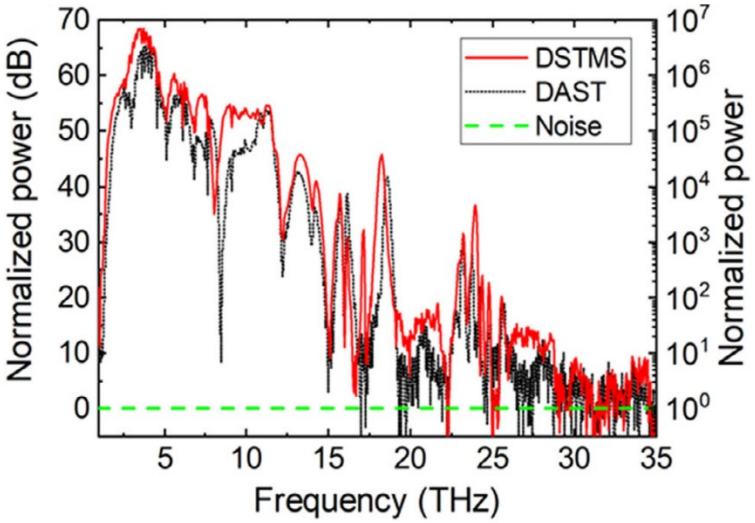

Fig. 5.4 THz power spectra of time-domain signals measured with a pair of DSTMS crystal and DAST crystals. Both these power spectra are normalized to the noise floor which is defined as the average of the signal power above 30 THz. This figure is taken from [87].

Another definition of the noise floor taken from [86] is the RMS value of the signal measured by blocking the THz beam while keeping the rest of the experimental setting the same. A typical example of this definition is shown in Fig. 5.5. In this figure, the THz spectral intensity and noise level are measured separately. The dynamic range of the system is calculated accordingly. We can also see a frequency dependence on the noise floor due to the 1/f noise in the system [86]. We take this second definition of the noise floor in this manuscript in this chapter. For the noise floor defined as the RMS value of the signal at frequencies where there is no THz, it contains the noise carried by the THz pulse itself. If the noise carried by the THz pulse is dominant in the system, it does not equal to the lowest signal that we can detect using this THz-TDS system. If we put an absorptive sample in the THz beamline of this THz-TDS

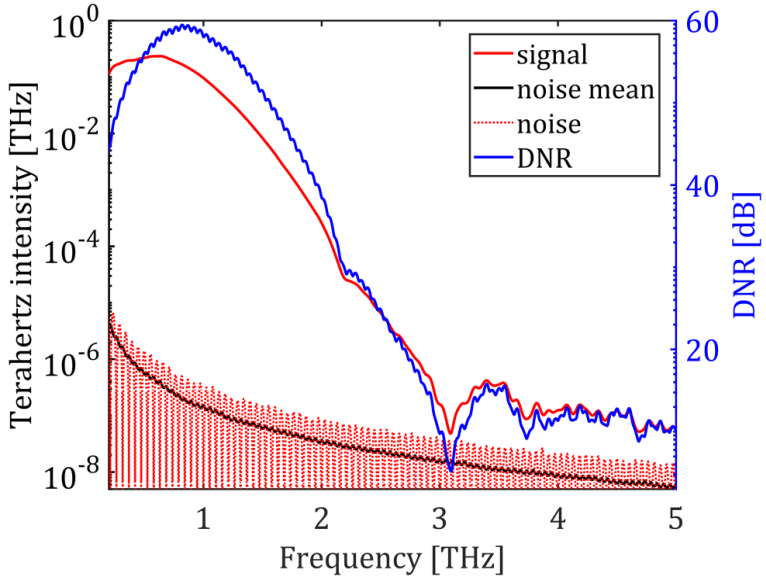

Fig. 5.5 THz spectral intensity (red solid line) compared to spectral noise intensity (dotted line). The black line is the smoothed noise floor. The blue line is the calculated dynamic range (DNR) in dB. Figure taken from [86].

system, which decreases the THz intensity incident on the detection crystal, then the noise level defined in the first definition in this subsection will also decrease as the noise carried by the THz pulse is also absorbed.

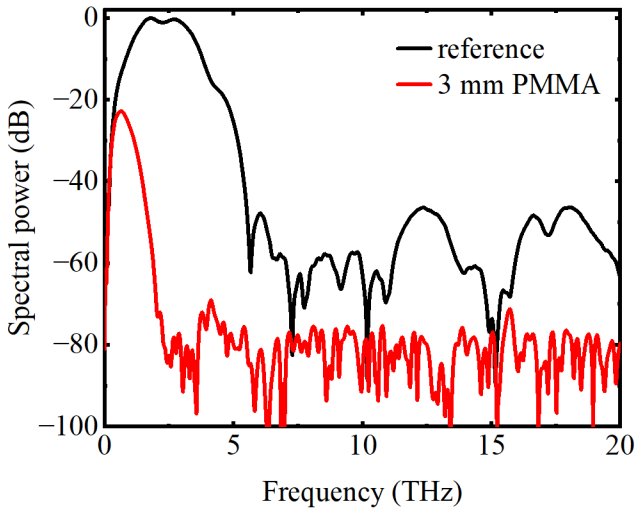

Fig. 5.6 THz spectra power measured when there is no sample in the dual grating assisted THz-TDS system (black) and when there is a 3 mm-thick PMMA is in the THz path (red). Spectra power normalized to the peak of the black curve.

Fig. 5.6 is an example of noise level at frequencies, where there is no THz signal, decreases when the THz signal is attenuated. In this plot, when there is no sample in the THz system, the noise level at frequencies where there is no THz signal is around -60 dB. After putting the 3 mm-thick PMMA into the system, the peak spectral power is attenuated to below -20 dB, and the noise level at frequency where there is no THz signal also decreases to -80 dB. Thus, we decided to use the noise purely from the gating beam as the noise level of the THz-TDS system.

Chapter 6

High-field THz source centered at 2.6 THz

6.1 Background and relevance

In the previous chapter, our work demonstrates for the first time the use of a contact grating on a semiconductor second-order nonlinear crystal to generate frequencies exceeding 2 THz. The next step is to boost the field strength in this THz system. In Chapters 4 and 5, we operate the Pharos laser at 1.1 MHz with a 0.9 μJ pulse energy and aim to achieve a high signal-to-noise ratio from the THz-TDS system. In this context, it is necessary to tightly focus our generation beam into the generation crystal, as the efficiency of the THz generation is proportional to the fluence of the NIR generation beam, assuming no saturation effect [43]. Furthermore, since the wavelength of the generated THz is larger than the spot size of the focused generation beam, the generated THz beam is close to a point source that can be easily collimated and subsequently refocused [88]. To generate high-field THz, it is imperative to increase the NIR generation beam fluence on the generation crystal. This is not feasible in a THz system where the generation beam is tightly focused into the generation crystal because the fluence will rapidly approach the damage threshold of the generation crystal. Higher NIR beam fluence also leads to pronounced saturation effects such as multi-photon absorption [46] and thermal effects [62]. An alternative approach involves using a collimated NIR beam for THz generation with an expanded beam size, provided there is sufficient NIR pulse energy. High-field THz generation using a collimated generation beam in a collimated system configuration has been demonstrated with different semiconductor crystals [64,88–90] and in organic crystals [91–93]. It is worth noting that the generation beam in the tilted-pulse-front THz generation technique incident into the $LiNbO_3$ crystal is also collimated. Additionally, the collimated

generation beam approach has been used for contact grating-assisted tilted-pulse-front high-field THz generation below 2 THz in ZnTe crystals [54].

In this chapter, we utilize a 1 mm-thick GaP crystal with a surface-etched phase grating to generate high-field THz with a peak exceeding 2 THz [23]. On this occasion, the grating is fabricated with a different Recipe by Dr. Mohammad Bashirpour [94]. To improve the uniformity of the grating across the whole area, we replace e-beam lithography with contact photolithography. Rather than drawing 20×20 gratings with an area of 500 μm × 500 μm using e-beam lithography, contact photolithography can produce a single 1 cm × 1 cm grating in one pass. The newly fabricated phase grating exhibits a diffraction efficiency of 43.5% in each of the $\pm 1^{st}$ diffraction orders while only 0.7% of the power was left in the 0^{th} order. This 43.5% diffraction efficiency surpasses the maximum theoretical value for a phase grating of 40.5%. This anomaly arises because the grating also functions as an anti-reflection structure, resulting in an increased transmission into the GaP crystals. This grating with high uniformity and diffraction efficiency facilitates the generation of high-field THz exceeding 2 THz using a collimated NIR generation beam.

Research Article | Vol. 31, No. 20 / 25 Sep 2023 / Optics Express 32468
Optics EXPRESS

High-field THz source centered at 2.6 THz

WEI CUI,[1] EESWAR KUMAR YALAVARTHI,[1] ASWIN VISHNU RADHAN,[1] MOHAMMAD BASHIRPOUR,[1] ANGELA GAMOURAS,[1,2] AND JEAN-MICHEL MÉNARD[1,2,*]

[1]University of Ottawa, Department of Physics, 25 Templeton Street, Ottawa, Ontario K1N 6N5, Canada
[2]National Research Council Canada, 1200 Montreal Road, Ottawa, Ontario K1A 0R6, Canada
*jean-michel.menard@uottawa.ca

Abstract: We demonstrate a table-top high-field terahertz (THz) source based on optical rectification of a collimated near-infrared pulse in gallium phosphide (GaP) to produce peak fields above 300 kV/cm with a spectrum centered at 2.6 THz. The experimental configuration, based on tilted-pulse-front phase matching, is implemented with a phase grating etched directly onto the front surface of the GaP crystal. Although the THz generation efficiency starts showing a saturation onset as the near-infrared pulse energy reaches 0.57 mJ, we can expect our configuration to yield THz peak fields up to 866 kV/cm when a 5 mJ generation NIR pulse is used. This work paves the way towards broadband, high-field THz sources able to access a new class of THz coherent control and nonlinear phenomena driven at frequencies above 2 THz.

1. Introduction

High-field terahertz (THz) sources [1] are widely applied to explore nonlinear THz properties of various materials including semiconductors [2], 2D materials [3], and gases [4]. These sources also allow experimentalists to access new regimes of high-harmonic generation [5], free electron acceleration [6], and coherent control [7–9]. Most research groups working on these topics have employed the tilted-pulse-front technique based on an ultrafast near-infrared (NIR) laser to generate high-field THz pulses by optical rectification inside a $LiNbO_3$ nonlinear crystal [10,11]. Generally, this table-top technique provides a THz electric field on the order of several hundreds of kV/cm, with a record value of 6.3 MV/cm [12], featuring a spectrum which peaks around 1 THz and then gradually decreases in amplitude as frequencies approach the phonon resonance of $LiNbO_3$ at 4.5 THz [13,14]. Modifications to this standard configuration have recently led to a more efficient generation of high-field THz pulses with spectral components up to 4 THz [15]. However, 98% of the pulse energy in this configuration is still contained within the frequency range below 2 THz, limiting most high-field applications requiring a spectrum centered at higher frequencies. Cooling the $LiNbO_3$ crystal down to cryogenic temperatures can increase the field strength by a factor up to 2.7 [16,17] and, in some cases, extend the spectrum towards higher frequencies by reducing losses due to the phonon absorption tail. This latter approach was notably used to enable the generation of a spectrum centered at 4 THz with a peak field around 10 kV/cm [16]. However, the use of cryogenic equipment adds another level of complexity to an already complicated experimental setup. Furthermore, a THz peak field evaluated to about 150 kV/cm from power measurements was produced in a 1 mm-thick GaP crystal with a spectral peak below 2 THz [18]. There is therefore a general lack of a straightforward table-top experimental configuration based on high damage threshold crystals, able to generate high-field THz pulses with a spectrum centered at frequencies exceeding 2 THz. Such a system is crucial for providing experimentalists with access to a new range of phenomena such as phonon-assisted nonlinearities [2,19], coherent control of Bose-Einstein condensation in semiconductor microcavities [20], and saturable transitions in molecular gases [4]. Other high-field THz generation techniques using air plasma or metallic spintronic emitters have reported peak fields above 1 MV/cm [21–24],

#496855 https://doi.org/10.1364/OE.496855
Journal © 2023 Received 31 May 2023; revised 29 Aug 2023; accepted 29 Aug 2023; published 14 Sep 2023

Optics EXPRESS

the spectral bandwidth of these sources typically extends from 0.5 to 30 THz. Recent work on air plasma THz sources have demonstrated high-energy pulses covering a large spectral range [24,25]. Such systems, if combined with spectral filters [26], can potentially yield THz pulses with peak field amplitudes reaching several 100's of kV/cm within a specific spectral region. Finally, organic materials, such as DAST and DSTMS, display great potential for generating high-field THz above 20 THz [27–29]. High conversion efficiencies in the region between 2 and 4 THz [30–32] can notably be achieved with a pump source centered between 1.2 and 1.6 μm, relying on a nonlinear wavelength conversion stage [33]. BNA and HMQ-TMS crystals can generate high-field THz up to 6 THz with a NIR pump laser centered at 800 nm or 1030 nm, however most of the THz pulse energy is still contained within a spectral range below 2 THz [34,35]. In those spectra, phonon absorption lines are common due to the organic nature of the THz generation crystal, but those lines can be reduced with cryogenic cooling [30,35,36]. The typical damage threshold of organic crystal is however relatively low, typically below 20 mJ/cm^2 [35,37,38], which is about 60 times lower than that of semiconductor crystals, such as GaP [39,40]. This may be a limiting factor for long-term stability of a THz source relying on high near-infrared power.

In this work, we demonstrate a scheme to generate high-field THz pulses centered at 2.6 THz using a phase grating directly etched onto the surface of a nonlinear crystal to enable non-collinear phase-matched tilted-pulse-front THz generation. This technique has been proposed theoretically [41–47] and then demonstrated experimentally [48–50] with surface gratings on ZnTe and $LiNbO_3$ crystals to achieve high THz generation efficiencies at frequencies <2 THz. In comparison to the standard tilted-pulse-front technique in $LiNbO_3$, this configuration eliminates imaging distortions of the diffracted generation pulse, hence improving THz beam quality as well as THz generation efficiency [41,44,48]. Recently, broadband THz generation was demonstrated from 0.1 to 6 THz with a phase grating etched on the surface of a 2 mm-thick GaP crystal [50]. In this geometry the generation NIR pulse was focused onto the generation crystal. Here we use the same material, but we rely instead on a different geometry using a collimated 0.57 mJ NIR pulse from a standard commercial 1035 nm femtosecond laser amplifier to generate a THz pulse with a peak field reaching 303 kV/cm at a central frequency of 2.6 THz. This is the first report of a high-field source based on a high damage threshold crystal to target the hard-to-access region immediately above 2 THz. The confined spectral bandwidth, free of phonon absorption lines, can be efficiently used to drive a resonant system into a nonlinear regime. More importantly, there are two indications that our configuration is able to yield much larger THz peak fields: (1) NIR pulse energies to generate THz radiation can be increased by two orders of magnitude before reaching the GaP damage threshold, and (2) we observe a quasi-linear relationship between the incident NIR pulse energy and the emitted THz amplitude, with a slight saturation onset only observed at the highest energies reached in our experiments.

2. Experiments

Figure 1 shows a diagram of the experiment apparatus for high-field THz generation in a GaP crystal. This crystal is patterned with a surface phase grating to efficiently diffract the incident NIR beam and enable tilted-pulse front phase-matching conditions [10,51]. The optical source is a commercial Yb:KGW regenerative amplifier system generating 265 fs pulses with a center wavelength of 1035 nm, a pulse energy of 1 mJ and a repetition rate of 3 kHz. The output laser beam is focused in air with a 1 m focal length lens. A 1 mm-thick BK7 window is placed before the focus to broaden the NIR spectrum from a bandwidth of 3.5 THz to 7.2 THz through self-phase modulation (SPM). The NIR spectra of the pulse before and after the BK7 window are shown in Fig. 1(a). The laser beam is then guided through a set of chirped mirrors, providing a total dispersion of -3000 fs^2, to compensate for the positive dispersion in the SPM process and

Optics EXPRESS

compress the pulse to ~80 fs (FWHM) in the time domain. The autocorrelation traces of the NIR pulses before and after the BK7 window and chirped mirrors are shown in Fig. 1(b).

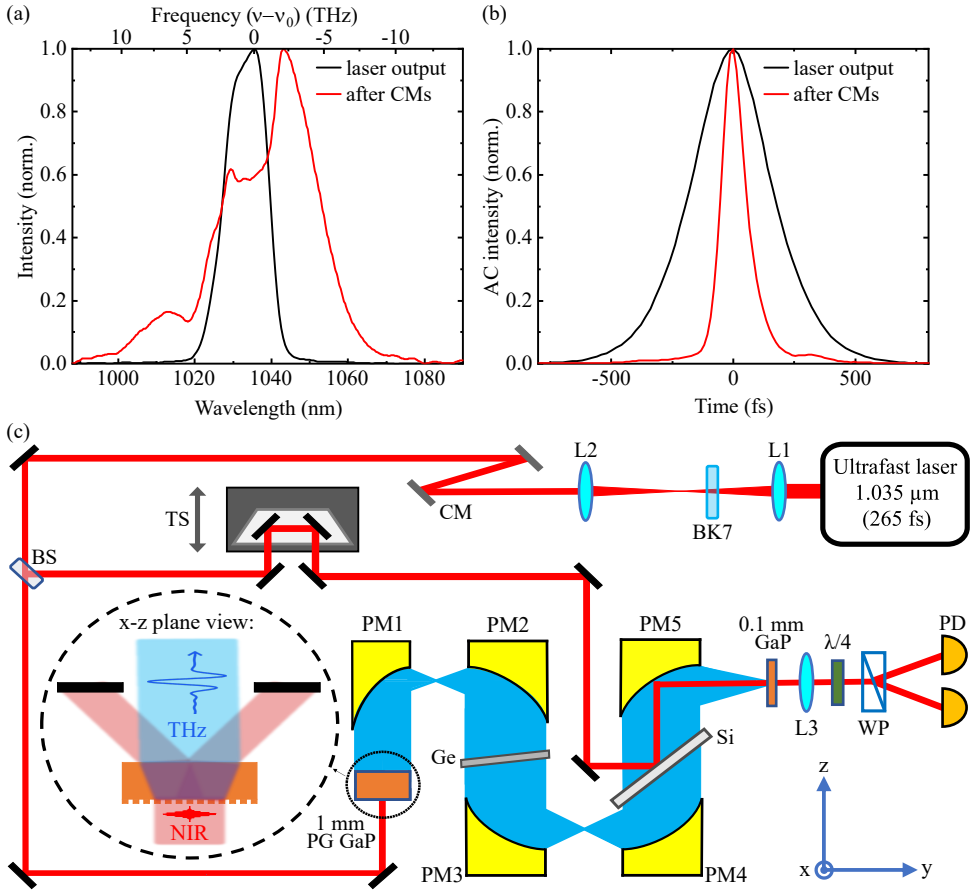

Fig. 1. (a) and (b) Spectra and corresponding autocorrelation traces of the NIR laser pulses measured at the laser output (black line) and after spectral broadening in BK7 and temporal compression with chirped mirrors (CMs) (red line). We observe a spectral broadening from 3.5 THz to 7.2 THz (FWHM) and a reduced pulse duration from 265 fs to 81 fs (FWHM). The reference frequency ν_0 corresponds to the center wavelength of 1035 nm. (c) Schematic of the high-field THz setup. The focused NIR pulses are first passed through a 1 mm-thick BK7 window to broaden the spectrum by self-phase modulation. A THz-TDS scheme is then used to generate and detect THz radiation where the NIR generation beam is collimated onto the THz generation crystal. The germanium wafer (Ge) can be used to block the small (1.4%) residual fundamental NIR beam. The system is operated in a dry-air purged environment. Optical components to build the setup are labelled above as follows: L1: lens, f = 100 cm; L2: lens, f = 70 cm; CMs: -250 fs^2 each; BS: beamsplitter; TS: translation stage; PG on 1 mm GaP: 110-oriented 1 mm-thick GaP crystal with a phase grating on the incident surface; Si: silicon wafer; PM: Parabolic mirror; 0.1 mm GaP: 110-oriented 0.1 mm-thick GaP crystal; L3: lens, f = 5 cm; λ/4: quarter-wave plate; WP: Wollaston prism; PD: photodetector.

The NIR beam in the first arm is collimated at normal incidence onto a 1 mm-thick 110-oriented GaP semiconductor crystal with a surface-etched phase grating [52] to enable efficient THz

Optics EXPRESS

generation by optical rectification.This NIR beam has a $1/e^2$ diameter of 3.2 mm and a pulse energy of 0.57 mJ. The highly uniform grating with an average pitch of $\Lambda = 1.60$ µm yields first diffraction orders at angles of ±12° inside the GaP crystal. The standard deviation of this average grating pitch is measured to be ±0.03 µm. This configuration enables non-collinear phase-matching conditions leading to broadband THz generation from 0.5 to 6 THz with a geometry allowing both the incident NIR pulses and generated THz pulses to propagate along a direction normal to the crystal plane. In this geometry, the 1st order diffraction angle of the NIR pulse is also equal to its pulse-front-tilt angle [42]:

$$\theta_{tilt} = cos^{-1}\frac{n_g(\omega_{NIR})}{n(\omega_{4THz})}, \tag{1}$$

where $n_g(\omega_{NIR})$ is the group index of the NIR generation beam centered at 1035 nm and $n(\omega_{4THz})$ is the phase index at 4 THz inside of the generation crystal. The grating filling ratio is 50%, and the target height modulation is 245 nm. This corresponds to an optical π-phase difference between optical light rays passing through the top and bottom sections of the grating, which reduces the 0th diffraction order because of destructive interference. In a transmission geometry, we measure a total of 44% of the incident power (87% of the total transmitted NIR power) in ±1 diffraction orders, while only 0.7% of the incident power (1.4% of the transmitted power) remains in the 0th diffraction order. Note that the presence of the grating also creates an effective index layer at the air-GaP interface reducing the Fresnel reflection coefficient by about 5% at the front crystal surface [52,53]. The presence of the grating on a 1 mm-thick GaP crystal increases the energy contained in the region between 2 and 3 THz by a factor of 4. The generated THz radiation is collected by an off-axis gold parabolic mirror PM1 in Fig. 1(c) with 1.27 cm diameter and a short (1.27 cm) focal length to minimize the spot size at the focus. The ±1st diffracted NIR beams leave the generation crystal with an exiting angle of 40°. Since these beams are not collected by PM1, this allows a sample to be positioned at the first THz focus to perform high-field experiments while the NIR background illumination remains relatively weak. In the same figure, the subsequent parabolic mirrors, with a 5.08 cm diameter and 5.08 cm focal length (PM2-PM5), are arranged in a standard terahertz time-domain spectroscopy (THz-TDS) configuration. The gating pulse in the second arm is first reflected by the Si wafer and then focused by the PM5 on a 0.1 mm-thick 110-oriented GaP detection crystal, overlapped with the focused THz transient to resolve the oscillating THz transient with electro-optical sampling (EOS) detection. The thin GaP detection crystal enables a broad detection bandwidth >6 THz.

3. Results and discussion

Figure 2 shows the measured high-field THz transient and corresponding spectral amplitude, obtained with the Fourier transform. The spectral bandwidth extends up to 6.3 THz with a peak centered at 2.6 THz. The multi-cycle pulse is attributed to group velocity dispersion in the 1 mm-thick GaP generation crystal stretching the pulse in time. We evaluate the electric field strength of the THz pulse at the focus between PM1 and PM2 since this is a practical position to insert a sample in the setup. We evaluate the THz electric field E_{THz} with the following equation [54]:

$$E_{THz} = \frac{A-B}{A+B}\frac{\lambda_{gat}K_{gat}}{2\pi r_{41}n_0^3 L t_{tot}}, \tag{2}$$

where A and B are the voltages on the PDs, λ_{gat} is the central wavelength of the NIR gating beam (1035 nm), $r_{41} = 1$ pm/V is the electro-optical coefficient of GaP at 1035 nm [55], n_0 is the refractive index of the GaP at 1035 nm [56], $L = 0.1$ mm is the thickness of the GaP detection crystal, t_{tot} is the transmission coefficient taking into account the THz transmission through the GaP detection crystal, the Ge wafer and the Si wafer after PM4 considering the index of refraction

Optics EXPRESS

of these material at 2.6 THz [57–59]. Finally, the damping factor $K_{gat} = E^{original}_{THz,max}/E^{measured}_{THz,max} = 1.46$ describes the "smooth effect" in the EOS from a non-infinitely short gating pulse [60]. Considering this geometry, we obtain a peak field of 303 kV/cm at the focus of PM1.

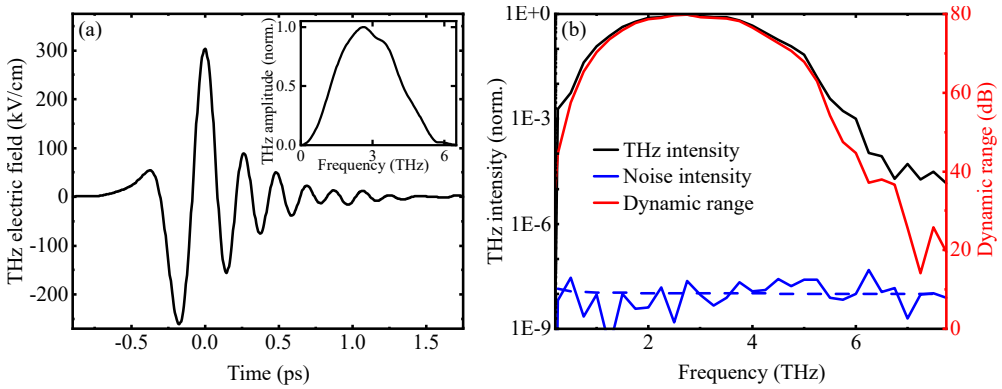

Fig. 2. (a) Time-resolved high-field THz transient. The inset shows the corresponding spectral amplitude calculated with the Fourier transform. (b) THz spectral intensity (black curve) and noise floor (blue curve). The dashed blue line is the noise floor fitted with the model $A^*(1/f + B)$, considering the $1/f$ noise, where f is the frequency and both A and B are fitting parameters. The dynamic range (red curve) is calculated based on [61].

The dynamic range of our system reaches 80 dB at 2.6 THz and remains above 60 dB between 0.6 THz to 5.3 THz (Fig. 2(b)). We do not expect THz radiation to be generated at frequencies exceeding the range shown in Fig. 2(b) due to a drop in the second order nonlinear coefficient at 8 THz and a phonon absorption at 11 THz [62].This figure of merit is calculated by dividing the THz spectral intensity by the noise floor, which is measured by blocking the THz beam and then fitted to a model $A^*(1/f + B)$, where f is the frequency, and A and B are fitting parameters [61].

To confirm the THz field strength, we also measure the THz power with a thermal detector. A Golay cell, calibrated using a blackbody source, measures a power corresponding to a THz pulse energy of 2.8 nJ immediately after the detection crystal since the space after PM1 in our setup is too small to accommodate the Golay cell or a mirror able to deflect the beam. Considering the Fresnel transmission coefficients of all optical components between the Golay cell placed after the GaP detection crystal and THz focus located between PM1 and PM2, the pulse energy at that position corresponds to 41.1 nJ. Based on this value, the conversion efficiency from the diffracted NIR beam to THz radiation is relatively low (0.023%), but could be improved with an anti-reflection coating and an optimized grating design [63]. We then calculate the peak THz field strength based on this Golay cell measurement. First, we use the time-resolved THz transient and consider the highest THz half cycle containing 45% of the full pulse energy to extract a precise value of the THz peak electric field [60]. The peak intensity of the highest THz half cycle can be calculated by

$$I_{THz,\,peak} = \frac{2\,\mathcal{E}_{THz}}{\pi\,(w_{1/e^2})^2\,\tau_{THz,peak}}, \tag{3}$$

where $\mathcal{E}_{THz}$ is the THz pulse energy contained within the highest THz half cycle, w_{1/e^2} is the $1/e^2$ radius of the THz beam (160 μm) measured using the knife-edge method, and $\tau_{THz,peak}$ is the FWHM time duration of the peak half cycle (87 fs) of the THz intensity waveform. The peak

Optics EXPRESS

THz electric field is then given by:

$$E_{THz} = \sqrt{\frac{I_{THz,peak}}{\varepsilon_0 c}}, \tag{4}$$

where ε_0 is the vacuum permittivity and c is the speed of light in vacuum. We obtain a peak field of 446 kV/cm, which is 1.5 times higher than the value obtained using the EOS data and Eq. (2). This discrepancy between different measurement techniques is well known [64] and has also been observed in other work [54]. In this work, we mainly refer to the THz peak field calculated from the EOS measurement and Eq. (2), since it is a more traceable value than the value measured with the Golay cell.

Finally, we look into the possibility to combine our configuration with a more powerful NIR source to achieve even higher THz peak fields. We first determine the crystal damage threshold to the incident NIR pulse, which is a critical parameter to allow the use of higher pulse energies. We perform this test at a wavelength of 1035 nm and a repetition rate of 50 kHz by placing a non-patterned and patterned GaP window at the focus of a 15 cm lens. For both samples, we only notice visible damage on the crystal accompanied by an abrupt drop in the generated THz signal when the incident power exceeds 0.8 W, which corresponds to a peak fluence of 5.6 J/cm^2. For comparison purposes, the highest peak fluence used in this work is 14.2 mJ/cm^2, which is a factor of 400 lower than this damage threshold. These results indicate that it is indeed possible to significantly increase the incident NIR pulse energy to enable the generation of higher THz peak fields. We also investigate the dependence of the THz peak field E_{THz}^{Peak} as a function of the NIR generation peak fluence F_{NIR}. Figure 3(a) shows the THz signal as F_{NIR} is varied from 1.5 mJ/cm^2 to 14.2 mJ/cm^2 while keeping the same NIR spot size on the generation crystal. The experimental results are displayed along with two simple models: (1) a linear relationship (red dashed line) fitting the data collected at low fluence <5.1 mJ/cm^2: $E_{THz}^{Peak} = aF_{NIR}$, where the slope $a = 27.5$ kV cm mJ^{-1} is related to the conversion efficiency, and (2) a modification of the first model (blue dashed curve): $E_{THz}^{Peak} = aF_{NIR} / (1 + bF_{NIR})$, where a is the same as that in the first model, and $b = 0.024$ mJ^{-1} cm^2 accounts for saturation effects, which can be caused by multiple-photon absorption [10] and thermal effects [65]. We observe that the generated

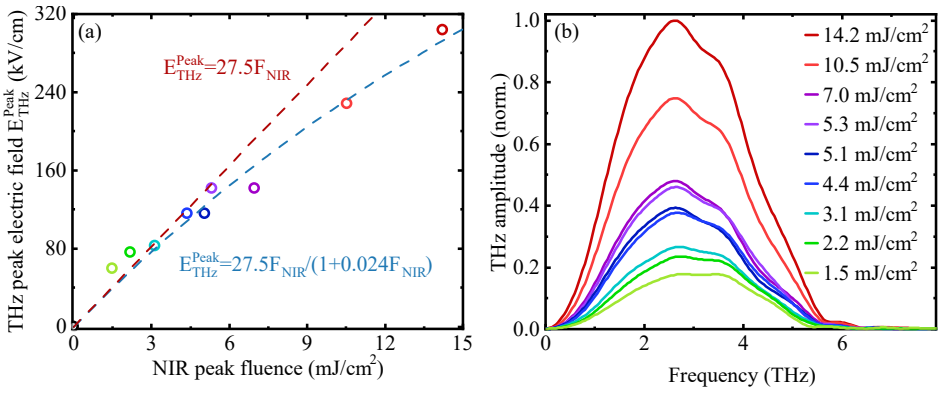

Fig. 3. (a) Measured THz peak electric field E_{THz}^{Peak} strength versus NIR peak fluence F_{NIR}. The red dashed line is a linear fit while the blue dashed line corresponds to a saturation model: $aF_{NIR} / (1 + bF_{NIR})$, where both a and b are fitting parameters. (b) Corresponding THz spectra measured with NIR generation pulses with different NIR peak fluence. We normalize these measurements to the maximum amplitude obtained with a 14.2 mJ/cm^2 NIR peak fluence.

Optics EXPRESS

THz peak amplitude is linear with F_{NIR} until 5.1 mJ/cm^2. The observation of a saturation onset at this NIR fluence is consistent with previous work using an unpatterned GaP crystal [66]. Figure 3(b) shows THz spectra generated with different NIR incident pulse energies, which all peak at 2.6 THz. However, we observe a gradual decrease of the THz spectral amplitude around 3.5 THz as F_{NIR} increases from 1.5 mJ/cm^2 to 4.4 mJ/cm^2. Similar THz spectral changes at high F_{NIR} have also been observed previously [67], but further investigation is still required to fully understand this effect. Considering our saturation model and the fact that F_{NIR} can be significantly increased without inducing damage to the crystal, we can anticipate that a NIR peak fluence of 124 mJ/cm^2, corresponding to a NIR pulse energy of 5 mJ with the same beam size, will produce a THz peak field of 866 kV/cm with a spectrum also centered at 2.6 THz.

4. Conclusion

We demonstrate a high-field THz system using collimated NIR pulses impinging on a GaP crystal with a surface phase grating to generate pulses with 303 kV/cm peak field centered at 2.6 THz. This peak field is confirmed by measurements performed with a calibrated Golay cell. We also show that our system operates significantly below the GaP damage threshold and close to a linear regime, allowing more powerful NIR sources to produce even higher peak fields approaching 1 MV/cm. Note that increasing the NIR beam size on the generation crystal allows the use of higher pulse energies without damaging the crystal, hence resulting in larger THz powers. A laser source at a longer wavelength could also be used to reduce the multi-photon absorption processes in GaP, which may help to reduce saturation effects observed in the THz generation process as well as increase the crystal damage threshold. Considering a tilted-pulse-front configuration with an optimal grating design, this latter approach could, according to numerical models, produce peak fields reaching up to 17 MV/cm at a central frequency of 3 THz [47]. Finally, although our experiment focuses exclusively on GaP as the THz generation crystal, the same optical configuration could be used to generate high-field THz in other materials with a surface phase grating to gain access to different spectral ranges or to increase THz generation efficiencies. This work will pave the way towards a new class of high-field THz sources able to access a spectral range departing from the conventional region below 2 THz and will enable novel nonlinear and coherent control experiments in condensed matter systems.

Funding. Ontario Ministry of Colleges and Universities (ER21-16-206); National Research Council Canada (HTSN-702, JCEP); Natural Sciences and Engineering Research Council of Canada (RGPIN-2016-04797, RGPIN-2023-05365); Canada Foundation for Innovation (Project Number 35269).

Acknowledgments. We thank R. Huber for helpful discussions. This work was supported by the High Throughput and Secure Networks Challenge Program at the National Research Council of Canada (HTSN-702), the NSERC Discovery funding program (RGPIN-2016-04797, RGPIN-2023-05365), the Canada Foundation for Innovation (CFI) (Project Number 35269), the Ontario Ministry of Colleges and Universities' Early Researcher Award (ER21-16-206) and the National Research Council of Canada via the Joint Centre for Extreme Photonics (JCEP).

Disclosures. The authors declare no conflicts of interest.

Data availability. Data underlying the results presented in this paper are not publicly available at this time but may be obtained from the authors upon reasonable request.

References

1. J. A. Fülöp, S. Tzortzakis, and T. Kampfrath, "Laser-Driven Strong-Field Terahertz Sources," Adv. Opt. Mater. **8**(3), 1900681 (2020).
2. Y. Lu, Q. Zhang, Q. Wu, Z. Chen, X. Liu, and J. Xu, "Giant enhancement of THz-frequency optical nonlinearity by phonon polariton in ionic crystals," Nat. Commun. **12**(1), 3183 (2021).
3. I. Katayama, H. Aoki, J. Takeda, H. Shimosato, M. Ashida, R. Kinjo, I. Kawayama, M. Tonouchi, M. Nagai, and K. Tanaka, "Ferroelectric Soft Mode in a $SrTiO_3$ Thin Film Impulsively Driven to the Anharmonic Regime Using Intense Picosecond Terahertz Pulses," Phys. Rev. Lett. **108**(9), 097401 (2012).
4. P. Rasekh, A. Safari, M. Yildirim, R. Bhardwaj, J.-M. Ménard, K. Dolgaleva, and R. W. Boyd, "Terahertz Nonlinear Spectroscopy of Water Vapor," ACS Photonics **8**(6), 1683–1688 (2021).

Optics EXPRESS

5. B. Cheng, N. Kanda, T. N. Ikeda, T. Matsuda, P. Xia, T. Schumann, S. Stemmer, J. Itatani, N. P. Armitage, and R. Matsunaga, "Efficient Terahertz Harmonic Generation with Coherent Acceleration of Electrons in the Dirac Semimetal Cd_3As_2," Phys. Rev. Lett. **124**(11), 117402 (2020).
6. Z. Tibai, M. Unferdorben, S. Turnár, A. Sharma, J. A. Fülöp, G. Almási, and J. Hebling, "Relativistic electron acceleration by focused THz pulses," J. Phys. B At. Mol. Opt. Phys. **51**(13), 134004 (2018).
7. S. Schlauderer, C. Lange, S. Baierl, T. Ebnet, C. P. Schmid, D. C. Valovcin, A. K. Zvezdin, A. V. Kimel, R. V. Mikhaylovskiy, and R. Huber, "Temporal and spectral fingerprints of ultrafast all-coherent spin switching," Nature **569**(7756), 383–387 (2019).
8. X. Li, T. Qiu, J. Zhang, E. Baldini, J. Lu, A. M. Rappe, and K. A. Nelson, "Terahertz field–induced ferroelectricity in quantum paraelectric $SrTiO_3$," Science **364**(6445), 1079–1082 (2019).
9. K. Iwaszczuk, M. Zalkovskij, A. C. Strikwerda, and P. U. Jepsen, "Nitrogen plasma formation through terahertz-induced ultrafast electron field emission," Optica **2**(2), 116–123 (2015).
10. J. Hebling, K.-L. Yeh, M. C. Hoffmann, B. Bartal, and K. A. Nelson, "Generation of high-power terahertz pulses by tilted-pulse-front excitation and their application possibilities," J. Opt. Soc. Am. B **25**(7), B6 (2008).
11. H. Hirori, A. Doi, F. Blanchard, and K. Tanaka, "Single-cycle terahertz pulses with amplitudes exceeding 1 MV/cm generated by optical rectification in $LiNbO_3$," Appl. Phys. Lett. **98**(9), 091106 (2011).
12. B. Zhang, Z. Ma, J. Ma, X. Wu, C. Ouyang, D. Kong, T. Hong, X. Wang, P. Yang, L. Chen, Y. Li, and J. Zhang, "1.4-mJ High Energy Terahertz Radiation from Lithium Niobates," Laser Photonics Rev. **15**(3), 2000295 (2021).
13. N. V. Sidorov, M. N. Palatnikov, V. S. Gorelik, and P. P. Sverbil, "Second-order Raman spectra of a $LiNbO_3$:Tb crystal," Spectrochim. Acta, Part A **266**, 120445 (2022).
14. S. Kojima, "Broadband Terahertz Spectroscopy of Phonon-Polariton Dispersion in Ferroelectrics," Photonics **5**(4), 55 (2018).
15. L. Guiramand, J. E. Nkeck, X. Ropagnol, X. Ropagnol, T. Ozaki, and F. Blanchard, "Near-optimal intense and powerful terahertz source by optical rectification in lithium niobate crystal," Photonics Res. **10**(2), 340–346 (2022).
16. J. Hebling, A. G. Stepanov, G. Almási, B. Bartal, and J. Kuhl, "Tunable THz pulse generation by optical rectification of ultrashort laser pulses with tilted pulse fronts," Appl. Phys. B: Lasers Opt. **78**(5), 593–599 (2004).
17. T. Kroh, T. Rohwer, D. Zhang, U. Demirbas, H. Cankaya, M. Hemmer, Y. Hua, L. E. Zapata, M. Pergament, F. X. Kärtner, and N. H. Matlis, "Parameter sensitivities in tilted-pulse-front based terahertz setups and their implications for high-energy terahertz source design and optimization," Opt. Express **30**(14), 24186 (2022).
18. N. Nilforoushan, T. Apretna, C. Song, T. Boulier, J. Tignon, S. Dhillon, M. Hanna, and J. Mangeney, "Ultra-broadband THz pulses with electric field amplitude exceeding 100 kV/cm at a 200 kHz repetition rate," Opt. Express **30**(9), 15556–15565 (2022).
19. P. Rasekh, M. Saliminabi, M. Yildirim, R. W. Boyd, J.-M. Ménard, and K. Dolgaleva, "Propagation of broadband THz pulses: effects of dispersion, diffraction and time-varying nonlinear refraction," Opt. Express **28**(3), 3237–3248 (2020).
20. J.-M. Ménard, C. Poellmann, M. Porer, U. Leierseder, E. Galopin, A. Lemaître, A. Amo, J. Bloch, and R. Huber, "Revealing the dark side of a bright exciton–polariton condensate," Nat. Commun. **5**(1), 4648 (2014).
21. J. Dai, J. Liu, and X.-C. Zhang, "Terahertz Wave Air Photonics: Terahertz Wave Generation and Detection with Laser-Induced Gas Plasma," IEEE J. Sel. Top. Quantum Electron. **17**(1), 183–190 (2011).
22. A. D. Koulouklidis, C. Gollner, V. Shumakova, V. Y. Fedorov, A. Pugžlys, A. Baltuška, and S. Tzortzakis, "Observation of extremely efficient terahertz generation from mid-infrared two-color laser filaments," Nat. Commun. **11**(1), 292 (2020).
23. T. Seifert, S. Jaiswal, and U. Martens, *et al.*, "Efficient metallic spintronic emitters of ultrabroadband terahertz radiation," Nat. Photonics **10**(7), 483–488 (2016).
24. J. Buldt, H. Stark, M. Müller, C. Grebing, C. Jauregui, and J. Limpert, "Gas-plasma-based generation of broadband terahertz radiation with 640 mW average power," Opt. Lett. **46**(20), 5256–5259 (2021).
25. J. Buldt, M. Mueller, H. Stark, C. Jauregui, and J. Limpert, "Fiber laser-driven gas plasma-based generation of THz radiation with 50-mW average power," Appl. Phys. B **126**(1), 2 (2020).
26. A. Maleki, A. Singh, A. Jaber, W. Cui, Y. Xin, B. T. Sullivan, R. W. Boyd, and J.-M. Ménard, "Metamaterial-based octave-wide terahertz bandpass filters," Photonics Res. **11**(4), 526–532 (2023).
27. P. Y. Han, M. Tani, F. Pan, and X.-C. Zhang, "Use of the organic crystal DAST for terahertz beam applications," Opt. Lett. **25**(9), 675–677 (2000).
28. M. Jazbinsek, U. Puc, A. Abina, and A. Zidansek, "Organic Crystals for THz Photonics," Appl. Sci. **9**(5), 882 (2019).
29. U. Puc, T. Bach, P. Günter, M. Zgonik, and M. Jazbinsek, "Ultra-Broadband and High-Dynamic-Range THz Time-Domain Spectroscopy System Based on Organic Crystal Emitter and Detector in Transmission and Reflection Geometry," Adv. Photonics Res. **2**(4), 2000098 (2021).
30. C. P. Hauri, C. Ruchert, C. Vicario, and F. Ardana, "Strong-field single-cycle THz pulses generated in an organic crystal," Appl. Phys. Lett. **99**(16), 161116 (2011).
31. C. Vicario, C. Ruchert, and C. P. Hauri, "High field broadband THz generation in organic materials," J. Mod. Opt. **62**(18), 1480–1485 (2015).
32. C. Vicario, B. Monoszlai, and C. P. Hauri, "GV/m Single-Cycle Terahertz Fields from a Laser-Driven Large-Size Partitioned Organic Crystal," Phys. Rev. Lett. **112**(21), 213901 (2014).

Optics EXPRESS

33. S. S. Dhillon, M. S. Vitiello, and E. H. Linfield, *et al.*, "The 2017 terahertz science and technology roadmap," J. Phys. Appl. Phys. **50**(4), 043001 (2017).
34. A. Rovere, Y.-G. Jeong, R. Piccoli, S.-H. Lee, S.-C. Lee, O.-P. Kwon, M. Jazbinsek, R. Morandotti, and L. Razzari, "Generation of high-field terahertz pulses in an HMQ-TMS organic crystal pumped by an ytterbium laser at 1030 nm," Opt. Express **26**(3), 2509–2516 (2018).
35. Z. B. Zaccardi, I. C. Tangen, G. A. Valdivia-Berroeta, C. B. Bahr, K. C. Kenney, C. Rader, M. J. Lutz, B. P. Hunter, D. J. Michaelis, and J. A. Johnson, "Enabling high-power, broadband THz generation with 800-nm pump wavelength," Opt. Express **29**(23), 38084 (2021).
36. C. Vicario, B. Monoszlai, M. Jazbinsek, S.-H. Lee, O.-P. Kwon, and C. P. Hauri, "Intense, carrier frequency and bandwidth tunable quasi single-cycle pulses from an organic emitter covering the Terahertz frequency gap," Sci. Rep. **5**(1), 14394 (2015).
37. T. O. Buchmann, E. J. Railton Kelleher, M. Jazbinsek, B. Zhou, J.-H. Seok, O.-P. Kwon, F. Rotermund, and P. U. Jepsen, "High-power few-cycle THz generation at MHz repetition rates in an organic crystal," APL Photonics **5**(10), 106103 (2020).
38. B. Monoszlai, C. Vicario, M. Jazbinsek, and C. P. Hauri, "High-energy terahertz pulses from organic crystals: DAST and DSTMS pumped at Ti:sapphire wavelength," Opt. Lett. **38**(23), 5106–5109 (2013).
39. H. Lee, "Picosecond mid-IR laser induced surface damage on Gallium Phosphate (GaP) and Calcium Fluoride (CaF_2)," J. Mech. Sci. Technol. **21**(7), 1077–1082 (2007).
40. L. P. Gonzalez, S. Guha, and S. Trivedi, "Damage thresholds and nonlinear optical performance of GaP," in *Conference on Lasers and Electro-Optics, 2004*. (CLEO). (2004), Vol. 1, p. 2.
41. L. Pálfalvi, J. A. Fülöp, G. Almási, and J. Hebling, "Novel setups for extremely high power single-cycle terahertz pulse generation by optical rectification," Appl. Phys. Lett. **92**(17), 171107 (2008).
42. K. Nagashima and A. Kosuge, "Design of Rectangular Transmission Gratings Fabricated in $LiNbO_3$ for High-Power Terahertz-Wave Generation," Jpn. J. Appl. Phys. **49**(12R), 122504 (2010).
43. M. I. Bakunov and S. B. Bodrov, "Terahertz generation with tilted-front laser pulses in a contact-grating scheme," J. Opt. Soc. Am. B **31**(11), 2549 (2014).
44. Z. Ollmann, J. Hebling, and G. Almási, "Design of a contact grating setup for mJ-energy THz pulse generation by optical rectification," Appl. Phys. B **108**(4), 821–826 (2012).
45. Z. Ollmann, J. A. Fülöp, J. Hebling, and G. Almási, "Design of a high-energy terahertz pulse source based on ZnTe contact grating," Opt. Commun. **315**, 159–163 (2014).
46. P. S. Nugraha, G. Krizsán, G. Polónyi, M. I. Mechler, J. Hebling, G. Tóth, and J. A. Fülöp, "Efficient semiconductor multicycle terahertz pulse source," J. Phys. B At. Mol. Opt. Phys. **51**(9), 094007 (2018).
47. Z. Tibai, G. Krizsán, G. Tóth, G. Almási, G. Illés, L. Pálfalvi, and J. Hebling, "Scalable microstructured semiconductor THz pulse sources," Opt. Express **30**(25), 45246–45258 (2022).
48. J. A. Fülöp, G. Polónyi, B. Monoszlai, G. Andriukaitis, T. Balciunas, A. Pugzlys, G. Arthur, A. Baltuska, and J. Hebling, "Highly efficient scalable monolithic semiconductor terahertz pulse source," Optica **3**(10), 1075 (2016).
49. M. Tsubouchi, K. Nagashima, F. Yoshida, Y. Ochi, and M. Maruyama, "Contact grating device with Fabry–Perot resonator for effective terahertz light generation," Opt. Lett. **39**(18), 5439 (2014).
50. W. Cui, K. M. Awan, R. Huber, K. Dolgaleva, and J.-M. Ménard, "Broadband and High-Sensitivity Time-Resolved THz System Using Grating-Assisted Tilted-Pulse-Front Phase Matching," Adv. Opt. Mater. **10**(1), 2101136 (2022).
51. J. Hebling, G. Almási, I. Kozma, and J. Kuhl, "Velocity matching by pulse front tilting for large area THz-pulse generation," Opt. Express **10**(21), 1161 (2002).
52. M. Bashirpour, W. Cui, A. Gamouras, and J.-M. Ménard, "Scalable Fabrication of Nanogratings on GaP for Efficient Diffraction of Near-Infrared Pulses and Enhanced Terahertz Generation by Optical Rectification," Crystals **12**(5), 684 (2022).
53. M. Bashirpour, S. Khankalantary, and M. Hajizadeh, "A new hybrid metasurface design for performance improvement of thin film unbiased terahertz photoconductive source," Optik **246**, 167817 (2021).
54. F. Blanchard, L. Razzari, H. C. Bandulet, G. Sharma, R. Morandotti, J. C. Kieffer, T. Ozaki, M. Reid, H. F. Tiedje, H. K. Haugen, and F. A. Hegmann, "Generation of 1.5 μJ single-cycle terahertz pulses by optical rectification from a large aperture ZnTe crystal," Opt. Express **15**(20), 13212 (2007).
55. D. F. Nelson and E. H. Turner, "Electro-optic and Piezoelectric Coefficients and Refractive Index of Gallium Phosphide," J. Appl. Phys. **39**(7), 3337–3343 (1968).
56. W. L. Bond, "Measurement of the Refractive Indices of Several Crystals," J. Appl. Phys. **36**(5), 1674–1677 (1965).
57. D. F. Parsons and P. D. Coleman, "Far Infrared Optical Constants of Gallium Phosphide," Appl. Opt. **10**(7), 1683_1 (1971).
58. I. A. Kaplunov, A. I. Kolesnikov, G. I. Kropotov, and V. E. Rogalin, "Optical Properties of Single-Crystal Germanium in the THz Range," Opt. Spectrosc. **126**(3), 191–194 (2019).
59. J. Dai, J. Zhang, W. Zhang, and D. Grischkowsky, "Terahertz time-domain spectroscopy characterization of the far-infrared absorption and index of refraction of high-resistivity, float-zone silicon," J. Opt. Soc. Am. B **21**(7), 1379–1386 (2004).
60. D. S. Sitnikov, S. A. Romashevskiy, A. V. Ovchinnikov, O. V. Chefonov, A. B. Savel'ev, and M. B. Agranat, "Estimation of THz field strength by an electro-optic sampling technique using arbitrary long gating pulses," Laser Phys. Lett. **16**(11), 115302 (2019).

Optics EXPRESS

61. J. Neu and C. A. Schmuttenmaer, "Tutorial: An introduction to terahertz time domain spectroscopy (THz-TDS)," J. Appl. Phys. **124**(23), 231101 (2018).
62. A. Leitenstorfer, S. Hunsche, J. Shah, M. C. Nuss, and W. H. Knox, "Detectors and sources for ultrabroadband electro-optic sampling: Experiment and theory," Appl. Phys. Lett. **74**(11), 1516–1518 (1999).
63. Z. Tibai, N. M. Mbithi, G. Almási, J. A. Fülöp, and J. Hebling, "Design of Semiconductor Contact Grating Terahertz Source with Enhanced Diffraction Efficiency," Crystals **12**(8), 1173 (2022).
64. E. Castro-Camus, M. Koch, T. Kleine-Ostmann, and A. Steiger, "On the reliability of power measurements in the terahertz band," Commun. Phys. **5**(1), 42–43 (2022).
65. N. Hekmat, T. Vogel, Y. Wang, S. Mansourzadeh, F. Aslani, A. Omar, M. Hoffmann, F. Meyer, and C. J. Saraceno, "Cryogenically cooled GaP for optical rectification at high excitation average powers," Opt. Mater. Express **10**(11), 2768 (2020).
66. M. C. Hoffmann, K.-L. Yeh, J. Hebling, and K. A. Nelson, "Efficient terahertz generation by optical rectification at 1035 nm," Opt. Express **15**(18), 11706 (2007).
67. J. A. Fülöp, Z. Ollmann, C. Lombosi, C. Skrobol, S. Klingebiel, L. Pálfalvi, F. Krausz, S. Karsch, and J. Hebling, "Efficient generation of THz pulses with 0.4 mJ energy," Opt. Express **22**(17), 20155–20163 (2014).

6.2 Additional comments

6.2.1 High-field THz field strength measured with EOS

Normally, when employing the electro-optic sampling (EOS) technique to measure high-field THz pulses with ZnTe, we may encounter over-rotation, where the EOS signal is no longer linearly related to the actual THz field strength. In our case, we utilize a relatively thin 100 μm GaP crystal as the detection crystal, whose second-order nonlinear coefficient is four times lower than that of the ZnTe crystal. In our case, a 303 kV/cm THz field strength only leads to a modulation depth of 3%, which remains within the linear regime for THz field strength measurement when using the EOS technique.

6.2.2 The saturation of the THz generation in GaP

In our study, to characterize the saturation in the THz generation process, we plot the generated peak THz field vs the NIR generation beam peak fluence on the generation crystal. Previously, we noted that the generated peak THz field should be linearly proportional to the NIR generation beam peak fluence, assuming no saturation effects are involved [43]. Our data revealed that the saturation onset occurs at a peak NIR fluence of 5.1 mJ/cm^2. In many high-field THz generation studies, such a plot is often represented as THz pulse energy/THz power against NIR peak fluence/ NIR pulse energy. This is because they directly characterize the THz power using a Golay cell or THz power meter. However, in such a plot, it is challenging to pinpoint the onset of the saturation. To address this problem, besides fitting the data with power functions of different power exponents, we can plot the same figure with both axes in log scale, which transforms the power components into coefficients of linear relationships. A representative example of the log scale plot is in [89].

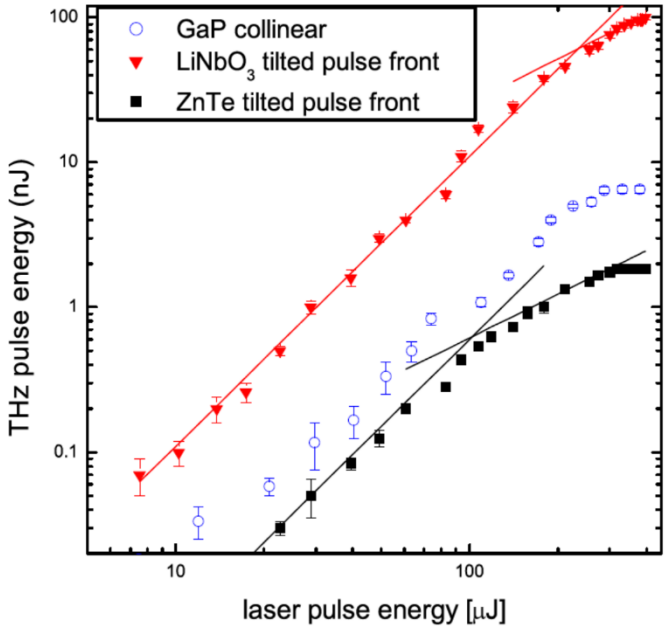

Fig. 6.1 Dependence of THz pulse energy measured with calibrated pyroelectric detector on NIR laser pulse energy for THz generation using $LiNbO_3$, GaP, and ZnTe crystals with a laser centered at 1035 nm. The solid lines represent the slopes of the data points. This figure is taken from [89].

From Fig. 6.1, we can clearly see where the slope of the linear relationship changes, representing the saturation onset of the THz generation. The NIR generation beam spot size in this figure on the GaP crystal is 5 mm in diameter, on the ZnTe wedge is 6 mm in diameter, and on the LiNbO3 wedge is 1 mm × 2 mm. Based on this data, the THz generation saturation onset when using a 1035 nm NIR generation beam for GaP occurs when the NIR fluence is approximately 2 mJ/cm^2, for ZnTe occurs when the NIR fluence is around 1.8 mJ/cm^2, and for $LiNbO_3$ occurs when the NIR fluence is close to 12.5 mJ/cm^2. The value of THz generation onset for GaP measured in Fig. 6.1 is close to the value we report in our study.

6.2.3 Future work

In the research presented in this chapter, the laser setting used is 3 W, 3 kHz. Notably, this is not the maximum pulse energy which can be generated from this Pharos amplifier. Our subsequent work involves utilizing the full pulse energy of our laser, which is 4.5 W, 3 kHz. Achieving this

necessitates adjustments to the NIR spectral broadening setup since merely increasing NIR pulse energy results in enhanced SPM inside the BK7, which leads to a stronger self-focusing effect. In the experiment using 1 mJ NIR pulse energy at laser output, a bright center spot in the beam profile is observed, causing some burning issues to the silver mirrors. A potential solution is to reposition the BK7 further from the focal point and enlarge the NIR beam size in the collimated section. Currently, the collimated NIR generation beam has a $1/e^2$ diameter of 3.3 mm, which remains smaller than the grating's dimension (1 cm× 1 cm). Our intention is to increase the $1/e^2$ diameter of the beam to approximately 1 cm, which should mitigate the saturation effects observed in the THz generation process. Consequently, we utilize higher pulse NIR pulse energy for THz generation. For instance, with a NIR generation pulse energy of 20 mJ, we would be able to generate a peak THz field strength of 1.7 MV/cm. Since the peak fluence is lower in this case, the spectral peak could shift to higher frequencies. Additionally, applying an anti-reflection coating on the surface of the generation crystal will further enhance the transmission of the NIR beam into the generation crystal. Once we attain the maximum THz field using our laser, we aim to employ this THz source to in nonlinear experiments such as driving the Bose-Einstein condensation of exciton and polariton [95]. Also, this source could be used to broaden the spectrum of the single-pulse THz detection system [96], paving the way for a wider range of applications.

Chapter 7

Summary

In this work, we introduced the background and application of different THz generation and detection techniques. In particular, we discussed the THz-TDS system which is primarily used to study the linear dispersion property in the THz range. The relevant theory for THz generation and detection through nonlinear optics methods was introduced in Chapter 2.

In Chapter 3, starting with a standard Yb:KGW fs laser system generating 200 fs pulses centered at 1035 nm, we construct a THz time-domain system. This system generates THz pulses via optical rectification and detects the THz with EOS. It can produce a THz pulse with a spectrum covering 0.5 to 4 THz with a pair of 0.3 mm-thick GaP crystals for THz generation and detection. The THz generation and detection bandwidth are limited by the laser pulse spectral bandwidth.

In the first work in Chapter 4, an HC-PCF pulse shaper broadens the NIR pulse spectrum through SPM and chirped mirror pairs are used to temporally compress NIR pulse. The resulting pulse, with its broader NIR spectrum, leads to an increased bandwidth in THz generation through difference-frequency mixing. The shorter NIR pulse, which has a higher NIR peak electric field, enhances the efficiency of THz generation. It also equips the THz detection system (EOS) with the ability to time-resolve higher frequencies. Consequently, the new system incorporating the HC-PCF pulse shaper achieves a spectrum that ranges from 0.5 to ~6 THz and the system signal intensity increases by a factor of 16.

In the second work in Chapter 5, tilted-pulse-front phase matching is achieved by etching a phase grating at the front surface of the generation and detection crystals. The tilted-pulse-front phase-matching is a perfect noncollinear phase-matching that overcomes the limitations imposed by the crystal thickness on the bandwidth for THz generation and detection due to an imperfect phase matching. Another notable feature of the grating design in this work is that, despite the

noncollinear phase matching configuration, the NIR generation beam and generated THz beam remain collinear and for the detection part, the only difference is that the EOS measures the 1st diffraction order of the NIR gating beam, rather than the collinear NIR beam. This characteristic ensures that the grating-assisted THz generation and detection can be integrated into the standard collinear THz system with minimum adjustment. As a result, with a pair of 2 mm-thick GaP with etched surface gratings for THz generation and detection, the signal intensity in this system increases by a factor of 400 compared to that of the system in Chapter 3. The spectrum of this system consistently spans from 0.5 THz to 6 THz. For a 2-minute single scan, the peak dynamic range reaches 90 dB at 3 THz.

In Chapter 6, a grating with improved uniformity is etched at the front surface of a 1 mm-thick GaP for THz generation, where the generation beam is collimated onto the generation crystal. This new THz source is the pioneering high-field THz source based on semiconductor crystals, generating high-field THz with the majority of the energy contained above 2 THz. In this setup, the THz peak field exceeds 300 kV/cm, spectrally peaking at 2.6 THz with a NIR generation pulse energy of 0.57 mJ (peak fluence of 14.2 mJ/cm^2). The damage threshold of GaP, when measured with a 1035 nm laser, stands at 5.6 J/cm^2, which is 400 times higher than the NIR peak fluence used here. Our analysis of saturation in THz generation suggests that the NIR pulse energy merely triggers the onset of saturation. With 5 mJ NIR generation pulses, we anticipate generating THz pulses approaching 1 mV/cm peak at 2.6 THz.

The work in Chapters 4 and 5 enhances the bandwidth and the sensitivity of a standard THz-TDS system. These improved systems can collect more detailed information from samples under study both in terms of spectral bandwidth and by detecting weaker signals with greater precision. The research in Chapter 6 enables the THz system to measure linear dispersion information for highly absorptive materials. It also equips the system with the capability to investigate the nonlinear properties of materials at frequencies above 2 THz. Furthermore, this THz source can be employed

to perform coherent control of Bose-Einstein condensation in the microcavities [95], 3rd harmonic THz generation beyond the traditional frequency region [97] and saturable transitions in molecular gases [98].

Chapter 8

Conclusion

This thesis enhanced the performance of a THz-TDS system, leveraging a standard Yb:KGW femtosecond laser amplifier in terms of bandwidth, sensitivity, and field strength.

An expanded system bandwidth allows the THz-TDS system to acquire information from more intricate materials, characterize a broader range of materials, and uncover phenomena potentially obscured by a limited bandwidth. Additionally, a system with a wider bandwidth inherently possesses higher temporal resolution, facilitating the study of ultrafast material processes. More generally, broadband THz systems have potential applications in high-data-rate communications and high-resolution imaging.

The THz system with augmented sensitivity can discern nuanced material features, fostering a deeper comprehension of material properties. Such sensitivity is advantageous for chemical analysis and quality control, especially with low-concentration samples. Enhanced sensitivity also has implications for environmental monitoring, complex biological system studies and long-distance communications.

Chapters 5 and 6 detail the enhancement of the generation efficiency using a GaP crystal with a surface-etched phase grating, enabling the THz-TDS to produce both high-average-power and high-field-strength THz pulses. High-power THz pulses can probe highly absorptive materials, increase THz penetration depth of the THz and generally study the material under high illuminance. Such pulses also hold promise for remote sensing and long-distance data communications. The high-field THz source introduced in Chapter 6, is the first high-field THz source centered above 2 THz based on high damage threshold semiconductor nonlinear crystals. This new source has

potential applications in high-field THz magnetic pulse generation at higher frequencies, nonlinear spectroscopy at higher frequencies, and coherent control of quantum states, phase transitions, chemical reactions, and lattice vibrations.

The THz-TDS system developed in this thesis was initially intended to study the photo-illuminance effects in PMMA [99] and to coherently control the exciton-polariton Bose-Eistein condensation in semiconductor micro-cavities [95]. Regrettably, while the tools are prepared, time constraints limit further pursuit of these projects. I hope to continue this work during the time that I am still in the group and encourage new students or postdocs to advance these endeavors.

Techniques for generating and detecting frequencies below 5 THz and above 15 THz have matured over the recent decades. The current challenge lies in the 5 THz and 10 THz range [100]. While metallic spintronics and air plasma can span this range, the spectral density at certain frequencies remains suboptimal. Organic crystals, pumped by femtosecond laser with a wavelength exceeding 1200 nm, are beginning to bridge this gap. Continued development of metallic spintronics, air plasma, and organic crystals may yield efficient THz generation and detection in this range. In my view, further development of nonlinear crystals for THz generation and detection remains crucial, especially in addressing a certain narrow frequency band. Silicon Carbide (SiC) is a potential crystal for the 5 to 15 THz range [101,102]. The surface grating can further optimize the phase-matching for THz generation and detection at certain frequencies on potential crystals like SiC. There is potential to refine surface grating fabrication, aiming for efficient titled pulse front generation with a collinear configuration. If a blazed grating is crafted on the front surface of the generation crystals, diffraction efficiency could significantly increase, optimizing THz generation from a singular diffraction order other than from both $\pm 1^{st}$ diffraction orders. Collaborating with scientists specializing in the design and growth of nonlinear crystals could lead

to the development of novel crystals optimized for THz generation and detection in the new THz gap.

References

[1] S. Almoughrabie, C. Ngari, L. Guillier, R. Briandet, V. Poulet, and F. Dubois-Brissonnet, *Rapid Assessment and Prediction of the Efficiency of Two Preservatives against S. Aureus in Cosmetic Products Using High Content Screening—Confocal Laser Scanning Microscopy*, PLOS ONE **15**, e0236059 (2020).

[2] R. I. Stantchev, X. Yu, T. Blu, and E. Pickwell-MacPherson, *Real-Time Terahertz Imaging with a Single-Pixel Detector*, Nat. Commun. **11**, 2535 (2020).

[3] K. Ahi and M. Anwar, *Advanced Terahertz Techniques for Quality Control and Counterfeit Detection*, in *Terahertz Physics, Devices, and Systems X: Advanced Applications in Industry and Defense*, Vol. 9856 (SPIE, 2016), pp. 31–44.

[4] G. Tzydynzhapov, P. Gusikhin, V. Muravev, A. Dremin, Y. Nefyodov, and I. Kukushkin, *New Real-Time Sub-Terahertz Security Body Scanner*, J. Infrared Millim. Terahertz Waves **41**, 632 (2020).

[5] M. Naftaly and R. E. Miles, *Terahertz Time-Domain Spectroscopy for Material Characterization*, 8 (n.d.).

[6] S. Scarfe, W. Cui, A. Luican-Mayer, and J.-M. Ménard, *Systematic THz Study of the Substrate Effect in Limiting the Mobility of Graphene*, Sci. Rep. **11**, 8729 (2021).

[7] F. Rutz, M. Koch, S. Khare, M. Moneke, H. Richter, and U. Ewert, *TERAHERTZ QUALITY CONTROL OF POLYMERIC PRODUCTS*, Int. J. Infrared Millim. Waves **27**, 547 (2006).

[8] F. Ellrich, M. Bauer, N. Schreiner, A. Keil, T. Pfeiffer, J. Klier, S. Weber, J. Jonuscheit, F. Friederich, and D. Molter, *Terahertz Quality Inspection for Automotive and Aviation Industries*, J. Infrared Millim. Terahertz Waves **41**, 470 (2020).

[9] S. Koenig et al., *Wireless Sub-THz Communication System with High Data Rate*, Nat. Photonics **7**, 12 (2013).

[10] T. Kürner, D. M. Mittleman, and T. Nagatsuma, editors , *THz Communications: Paving the Way Towards Wireless Tbps*, Vol. 234 (Springer International Publishing, Cham, 2022).

[11] R. Köhler, A. Tredicucci, F. Beltram, H. E. Beere, E. H. Linfield, A. G. Davies, D. A. Ritchie, R. C. Iotti, and F. Rossi, *Terahertz Semiconductor-Heterostructure Laser*, Nature **417**, 6885 (2002).

[12] B. S. Williams, S. Kumar, Q. Hu, and J. L. Reno, *Operation of Terahertz Quantum-Cascade Lasers at 164 K in Pulsed Mode and at 117 K in Continuous-Wave Mode*, Opt. Express **13**, 3331 (2005).

[13] G. P. Williams, *FAR-IR/THz Radiation from the Jefferson Laboratory, Energy Recovered Linac, Free Electron Laser*, Rev. Sci. Instrum. **73**, 1461 (2002).

[14] M. Yu. Glyavin, A. G. Luchinin, G. S. Nusinovich, J. Rodgers, D. G. Kashyn, C. A. Romero-Talamas, and R. Pu, *A 670 GHz Gyrotron with Record Power and Efficiency*, Appl. Phys. Lett. **101**, 153503 (2012).

[15] G. Mourou, C. V. Stancampiano, A. Antonetti, and A. Orszag, *Picosecond Microwave Pulses Generated with a Subpicosecond Laser-driven Semiconductor Switch*, Appl. Phys. Lett. **39**, 295 (1981).

[16] J. T. Darrow, X. -C. Zhang, and D. H. Auston, *Power Scaling of Large-aperture Photoconducting Antennas*, Appl. Phys. Lett. **58**, 25 (1991).

[17] Q. Chen, M. Tani, Z. Jiang, and X.-C. Zhang, *Electro-Optic Transceivers for Terahertz-Wave Applications*, J. Opt. Soc. Am. B **18**, 823 (2001).

[18] J. Dai, J. Liu, and X.-C. Zhang, *Terahertz Wave Air Photonics: Terahertz Wave Generation and Detection with Laser-Induced Gas Plasma*, IEEE J. Sel. Top. Quantum Electron. **17**, 183 (2011).

[19] T. Seifert et al., *Efficient Metallic Spintronic Emitters of Ultrabroadband Terahertz Radiation*, Nat. Photonics **10**, 483 (2016).

[20] T. Vogel et al., *Average Power Scaling of THz Spintronic Emitters Efficiently Cooled in Reflection Geometry*, Opt. Express **30**, 20451 (2022).

[21] M. Tonouchi, *Cutting-Edge Terahertz Technology*, Nat. Photonics **1**, 97 (2007).

[22] K. Delfanazari, R. A. Klemm, H. J. Joyce, D. A. Ritchie, and K. Kadowaki, *Integrated, Portable, Tunable, and Coherent Terahertz Sources and Sensitive Detectors Based on Layered Superconductors*, Proc. IEEE **108**, 721 (2020).

[23] W. Cui, E. K. Yalavarthi, A. V. Radhan, M. Bashirpour, A. Gamouras, and J.-M. Ménard, *High-Field THz Source Centered at 2.6 THz*, Opt. Express **31**, 32468 (2023).

[24] R. C. Jones, *On the Relation between the Speed of Response and the Detectivity of Lead Sulfide Photoconductive Cells*, JOSA **43**, 1008 (1953).

[25] J. C. Mather, *Bolometers: Ultimate Sensitivity, Optimization, and Amplifier Coupling*, Appl. Opt. **23**, 584 (1984).

[26] F. Simoens, *THz Bolometer Detectors*, in *Physics and Applications of Terahertz Radiation*, edited by M. Perenzoni and D. J. Paul (Springer Netherlands, Dordrecht, 2014), pp. 35–75.

[27] M. J. E. Golay, *A Pneumatic Infra-Red Detector*, Rev. Sci. Instrum. **18**, 357 (1947).

[28] M. J. E. Golay, *Theoretical Consideration in Heat and Infra-Red Detection, with Particular Reference to the Pneumatic Detector*, Rev. Sci. Instrum. **18**, 347 (1947).

[29] W. Woltersdorff, *Über die optischen Konstanten dünner Metallschichten im langwelligen Ultrarot*, Z. Für Phys. **91**, 230 (1934).

[30] S. A. Kuznetsov, A. G. Paulish, M. Navarro-Cía, and A. V. Arzhannikov, *Selective Pyroelectric Detection of Millimetre Waves Using Ultra-Thin Metasurface Absorbers*, Sci. Rep. **6**, 1 (2016).

[31] W. C. B. Peatman, T. W. Crowe, and M. Shur, *A Novel Schottky/2-DEG Diode for Millimeter- and Submillimeter-Wave Multiplier Applications*, IEEE Electron Device Lett. **13**, 11 (1992).

[32] L. Liu, J. L. Hesler, H. Xu, A. W. Lichtenberger, and R. M. Weikle, *A Broadband Quasi-Optical Terahertz Detector Utilizing a Zero Bias Schottky Diode*, IEEE Microw. Wirel. Compon. Lett. **20**, 504 (2010).

[33] N. M. Burford and M. O. El-Shenawee, *Review of Terahertz Photoconductive Antenna Technology*, Opt. Eng. **56**, 010901 (2017).

[34] P. U. Jepsen, R. H. Jacobsen, and S. R. Keiding, *Generation and Detection of Terahertz Pulses from Biased Semiconductor Antennas*, JOSA B **13**, 2424 (1996).

[35] M. van Exter and D. R. Grischkowsky, *Characterization of an Optoelectronic Terahertz Beam System*, IEEE Trans. Microw. Theory Tech. **38**, 1684 (1990).

[36] P. Uhd Jepsen, M. Schall, V. Schyja, C. Winnewisser, H. Helm, and S. R. Keiding, *Detection of High Power THz Pulses by Phase Retardation in an Electro-Optic Crystal*, in *Ultrafast Processes in Spectroscopy*, edited by O. Svelto, S. De Silvestri, and G. Denardo (Springer US, Boston, MA, 1996), pp. 645–648.

[37] Q. Wu, T. D. Hewitt, and X. -C. Zhang, *Two-dimensional Electro-optic Imaging of THz Beams*, Appl. Phys. Lett. **69**, 1026 (1996).

[38] A. Nahata, D. H. Auston, T. F. Heinz, and C. Wu, *Coherent Detection of Freely Propagating Terahertz Radiation by Electro-optic Sampling*, Appl. Phys. Lett. **68**, 150 (1996).

[39] X. Lu and X.-C. Zhang, *Investigation of Ultra-Broadband Terahertz Time-Domain Spectroscopy with Terahertz Wave Gas Photonics*, Front. Optoelectron. **7**, 121 (2014).

[40] X. Lu and X.-C. Zhang, *Balanced Terahertz Wave Air-Biased-Coherent-Detection*, Appl. Phys. Lett. **98**, 151111 (2011).

[41] X.-C. Zhang and J. Xu, *Introduction to THz Wave Photonics* (Springer US, Boston, MA, 2010).

[42] A. Schiff-Kearn, *Experimental and Numerical Investigations into Terahertz Time-Domain Spectroscopy*, 98 (n.d.).

[43] R. W. Boyd, *Nonlinear Optics*, 4th ed. (Academic Press is an imprint of Elsevier, San Diego, 2019).

[44] J. Hebling, G. Almási, I. Kozma, and J. Kuhl, *Velocity Matching by Pulse Front Tilting for Large Area THz-Pulse Generation*, Opt. Express **10**, 1161 (2002).

[45] J. Hebling, A. G. Stepanov, G. Almási, B. Bartal, and J. Kuhl, *Tunable THz Pulse Generation by Optical Rectification of Ultrashort Laser Pulses with Tilted Pulse Fronts*, Appl. Phys. B Lasers Opt. **78**, 593 (2004).

[46] J. Hebling, K.-L. Yeh, M. C. Hoffmann, B. Bartal, and K. A. Nelson, *Generation of High-Power Terahertz Pulses by Tilted-Pulse-Front Excitation and Their Application Possibilities*, J. Opt. Soc. Am. B **25**, B6 (2008).

[47] D. H. Auston, *Subpicosecond Electro-optic Shock Waves*, Appl. Phys. Lett. **43**, 713 (1983).

[48] D. H. Auston, K. P. Cheung, J. A. Valdmanis, and D. A. Kleinman, *Cherenkov Radiation from Femtosecond Optical Pulses in Electro-Optic Media*, Phys. Rev. Lett. **53**, 1555 (1984).

[49] D. Kleinman and D. Auston, *Theory of Electrooptic Shock Radiation in Nonlinear Optical Media*, IEEE J. Quantum Electron. **20**, 964 (1984).

[50] M. C. Hoffmann and J. A. Fülöp, *Intense Ultrashort Terahertz Pulses: Generation and Applications*, J. Phys. Appl. Phys. **44**, 083001 (2011).

[51] L. Gingras, W. Cui, A. W. Schiff-Kearn, J.-M. Ménard, and D. G. Cooke, *Active Phase Control of Terahertz Pulses Using a Dynamic Waveguide*, Opt. Express **26**, 13876 (2018).

[52] N. Couture, W. Cui, M. Lippl, R. Ostic, D. J. J. Fandio, E. K. Yalavarthi, A. Vishnuradhan, A. Gamouras, N. Y. Joly, and J.-M. Ménard, *Single-Pulse Terahertz Spectroscopy Monitoring Sub-Millisecond Time Dynamics at a Rate of 50 kHz*, Nat. Commun. **14**, 1 (2023).

[53] L. Gingras, *All-Optical THz Pulse Shaping in a Dynamic Waveguide*, 131 (n.d.).

[54] J. A. Fülöp, Gy. Polónyi, B. Monoszlai, G. Andriukaitis, T. Balciunas, A. Pugzlys, G. Arthur, A. Baltuska, and J. Hebling, *Highly Efficient Scalable Monolithic Semiconductor Terahertz Pulse Source*, Optica **3**, 1075 (2016).

[55] L. Pálfalvi, J. A. Fülöp, G. Almási, and J. Hebling, *Novel Setups for Extremely High Power Single-Cycle Terahertz Pulse Generation by Optical Rectification*, Appl. Phys. Lett. **92**, 171107 (2008).

[56] M. I. Bakunov and S. B. Bodrov, *Terahertz Generation with Tilted-Front Laser Pulses in a Contact-Grating Scheme*, J. Opt. Soc. Am. B **31**, 2549 (2014).

[57] K. Nagashima, M. Tsubouchi, Y. Ochi, and M. Maruyama, *Improvement of Contact Grating Device for Efficient Terahertz Wave Generation Using Bi-Angular Filter*, J. Appl. Phys. **123**, 123104 (2018).

[58] Z. Ollmann, J. Hebling, and G. Almási, *Design of a Contact Grating Setup for mJ-Energy THz Pulse Generation by Optical Rectification*, Appl. Phys. B **108**, 821 (2012).

[59] G. Gallot and D. Grischkowsky, *Electro-Optic Detection of Terahertz Radiation*, J. Opt. Soc. Am. B **16**, 1204 (1999).

[60] W. Withayachumnankul and M. Naftaly, *Fundamentals of Measurement in Terahertz Time-Domain Spectroscopy*, J. Infrared Millim. Terahertz Waves **35**, 610 (2014).

[61] M. Naftaly and R. E. Miles, *Terahertz Time-Domain Spectroscopy of Silicate Glasses and the Relationship to Material Properties*, J. Appl. Phys. **102**, 043517 (2007).

[62] N. Hekmat, T. Vogel, Y. Wang, S. Mansourzadeh, F. Aslani, A. Omar, M. Hoffmann, F. Meyer, and C. J. Saraceno, *Cryogenically Cooled GaP for Optical Rectification at High Excitation Average Powers*, Opt. Mater. Express **10**, 2768 (2020).

[63] J. A. Fülöp, Z. Ollmann, C. Lombosi, C. Skrobol, S. Klingebiel, L. Pálfalvi, F. Krausz, S. Karsch, and J. Hebling, *Efficient Generation of THz Pulses with 0.4 mJ Energy*, Opt. Express **22**, 20155 (2014).

[64] F. Blanchard et al., *Generation of 1.5 μJ Single-Cycle Terahertz Pulses by Optical Rectification from a Large Aperture ZnTe Crystal*, Opt. Express **15**, 13212 (2007).

[65] D. F. Nelson and E. H. Turner, *Electro-optic and Piezoelectric Coefficients and Refractive Index of Gallium Phosphide*, J. Appl. Phys. **39**, 3337 (2003).

[66] W. L. Bond, *Measurement of the Refractive Indices of Several Crystals*, J. Appl. Phys. **36**, 1674 (1965).

[67] J. Dai, J. Zhang, W. Zhang, and D. Grischkowsky, *Terahertz Time-Domain Spectroscopy Characterization of the Far-Infrared Absorption and Index of Refraction of High-Resistivity, Float-Zone Silicon*, JOSA B **21**, 1379 (2004).

[68] D. S. Sitnikov, S. A. Romashevskiy, A. V. Ovchinnikov, O. V. Chefonov, A. B. Savel'ev, and M. B. Agranat, *Estimation of THz Field Strength by an Electro-Optic Sampling Technique Using Arbitrary Long Gating Pulses*, Laser Phys. Lett. **16**, 115302 (2019).

[69] D. F. Parsons and P. D. Coleman, *Far Infrared Optical Constants of Gallium Phosphide*, Appl. Opt. **10**, 1683_1 (1971).

[70] W. Cui, A. W. Schiff-Kearn, E. Zhang, N. Couture, F. Tani, D. Novoa, P. St. J. Russell, and J.-M. Ménard, *Broadband and Tunable Time-Resolved THz System Using Argon-Filled Hollow-Core Photonic Crystal Fiber*, APL Photonics **3**, 111301 (2018).

[71] P. S. J. Russell, P. Hölzer, W. Chang, A. Abdolvand, and J. C. Travers, *Hollow-Core Photonic Crystal Fibres for Gas-Based Nonlinear Optics*, Nat. Photonics **8**, 4 (2014).

[72] R. Piccoli, A. Rovere, Y.-G. Jeong, Y. Jia, L. Zanotto, F. Légaré, B. E. Schmidt, R. Morandotti, and L. Razzari, *Extremely Broadband Terahertz Generation via Pulse Compression of an Ytterbium Laser Amplifier*, Opt. Express **27**, 32659 (2019).

[73] E. Matsubara, M. Nagai, and M. Ashida, *Ultrabroadband Coherent Electric Field from Far Infrared to 200 THz Using Air Plasma Induced by 10 Fs Pulses*, Appl. Phys. Lett. **101**, 011105 (2012).

[74] P. St. J. Russell, *Photonic-Crystal Fibers*, J. Light. Technol. **24**, 4729 (2006).

[75] F. Benabid and P. J. Roberts, *Linear and Nonlinear Optical Properties of Hollow Core Photonic Crystal Fiber*, J. Mod. Opt. **58**, 87 (2011).

[76] A. Halpin, N. Couture, and J.-M. Ménard, *Optical Pulse Structuring in Gas-Filled Hollow-Core Kagomé PCF for Generation and Detection of Phase-Locked Multi-THz Pulses [Invited]*, Opt. Mater. Express **9**, 3115 (2019).

[77] A. Leitenstorfer, S. Hunsche, J. Shah, M. C. Nuss, and W. H. Knox, *Detectors and Sources for Ultrabroadband Electro-Optic Sampling: Experiment and Theory*, Appl. Phys. Lett. **74**, 1516 (1999).

[78] F. Blanchard, B. E. Schmidt, X. Ropagnol, N. Thiré, T. Ozaki, R. Morandotti, D. G. Cooke, and F. Légaré, *Terahertz Pulse Generation from Bulk GaAs by a Tilted-Pulse-Front Excitation at 1.8* μ *m*, Appl. Phys. Lett. **105**, 241106 (2014).

[79] W. Cui, K. M. Awan, R. Huber, K. Dolgaleva, and J.-M. Ménard, *Broadband and High-Sensitivity Time-Resolved THz System Using Grating-Assisted Tilted-Pulse-Front Phase Matching*, Adv. Opt. Mater. **10**, 2101136 (2022).

[80] G. Krizsán, Z. Tibai, G. Tóth, P. S. Nugraha, G. Almási, J. Hebling, and J. A. Fülöp, *Uniformly Scalable Lithium Niobate THz Pulse Source in Transmission Geometry*, Opt. Express **30**, 4434 (2022).

[81] Z. Tibai, G. Krizsán, G. Tóth, G. Almási, G. Illés, L. Pálfalvi, and J. Hebling, *Scalable Microstructured Semiconductor THz Pulse Sources*, Opt. Express **30**, 45246 (2022).

[82] P. S. Nugraha, G. Krizsán, G. Polónyi, M. I. Mechler, J. Hebling, G. Tóth, and J. A. Fülöp, *Efficient Semiconductor Multicycle Terahertz Pulse Source*, J. Phys. B At. Mol. Opt. Phys. **51**, 094007 (2018).

[83] A. Halpin, W. Cui, A. W. Schiff-Kearn, K. M. Awan, K. Dolgaleva, and J.-M. Ménard, *Enhanced Terahertz Detection Efficiency via Grating-Assisted Noncollinear Electro-Optic Sampling*, Phys. Rev. Appl. **12**, 031003 (2019).

[84] J.-M. Ménard, A. Halpin, and W. Cui, *Broadband THz Receiver Using Thick Patterned Semiconductor Crystals*, US11422088B2 (23 August 2022).

[85] M. Naftaly, *Metrology Issues and Solutions in THz Time-Domain Spectroscopy: Noise, Errors, Calibration*, IEEE Sens. J. **13**, 8 (2013).

[86] J. Neu and C. A. Schmuttenmaer, *Tutorial: An Introduction to Terahertz Time Domain Spectroscopy (THz-TDS)*, J. Appl. Phys. **124**, 231101 (2018).

[87] U. Puc, T. Bach, P. Günter, M. Zgonik, and M. Jazbinsek, *Ultra-Broadband and High-Dynamic-Range THz Time-Domain Spectroscopy System Based on Organic Crystal Emitter and Detector in Transmission and Reflection Geometry*, Adv. Photonics Res. **2**, 2000098 (2021).

[88] T. Löffler, T. Hahn, M. Thomson, F. Jacob, and H. G. Roskos, *Large-Area Electro-Optic ZnTe Terahertz Emitters*, Opt. Express **13**, 5353 (2005).

[89] M. C. Hoffmann, K.-L. Yeh, J. Hebling, and K. A. Nelson, *Efficient Terahertz Generation by Optical Rectification at 1035 Nm*, Opt. Express **15**, 11706 (2007).

[90] N. Nilforoushan, T. Apretna, C. Song, T. Boulier, J. Tignon, S. Dhillon, M. Hanna, and J. Mangeney, *Ultra-Broadband THz Pulses with Electric Field Amplitude Exceeding 100 kV/Cm at a 200 kHz Repetition Rate*, Opt. Express **30**, 15556 (2022).

[91] B. Monoszlai, C. Vicario, M. Jazbinsek, and C. P. Hauri, *High-Energy Terahertz Pulses from Organic Crystals: DAST and DSTMS Pumped at Ti:Sapphire Wavelength*, Opt. Lett. **38**, 5106 (2013).

[92] A. Rovere, Y.-G. Jeong, R. Piccoli, S.-H. Lee, S.-C. Lee, O.-P. Kwon, M. Jazbinsek, R. Morandotti, and L. Razzari, *Generation of High-Field Terahertz Pulses in an HMQ-TMS Organic Crystal Pumped by an Ytterbium Laser at 1030 Nm*, Opt. Express **26**, 2509 (2018).

[93] C. Vicario, A. V. Ovchinnikov, S. I. Ashitkov, M. B. Agranat, V. E. Fortov, and C. P. Hauri, *Generation of 0.9-mJ THz Pulses in DSTMS Pumped by a Cr:Mg_2SiO_4 Laser*, Opt. Lett. **39**, 6632 (2014).

[94] M. Bashirpour, W. Cui, A. Gamouras, and J.-M. Ménard, *Scalable Fabrication of Nanogratings on GaP for Efficient Diffraction of Near-Infrared Pulses and Enhanced Terahertz Generation by Optical Rectification*, Crystals **12**, 684 (2022).

[95] J.-M. Ménard, C. Poellmann, M. Porer, U. Leierseder, E. Galopin, A. Lemaître, A. Amo, J. Bloch, and R. Huber, *Revealing the Dark Side of a Bright Exciton–Polariton Condensate*, Nat. Commun. **5**, 4648 (2014).

[96] N. Couture, W. Cui, M. Lippl, R. Ostic, D. J. J. Fandio, E. K. Yalavarthi, A. V. Radhan, A. Gamouras, N. Joly, and J.-M. Ménard, *Single-Pulse Time-Resolved Terahertz Spectroscopy of Sub-Millisecond Time Dynamics*, arXiv:2207.11766.

[97] H. A. Hafez et al., *Extremely Efficient Terahertz High-Harmonic Generation in Graphene by Hot Dirac Fermions*, Nature **561**, 7724 (2018).

[98] P. Rasekh, A. Safari, M. Yildirim, R. Bhardwaj, J.-M. Ménard, K. Dolgaleva, and R. W. Boyd, *Terahertz Nonlinear Spectroscopy of Water Vapor*, ACS Photonics **8**, 1683 (2021).

[99] D. L. N. Kallepalli, A. M. Alshehri, D. T. Marquez, L. Andrzejewski, J. C. Scaiano, and R. Bhardwaj, *Ultra-High Density Optical Data Storage in Common Transparent Plastics*, Sci. Rep. **6**, 26163 (2016).

[100] A. Leitenstorfer et al., *The 2023 Terahertz Science and Technology Roadmap*, J. Phys. Appl. Phys. **56**, 223001 (2023).

[101] M. Naftaly, J. F. Molloy, B. Magnusson, Y. M. Andreev, and G. V. Lanskii, *Silicon Carbide—a High-Transparency Nonlinear Material for THz Applications*, Opt. Express **24**, 2590 (2016).

[102] M. P. Fischer, J. Bühler, G. Fitzky, T. Kurihara, S. Eggert, A. Leitenstorfer, and D. Brida, *Coherent Field Transients below 15 THz from Phase-Matched Difference Frequency Generation in 4H-SiC*, Opt. Lett. **42**, 2687 (2017).